Engineering Nuclear Pore Complex Function on Biological Interfaces

Inauguraldissertation

zur

Erlangung der Würde eines Doktors der Philosophie

vorgelegt der

Philosophisch-Naturwissenschaftlichen Fakultät

der Universität Basel

von

Ludovit Pavel Zweifel

aus Glarus Süd (GL)

Basel, 2019

Genehmigt von der Philosophisch-Naturwissenschaftlichen Fakultät

auf Antrag von

Prof. Dr. Roderick Lim

Prof. Dr. Ulrich Keyser

Basel, den 19. September 2017

Prof. Dr. Martin Spiess

Dekan

Acknowledgement

I appreciate Prof. Lim and the entire lab for the joyful time and the motivating atmosphere; Prof. Keyser for his hospitality and advice; Chaim, Kai, Rafael, Larisa, Tina and Tim for scrutinizing parts of this thesis and their priceless input; all my office mates during the last years: Elena, Suncica, Aska, Yusuke, Philippe, Bref, Janne, Kai, Marija, Marko and Tobias.

Special thanks go to Tina, my mom, my sister and the entire family for their everlasting support and all their love; to all my friends that I can always count on; and to my daughter for teaching me what truly counts.

Abstract

Nuclear pore complexes (NPCs) are the sole gateways that regulate the bidirectional exchange of macromolecules across the nuclear envelope (NE). In spite of bearing a ~40 nm wide aqueous channel, each NPC controls this fundamental nucleocytoplasmic transport (NCT) with unprecedented selectivity and efficiency. It is well established that soluble nuclear transport receptors (NTRs) such as Karyopherinβ1 (Kapβ1), regulate the traffic of specific cargoes by their multivalent interactions with intrinsically disordered, phenylalanine-glycine-rich protein (FG Nucleoporins or FG Nups) domains within the NPC. Nevertheless, how the FG Nups reject non-specific macromolecules while promoting the traffic of cargo-carrying NTRs remains elusive.

Recent *in vitro* studies on intrinsically disordered, end-grafted FG Nup domain brushes suggest that Kapβ1 is a *bona fide* constituent of the FG Nup permeability barrier and plays an integral role in regulating NPC transport selectivity and speed. However, these studies were performed directly on planar Au or SiO_2 surfaces and are lacking a nanoconfined pore geometry as one of the key characteristics of the NPC.

This thesis provides a route to engineer biomimetic NPCs for the *ex vivo* investigation of the FG Nup permeability barrier at biological interfaces under spatial confinement. NTA – Histidine affinity mediated immobilization of FG Nup domain brushes on supported lipid layers formed by spontaneous liposome spreading proved to be a versatile tool to impart NPC functionality on Au and SiO_2 substrates. A hallmark of minimal NPC models engineered by this approach is that the FG Nups are exposed to a consistent biointerface regardless of the underlying support. This allows one to investigate pristine FG Nup brushes and brushes interacting with Kapβ1 formed on lipid layers in a holistic manner by different techniques.

Contents

List of Figures

List of Tables

Glossary

ACF	Autocorrelation Function
BSA	Bovine Serum Albumin
CAS	Cellular Apoptosis Susceptibility
CCF	Cross-Correlation Function
CPR	Cytoplasmic Ring
CW	Continuous Wave
DGS NTA(Ni)	1,2-dioleoyl-sn-glycero-3-[(N-(5-amino-1-carboxypentyl)iminodiacetic acid)succinyl]
DLS	Dynamic Light Scattering
DNA	Deoxyribonucleic Acid
DOPC	1,2-dioleoyl-*sn*-glycero-3-phosphocholine
EM	Electron Microscopy
EMCCD	Electron Multiplying Charge-Coupled Device
ER	Endoplasmic Reticulum
FCCS	Fluorescence Cross-Correlation Spectroscopy
FCS	Fluorescence Correlation Spectroscopy
FG	Phenylalanine-Glycine
FIB	Focused Ion Beam
FLCCS	Fluorescence Lifetime Cross-Correlation Spectroscopy
FLCS	Fluorescence Lifetime Correlation Spectroscopy
FOV	Field of View
FRAP	Fluorescent Recovery after Photobleaching
GDP	Guanosine Diphosphate
GLFG	Glycine-Leucine-Phenylalanine-Glycine
GNC	Glass Nanocapillary
GTP	Guanosine Triphosphate
He	Helium
HEAT	Helical Structure in Huntingtin, Elongation Factor 3, Protein Phosphatase 2A, and Yeast Kinase TOR1
HeSTIM	Helium Scanning Transmission Ion Microscopy
His_6	6x Histidine tag
ICR	Ion Current Rectification
I-V	Current-to-Voltage Ratio
IBB	Importinβ Binding Domain
IDP	Intrinsically Disordered Protein
INM	Inner Nuclear Membrane
iPSF	inclined Point Spread Function
IRF	Instrument Response Function
Kap	Karyopherin
LSCM	Laser Scanning Confocal Microscopy
MSD	Mean Square Displacement
NCT	Nucleocytoplasmic Transport

NE	Nuclear Envelope
NES	Nuclear Export Sequence
NLS	Nuclear Localization Sequence
NPC	Nuclear Pore Complex
NPR	Nucleoplasmic Ring
Nsp1FF12	Yeast Nucleoporin with 12 FG Binding Domains
Nsp1SS12	Nsp1FF12 Mutant with all Phenylalanine Sites Substituted to Serine
NTA(Ni)	Nitrilotriacetic acid Nickel Chelator
NTF2	Nuclear Transport Factor 2
NTR	Nuclear Transport Receptor
Nup	Nucleoporin
ONM	Outer Nuclear Membrane
PBS	Phosphate Buffered Saline
PDI	Polydispersity Index
PDMS	Polydimethylsiloxan
PET	Polyethylene Terephthalate
pH	Potential of Hydrogen
PIE	Pulse Interleaved Excitation
RanGAP	RanGTPase Activating Protein
RanGDP	Guanosine Diphosphate On-Bound Ran Protein
RanGEF	Ran Guanine Nucleotide Exchange Factor
RanGTP	Guanosine Triphosphate On-Bound Ran Protein
Rh	Rhodamine
Rh PE	L-α-Phosphatidylethanolamine-N-(lissamine rhodamine B sulfonyl) (Ammonium Salt)
RNA	Ribonucleic Acid
ROD	Reduction of Dimension
ROI	Region of Interest
SD	Standard Deviation
SE	Secondary Electron
SEM	Scanning Electron Microscopy
SLB	Supported Lipid Bilayer
SLM	Supported Lipid Monolayer
SMF	Single Molecule Fluorescence
SNR	Signal to Noise Ratio
SPAD	Single Photon Avalanche Detector
SPEED	Single-Point Edge-Excitation Sub-Diffraction Microscopy
SR	Spoke Ring
STEM	Scanning Transmission Electron Microscopy
SUV	Small Unilamellar Vesicle
TCSPC	Time-Correlated Single Photon Counting
TEM	Transmission Electron Microscopy
TIRF	Total Internal Reflection Fluorescence Microscopy

Chapter 1

Introduction

1 Introduction

1.1 The Nuclear Pore Complex

Eukaryotic cells are organized into distinct compartments by intracellular membranes. Each compartment exhibits a characteristic structure, biochemical composition and function. Most pronounced amongst these membrane-enclosed organelles is the nucleus, which is encircled by two lipid bilayers. This so called nuclear envelope (NE) separates the genetic material and nucleoli containing nucleoplasm from the cytoplasm. It therefore not only protects the genome from exogenous causes of genomic instability, but also segregates the sites of transcription and translation. The formidable challenge of mediating a bidirectional exchange of essential molecules and complexes across the NE is accomplished by nuclear pore complexes (NPCs; Figure 1.1)[1,2].

NPCs are conserved from yeast to human. They are arguably the largest protein machineries in vertebrates (~110 – 125 MDa measured for *Xenopus laevis*[3] which will serve as model organism throughout this chapter) and perforate the NE in large numbers (average number in *Xenopus laevis* ~3500 NPCs per nucleus)[4]. As sole gateways between the nucleoplasm and the cytoplasm, NPCs exhibit exceptional features and a remarkable structure (see Section 1.1.1).

The speed and selectivity of the nucleocytoplasmic transport (NCT) is remarkable. This is regulated by soluble nuclear transport receptors (NTRs) that traffic of essential cargoes[5] through the NPCs. Their multivalent interactions with intrinsically disordered protein (IDP) domains within the NPC were identified as the key step to bridge the selectivity barrier (see Sections 1.1.2 through 1.2.2).

Still, the underlying mechanistic details of the NPC gating are incompletely understood and remain disputed. The major challenge to address the biophysical nature conclusively lies in resolving the native ensemble conformation of the IDP domains and the spatiotemporal scales of the transport process *in vivo*. Inevitably, models of NPC barrier functionality have evolved from *in vitro* studies (see Section 1.2.3)[6–11].

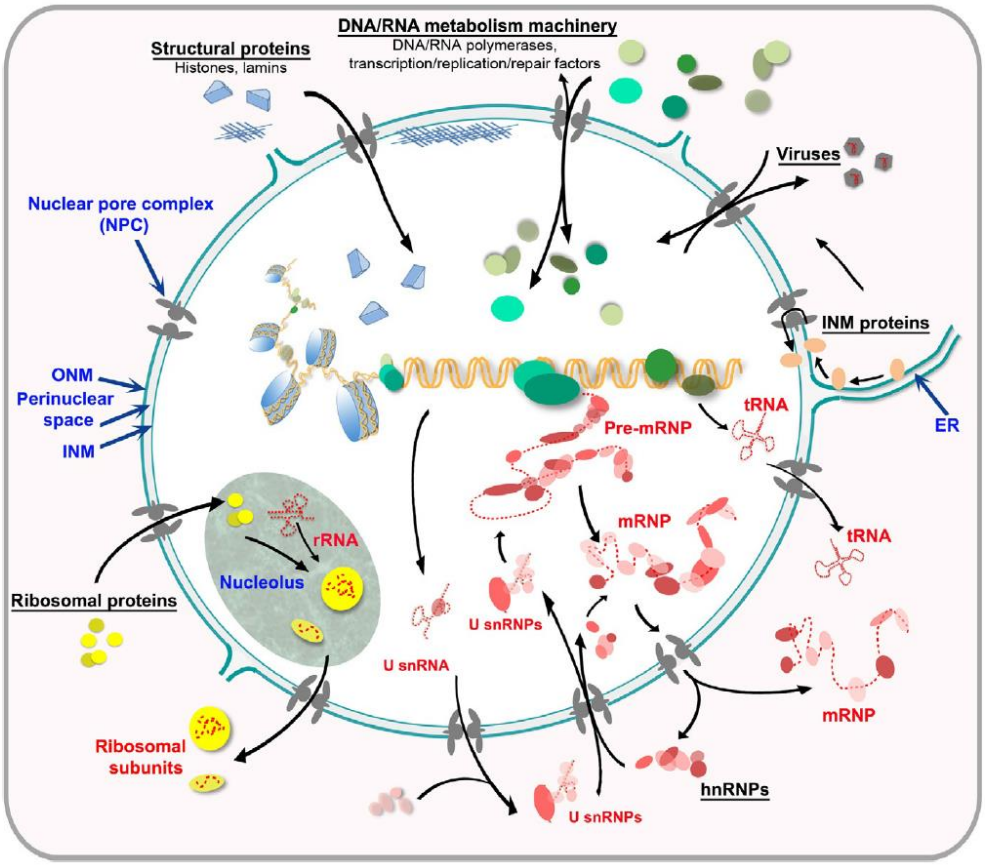

Figure 1.1: Overview of NPC-mediated transport across the nuclear envelope. The NPCs are the sole passages between the nucleoplasm and the cytoplasm for a vast number of proteins and RNA–protein complexes. The main nuclear processes are depicted, *e.g.* chromatin assembly, DNA metabolism and ribosome biogenesis. ONM, outer nuclear membrane; INM, inner nuclear membrane; and ER, endoplasmic reticulum. Figure reproduced from Floch, Palancade and Doye (2014)[12].

The following pages shall familiarize the interested reader with the structure and functions of the nuclear pore complex. This introductory part is thereby not an exhaustive review and the reader seeking for in-depth discussion of the various aspects of the NPC and NCT are referred to several excellent reviews[2,5,12–17].

1.1.1 Structure and Function of the NPC

The NPC is an enormous complex of ~30 different proteins[6,18] (nucleoporins; Nups) that are present in multiple copies and organized in stable subcomplexes[19]. About half of the Nups by mass contain structured domains (mainly α-solenoid and β-propeller folds) which act as NPC scaffold[5]. The other half comprises intrinsically disordered, phenylalanine-glycine (FG) rich domains that are involved *inter alia* in the NCT.

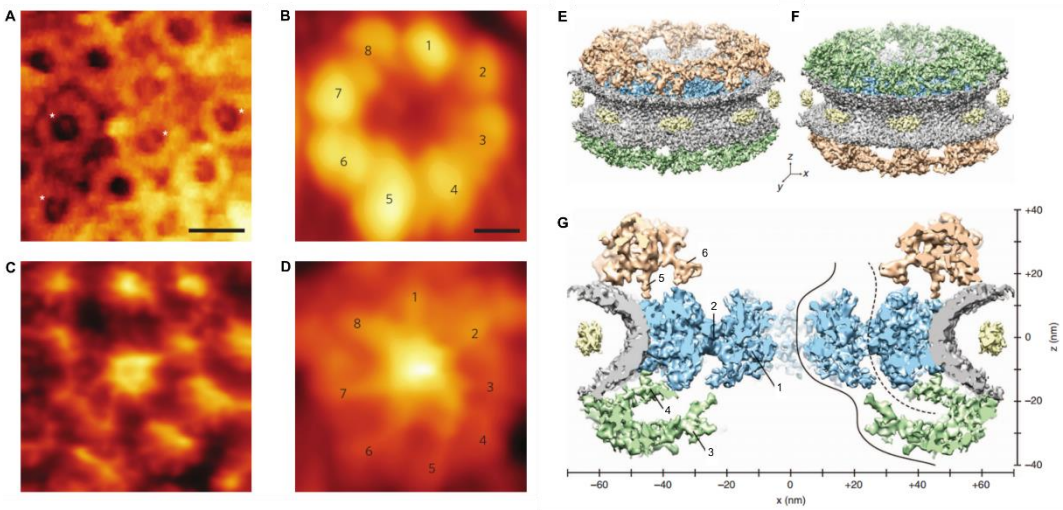

Figure 1.2: Global structure of the native *Xenopus leavis* NPC. **A-D**, High-speed AFM images of the cytoplasm-facing, outer nuclear membrane (**A** and **B**; scale bars 100 nm and 25 nm, respectively) and the nucleoplasm-facing, inner nuclear membrane (**C** and **D**; same scale as **A** and **B**, respectively). Overview image **A** reveals the close-packing of NPCs perforating the NE of *Xenopus laevis* (~50 NPC/µm^2). White stars in **A** indicate clogged pores with large cargoes-in-transit. Numbers in **B** and **D** indicate the eight cytoplasmic and nuclear (fusing into a distal ring) filaments, respectively. **E-F**, Cryo-electron tomographs of the cytoplasmic ring (gold; CPR), the nucleoplasmic ring (green; NPR) and the spoke ring (blue; SR); the nuclear envelope is depicted in grey. The central cross-section in **G** shows how the central channel ring (1) is attached to the SR (2) and how linker structures protrude from the NPR (3 and 4), as well as from the CPR (5). Putative position of the Nup214/Nup88 complexes is denoted by (6). Images **A-D** reproduced from Sakiyama *et al.* (2016)[20] and **E-G** modified from Eibauer *et al.* (2015)[21].

Although the number of polypeptide copies is variable and the size differs between species, overall NPC assembly follows a highly conserved, triple ring structure with an eightfold rotational symmetry[22,23]:

1. Eight peripheral filamentous structures extend from the outer ring on the cytoplasmic side[24] by ~35 – 50 nm [refs. 25, 26] (Figures 1.2A, B and 1.3). These cytoplasmic filaments in *Xenopus laevis* are built-up by three FG rich nucleoporins (FG Nups; Nup214, Nlp1 and Nup358), implicated in specific interactions with soluble nuclear transport receptors[27], in selective processes of the Ran-GTPase cycle, in cytoskeleton tethering and in the initiation of translation[14].

2. On the nucleoplasm-facing side, eight nuclear filaments protrude from the outer ring into the nucleoplasm[24] by ~50 – 75 nm [refs. 25, 28] and fuse into the distal nuclear basket (Figures 1.2 C, D and 1.3). Composed by two FG Nups (Nup153 and Nup50) and the nucleoporin Trp, the nuclear basket

is an interaction site for NTRs[27] involved in transcriptional regulation and chromatin stability[14].

3. Encompassed by the outer rings and the peripheral filaments, a central ring assembly surrounds an aqueous channel of ~50 nm width and of ~40 nm height (Figures 1.2E-G and 1.3)[25,26,28]. This central framework is symmetrical around the mirror plane of the NPC and constituted by four major groups of Nups. The inner ring Nups build the structural core, the transmembrane Nups anchor the NPC to the NE, the linker Nups interconnect the outer rings with the central ring and the central FG Nups contribute to the selective transport barrier that regulates the NCT through the central aqueous channel[29,30].

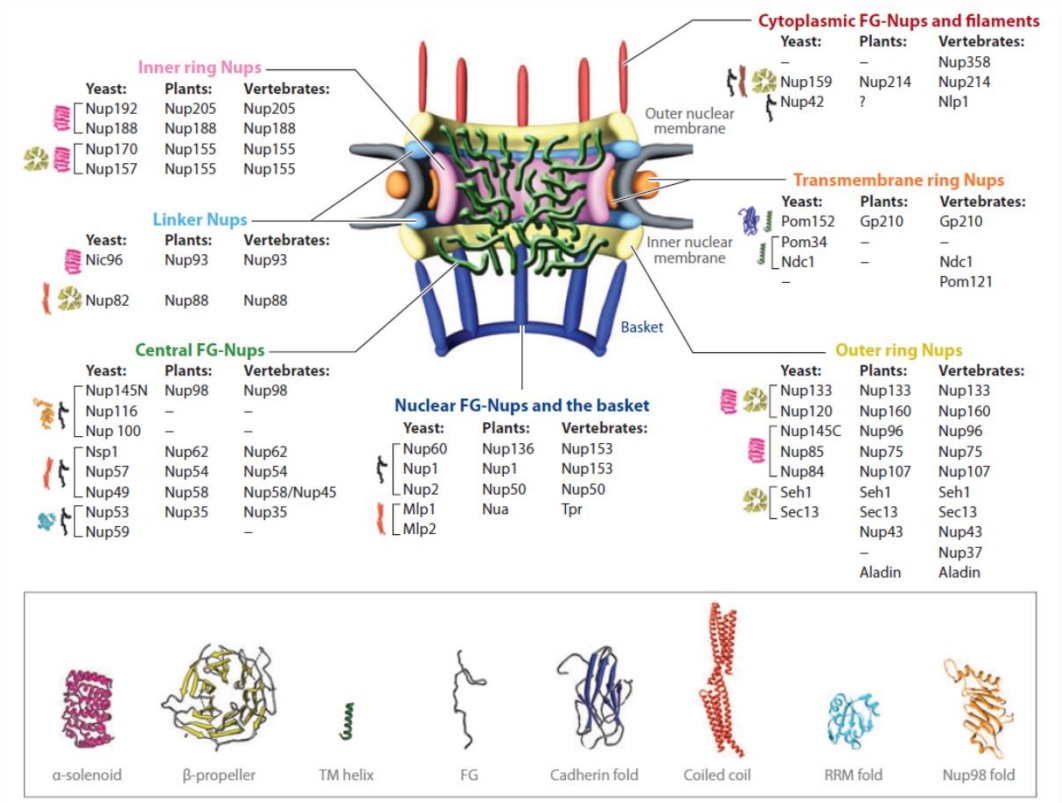

Figure 1.3 Yeast, plant and vertebrate Nups are arranged according to their position and structural features. The core is composed symmetrically by the central FG Nups, the outer ring Nups, linker Nups, inner ring Nups and transmembrane ring Nups. The FG Nups and filaments on the cytoplasmic and the basket on the nuclear side are the asymmetric parts of the NPC. The outer and inner nuclear membranes are depicted in grey. The structural motifs next to each Nup refer to their predicted protein fold in yeast and are described in the legend. Image reproduced from Grossman, Medalia and Zwerger (2012)[30].

1.1.2 Phenylalanine Glycine Rich Nucleoporins (FG Nups)

The inner wall of the NPC is lined with 11 different nucleoporins[31] (Figure 1.3; Table 1.1) each containing 150 – 700 amino acid long[18], intrinsically disordered[32] FG rich (5 to 50 repeats)[33] domains that emanate to explore the aqueous central channel. Due to the eightfold rotational symmetry of the NPC, FG Nups are assumed to exist in multiple copies of 8 and are classified by their repeating FG motifs (FxFG, GLFG or FG; Table 1.1). FG Nups associated with the peripheral filaments are biased towards the cytoplasmic[34] (Nup358, Nup214 and Nlp1) and nucleoplasmic[35] (Nup153 and Nup50) side, while the central FG Nups[36–38] (Nup98, Nup62, Nup54, Nup58/45 and Nup35) are thought to be distributed symmetrically around the central plane. In total, ~200 – 450 FG domains contribute ~3000 – 5000 FG repeats *per* NPC which share the ability to interact with soluble nuclear transport receptors in a multispecific manner[33]. Central FG Nups were identified to play a key role for the NPC transport functionality and are considered to be essential for maintaining active NCT as well as the passive permeability barrier[39]. Characteristics of FG Nups from human and yeast (Figure 1.3) used in the here presented work are listed in Table 1.1 (more information can be found in the Appendix of Chapter 2).

Table 1.1: Copy number of central FG nucleoporins. Values are taken from Peleg *et al.* (2010)[31].

FG Nup	# FG domain copies *per* NPC	# FG repeats *per* domain	Most abundant repeat motif
yNsp1	32	35	FxFG
hNup98	8	45	FG
hNup 153	8	39	FxFG, FG

1.2 Nucleocytoplasmic Transport

The bidirectional nucleocytoplasmic transport across nuclear pore complexes is orchestrated by nuclear transport receptors[2,5]. Essential proteins destined for nuclear import or export contain short peptide sequences known as nuclear localization signal (NLS; NLS-cargo) or nuclear export signal (NES; NES-cargo) which are recognized by the respective NTRs[40,41]. Loaded transport receptors ferry their specific cargo through the NPC *via* their multivalent interaction with FG domains within the NPC[42–44]. This specific NTR mediated NCT through NPCs shows some remarkable properties. Despite the ~50 nm-diameter central channel, unspecific cargo is rejected from passage by a soft barrier that intensifies gradually (~10 % per kD) with increasing mass from ~10kD (or a diameter of ~3 nm) onwards[45]. In contrast, cargo in complex with NTRs can reach ~39 nm [ref. 46] and still

translocate through the NPC in a facilitated manner. Although the dwell time of such cargo complexes is ~5 ms [ref. 47], translocation rates of ~1 kHz *per* pore have been measured[48], indicating the high parallelization of the nucleocytoplasmic transport, *i.e.* different cargo complexes can translocate through a single NPC at the same time. Specific cargo complexes accumulate thereby orders of magnitude faster than passively diffusing molecules, even against concentration gradients[49]. Moreover, transport of specific molecules through the NPC itself is an equilibrium process[50,51]. Energy beyond k_bT is only required to impart transport directionality[52] and cargo release[53]. The biochemical details of GTP-dependent transport cycles and possible *modi operandi* of the FG Nup transport barrier will be discussed in the subsequent sections.

1.2.1 Biochemistry of Nuclear Import and Export

The best characterized transport pathway is the import of NLS-cargo by the classical import receptor Karyopherinβ1 (Kapβ1, 100kD; also called Importinβ1 or Impβ1), a member of the Karyopherinβ family which share a N-terminal RanGTP-binding domain. Kapβ1 binds NLS-cargo either directly[54] or *via* the adaptor protein Karyopherinα (Kapα, 60 kD; Figure 1.4A, step 1)[55–57]. In general, use of adaptors amplifies the range of NLS-cargoes, which Kapβ1 can import. The heterodimer Kapβ1/Kapα associates strongly ($K_D \approx 10^{-8}$ M) by means of the N-terminal Importinβ binding (IBB) domain of Kapα[58]. This increases the affinity of Kapα towards NLS-cargo, since the IBB domain is an auto-inhibitory domain that mimics a NLS-motif and shares a common binding pocket with NLS-cargo on Kapα[59]. The heterotrimer complex Kapβ1/Kapα/NLS-cargo then translocates through the NPC *via* multivalent interactions of Kapβ1 with FG Nups[42–44]. On the nucleoplasmic side, the IBB domain is outcompeted by the small Ras-related nuclear protein RanGTP (a GTPase of the Ras family) and the Kapα/NLS-cargo complexe dissociates from Kapβ1 (Figure 1.4A, step 2)[2,60,61]. NLS-cargo is released from Kapα by the auto-inhibitory activity of its IBB domain, which loops back and competes for binding at the major NLS binding site. On some occasions, Nup50 is employed to catalyze the NLS-cargo release[62].

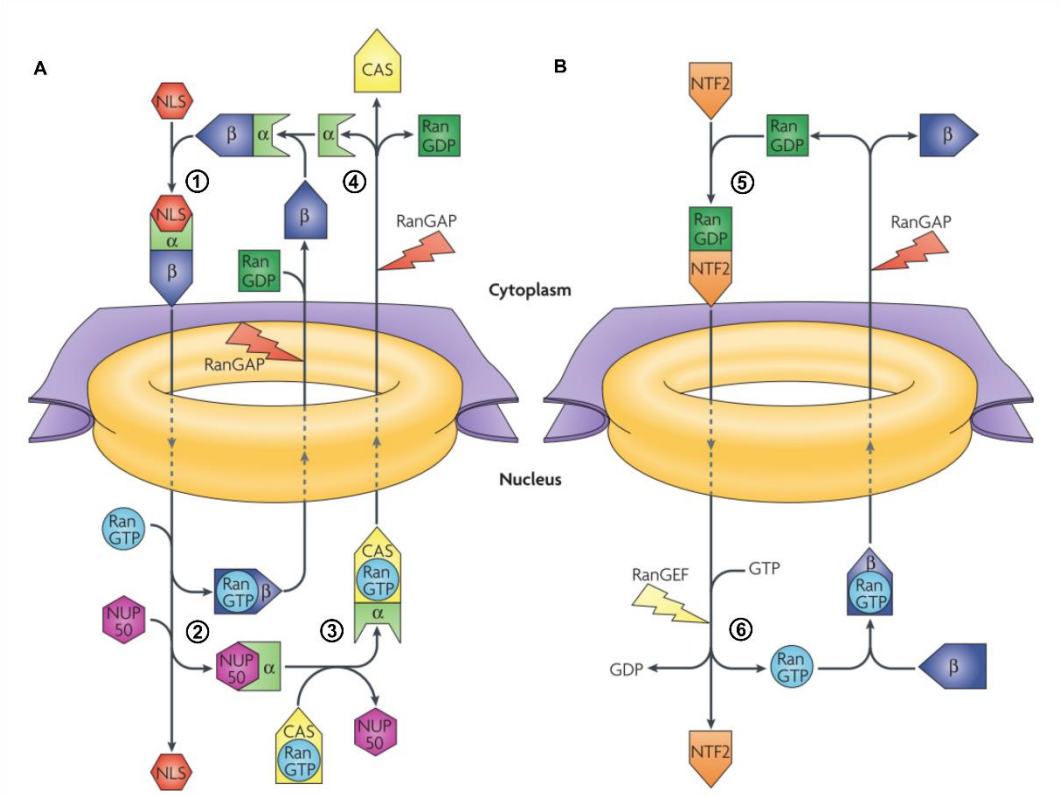

Figure 1.4: Biochemical mechanism of GTP-dependent nucleocytoplasmic import. **A**, the Karyopherinβ1 (Kapβ1) mediated cargo import and **B**, the NTF2 dependent Ran cycle. (**1**) Karyopherinα (Kapα) in complex with (Kapβ1) binds NLS-cargo. Passage of the Kapβ1/Kapα/NLS-cargo complex through the NPC is mediated by Kapβ1 binding to FG Nups. (**2**) In the nucleus, RanGTP disrupts the Kapβ1/Kapα heterodimer and Nup50 catalyzes the cargo release from Kapα. (**3**) Kapβ1/RanGTP shuttles back into the cytoplasm, whereas Kapα is recycled by its nuclear export factor CAS. (**4**) In the cytoplasm, the GTPase activation protein RanGAP stimulates the hydrolysis of RanGTP to RanGDP which dissociates from Kapα and Kapβ1. (**5**) RanGDP is ferried back to the nucleus by NTF2, where it is recharged into RanGTP by the chromatin-bound nucleotide exchange factor RanGEF (**6**). Figure reproduced and modified from Stewart (2007)[2].

While the Kapβ1/RanGTP complex is free to shuttle back to the cytoplasm, Kapα recycling requires its nuclear export receptor, which has been termed cellular apoptosis susceptibility gene (CAS)[63]. CAS binds to importin alpha only in the presence of RanGTP, forming an CAS/RanGTP/Kapα complex which is able to translocate through the NPC (Figure 1.4A, step 3)[64]. The RanGTP dependence of export receptor (CAS) to NES-cargo (Kapα) binding is the regulating step of nuclear export. On the cytoplasmic side, hydrolysis of RanGTP to RanGDP catalyzed by the GTPase-activating protein RanGAP within the cytoplasmic filaments causes the CAS/RanGTP/Kapα complex to dissociate into Kapα, CAS and RanGDP and the Kapβ1/RanGTP complex into Kapβ1 and RanGDP (Figure 1.4A, step 4)[65,66]. Kapα and Kapβ1 are then available for a new import cycle. Hydrolysis of RanGTP to RanGDP ($\Delta G \approx -33$ kJmol^{-1}), is the only irreversible process in the transport cycle.

Yet this free energy does not drive the facilitated transport through the NPC *per se* - which was shown to follow Brownian motion and hence is non-directional - but rather acts to release NLS-cargo and NES-cargo in their respective compartments against concentration gradients.

As NLS-cargo release and NES-cargo export both depend on binding of RanGTP, directionality of the transport requires a steep gradient of RanGTP across the NE[67,68], *e.g.* higher concentration of RanGTP in the nucleoplasm increases the probability of NLS-cargo release by RanGTP to Kapβ1 binding. Therefore, the pool of RanGTP requires constant replenishment, since on average *per* imported NLS-cargo two RanGTPs and *per* exported NES-cargo one RanGTP are ferried to the cytoplasm. RanGDP is therefore actively transported into the nucleus by its specific transport factor NTF2 (Figure 1.4B, step 5)[69,70] where it is recharged to RanGTP by the chromatin-bound guanine exchange factor RanGEF (Figure 1.4B, step 6)[71]. The asymmetric distribution of RanGAP and RanGEF establishes a ~200x – 1000x higher concentration of RanGTP in the nucleoplasm compared to the cytoplasm, although RanGTP and RanGDP are principally both small enough to freely diffuse through the NPC[72].

1.2.2 Multivalent Interactions of Karyopherinβ1 and FG Domains

Despite their low sequence identity of 10 – 20 %, members of the Karyopherinβ family share similar structure (all contain multiple HEAT repeats), molecular weights (90 – 150 kD) and isoelectrical points (4 – 5). The crystal structure of human Kapβ1, the transport receptor used in the present work, reveals an alpha-solenoid fold composed of 19 HEAT repeats, each consisting of two (A and B) anti-parallel alpha helices[42,58,73]. The repeats are arranged such that the helices A define the convex and helices B describe the concave surface of the overall falcate-shaped Kapβ1 protein. Crystal structures of Kapβ1 bound to RanGTP[73] and to the IBB domain[58] identify the N-terminal and C-terminal half of the inner (concave) surface as binding sites, respectively. The global confirmation of Kapβ1 seems thereby to be ligand dependent as it undergoes a transition from an open and flexible towards a more closed and rigid arrangement for both, the RanGTP and the IBB domain[74,75]. Moreover, 10 potential binding pockets for FG motifs have been predicted on the outer (convex) surface, of which 7 were confirmed experimentally[43,44,76]. The hydrophobic interaction between FG domains and Kapβ1 is therefore considered to be multivalent, since both binding partners bear multiple binding sites[77]. It is this multivalency which leads to collective binding affinities in the nanomolar range ($K_D \approx 10^{-9} – 10^{-7}$ M)[43,78–80], as the binding between

a single FG repeat to a respective binding pocket on Kapβ1 is usually very weak (K_D ≈ 10^{-3} M)[81]. The effective K_D values of Kapβ1 binding to FG Nups relevant to the here presented study are listed in Table 1.2.

Table 1.2: K_D values of Kapβ1 binding to FG Nups [10^{-9} M].

Nsp1	Nup98	Nup153
110 ± 30 [79]	∼50 and ∼3500 [11]	∼130 and ∼2300 [11]
340 ± 60 and 5610 ± 198 [82]		1.1 ± 0.1 [43]
		9 ± 2.5 [78]

1.2.3 Transport Models

As discussed above, cargo-Kap complexes pass through the NPC by means of transport receptor affinity towards FG repeats[42–44]. Single FG domains are able to bind ∼20 of these Kaps in a multispecific manner[33,83], *i.e.* one FG domain can specifically bind to many Kaps. The karyopherins are able to bind multiple FG repeats in a promiscuous way themselves[43,44,76], leading to highly multivalent interaction, *e.g.* one Kap could interact with many FG motifs of one FG domain or one Kap could transiently bind single FG motifs on many different FG domains, in both cases imparting strong avidity[81]. Both, FG domains (∼10^{-2} M) in[84] and Kaps (∼10^{-4} M) around[85] the NPC are highly abundant. Regardless of the high FG repeat density and although cargo translocation is a purely stochastic process, ∼100 – 500 parallel translocation events account for a molecular flux of up to ∼80 MDa per NPC and second[7,86]. This highlights one of the main conundrums in the field:

Which mechanism of the central FG Nups allows for such high transport rates and at the same time can account for its arguably unparalleled selectivity?

The major challenge to address this question conclusively lies in resolving the ensemble conformation of the central FG Nups and hence, how their collective morphology correlates with function. This shortcoming of structural determination is mainly owed to the high flexibility and low electron density of the FG domains. Thus, in order to explain the NPC barrier functionality based on FG domain organization, several *in vitro* studies have been performed[6–11]. Motivated by the findings of these efforts, various models have been proposed to explain the nucleocytoplasmic transport (Figure 1.5). The chronological overview in the following shall help to understand the evolution of the main models.

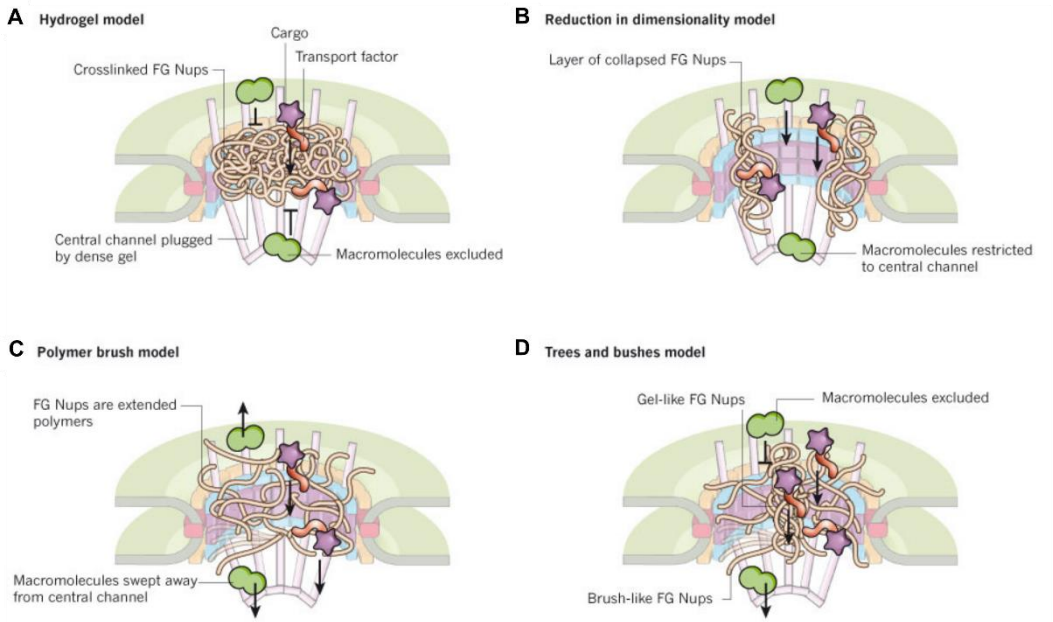

Figure 1.5: Main models of nucleocytoplasmic transport. **A**, The selective phase or hydrogel model suggests that FG Nups polymerize into a gel-like meshwork through which transport receptors pass by binding to the FG Nups and dissolving the nodes.[7] **B**, The reduction of dimensionality model proposes that FG Nups collapse after binding by nuclear transport receptors to form a cohesive surface along the walls of the central channel. Inert macromolecules are only able to pass through the central channel, NTRs can slide along the FG domain layer.[8] **C**, The polymer brush model marks a nanomechanical expansion of the Browninan affinity gate[6]. FG domains diffuse around their tether, and other molecules are excluded from this region. NTRs pass through the pore by binding to the FG repeats. FG domains adopt a brush-like conformation that collapses once transport receptors have bound other molecules.[9] **D**, In the trees and bushes or forest model, FG domains are supposed to fall in two categories of disordered filaments: collapsed coils, which are gel-like; and extended coils, which are brush-like. NTRs can pass through both configurations, but macromolecules are excluded.[10] Figure reproduced and modified from Grünwald, Singer and Rout (2011)[87].

The Browninan Affinity Gating Model

First proposed by Rout *et al.* (2000)[6]:

The "Brownian Affinity Gating Model" is based on the loss in a molecule's entropy upon entering the nanoconfined central NPC channel. Accordingly, the entropic penalty for translocation rises with the size of the cargo and the NPC represents an effectively impermeable virtual gate for large molecules. The densely packed FG Nups occupy additional volume in the center and at the extremities of the central channel, thereby adding up to the entropic barrier. FG domains are not assumed to adopt an ensemble conformation but rather act as entropic bristles, *i.e.* driven by thermal energy FG domains fluctuate and explore the volumes around their anchoring points and therefor repel each other and cargo[84]. In this scenario, transport receptors lower the entropic barrier by the enthalpy gain of FG-NTR interactions, increasing the probability of entering in and passing through the NPC. While this gating model can account for the observed differences in

accumulation speed of similarly sized NTRs and inert molecules[49], it fails to explain the fast transport rates under reasonable assumptions of Kap on- and off-rates[53].

The Selective Phase Model

First proposed by Ribbeck and Görlich (2001)[7]:

The "Selective-Phase Model" suggests that the FG domains assemble into a sieve-like meshwork based on inter-FG-repeat interactions (Figure 1.5A). On the other hand, by their affinity to FG, multivalent NTRs are hypothesized to compete locally with the FG-FG nodes, thereby dissolving into this hydrogel regardless of its mesh size. Even though such saturated gels - when all FG motifs are cross-linked - were shown to reproduce the permeability barrier of the NPC, several uncertainities remain[88,89]. Hydrogel formation was established under non-physiological conditions and the formed gels neither interacts with themselves nor with FG domains under physiological conditions[90,91]. Experimental data suggest distinct spatial routes through the NPC for passively diffusing and actively transported cargo[92]. It is not clear how a meshwork could account for such a spatial separation. Moreover, incubation with transport receptors after gel formation hinders the diffusion of NTR-cargo[89], in contrast to observations in cells which reveal a Kap dependent reduction of the NPC interaction time[51].

The Reduction of Dimensionality Model

First proposed by Peters *et al.* (2005)[8]:

The "Reduction of Dimensionality Model" (ROD) emanates from the notion that the overall FG domain conformation is sensitive to Kap binding (Figure 1.5B). The intracellular concentration of Kaps (*e.g.*~10 µM Kapβ1)[85] exceed the number of NPCs and it is likely that the FG domains are saturated at steady-state, *i.e.* FG domains are thought to remain permanently collapsed, thereby forming a hydrophobic FG layer which is lining the central NPC channel[84,93]. In ROD, transport receptors attach to this cohesive FG surface but retain lateral mobility due to the multivalent nature of the FG-NTR interaction. Therefore, NTR mediated translocation through the NPC is depicted as a two-dimensional random walk along the central channel wall. In contrast, passage of inert molecules resembles restricted three-dimensional Brownian motion through a narrow tube in the channel center. ROD rationalizes the observation that Kap-cargo complexes accumulate faster than passively diffusing molecules by these two suggested modes of translocation[94] and is in agreement with the observed distinct pathways for Kap-facilitated transport along the channel wall and passive diffusion preferentially through the central channel[92].

The Polymer Brush Model

First proposed by Lim *et al.* (2007)[9]:

The "Polymer Brush Model" implies an overall polymer brush-like conformation of the disordered FG domains (Figure 1.5C), *i.e.* due to the close proximity of their anchoring points, size-exclusion causes the FG domains to stretch away from the NPC[95,96]. Peripheral FG Nups are thought to form an entropic barrier which repels inert molecules access to the central NPC channel[97]. But in contrast to the "Brownian Affinity Gate Model", FG domains undergo a conformational transition upon binding with transport receptors. Namely, they reversibly collapse toward their base at the NPC causing the NTR-cargo complex to be drawn into the pore. Consecutive NTR unbinding leads to a re-extension of the FG domains and hence to a re-established entropic barrier. The NTR-cargo is then thought to randomly move from one FG domain to the next where each binding and unbinding event leads to a local collapse and a re-extension, respectively. This model explains barrier integrity and fast transport rates, since the relaxation times of disordered protein domains are orders of magnitudes faster[98]. It also rationalizes the observed transport path in NTR mediated NCT along the wall of the central channel[92]. Nevertheless, the observed collapse was experimentally induced at low, non-physiological Kap concentrations and it has been recently shown that the collapse is rectified at increasing receptor concentrations[99]. Furthermore, the asymmetrical disposition of FG Nups exhibiting different properties can interfere with a brush-like conformation and the collapse-extension mechanism may not be present throughout the NPC[10].

The Forest Model

First proposed by Yamada *et al.* (2010)[10]:

The "Forest Model" combines and extends the former models by considering the presents of different structural categories amongst FG domains (Figure 1.5D). Mainly based on their ratio of charged to hydrophobic amino acids, three distinct domain conformations were proposed: 1) a cohesive, globular collapsed coil (low ratio), 2) a dynamic, non-cohesive, extended coil (high ratio) and 3) FG domains featuring a bimodal distribution between state 1) and 2), thus resembling the canopy and trunk of a tree. The "Forest Model" suggests that the collapsed coils (or shrubs) and the trees form two distinct transport zones: Zone 1 is the central channel flanked by cohesive canopies that cohere into a gel-like state. Zone 2 is defined as the space of the trunks, reminiscent of a molecular brush, which is lined by shrubs. While both zones permit passive diffusion of small molecules only zone 1 can accommodated large cargo. The entrance of zone 2 is surrounded by

extended coils that act as entropic bristles and only allows transport receptors (or NTRs carrying small cargo) access to zone 2. Notwithstanding that the forest model basically combines all previous models, it is in contrast to single molecule experiments with native NPCs showing that passively diffusing molecules localize preferentially in the central channel[92].

The Kap-centric Model

First proposed by Kapinos *et al.* (2014)[11]:

The "Kap-centric Model" considers Kaps as *bona fide* constituents of the NPC transport barrier and can be understood as Kap-centric extension of the ROD model (Figure 1.6), *i.e.* the occupancy of the FG domains by Kaps regulates the layer conformation and determines the level of multivalency between FG repeats and transport receptors. It has been shown that collapsed FG domain layers undergo a re-extension (and even swelling beyond their initial height) as the concentration of interacting Kaps reaches physiological levels[85,99]. The affinity of the Kaps at low concentrations ($K_D \approx 10^{-7}$ M; slow phase; Figure 1.6 middle) drops substantially with rising Kap concentrations as the NTRs start to compete for the limited number of FG motifs inside the FG domain layer[100]. Incorporation of Kaps into the FG domain layer is therefore accompanied by the emergence of a small, transiently bound Kap fraction ($K_D \approx 10^{-5}$ M; fast phase; Figure 1.6 left) on top of the strongly bound species. This Kap-centric mechanism may resolve several incoherent aspects of purely FG-centric barrier models, *e.g.* it explains decreasing translocation times for increasing Kap concentration[51] and the functional robustness of the NPC against substantial FG domain deletion[101]. Further, it has been shown that transport receptors are an indispensable barrier reinforcement in artificial NPCs[102]. Given the high cellular Kap concentration[85] and their FG domain affinity[43,78–80], it is reasonable to assume that NPCs are filled[103] and not deplete from Kaps at steady state.

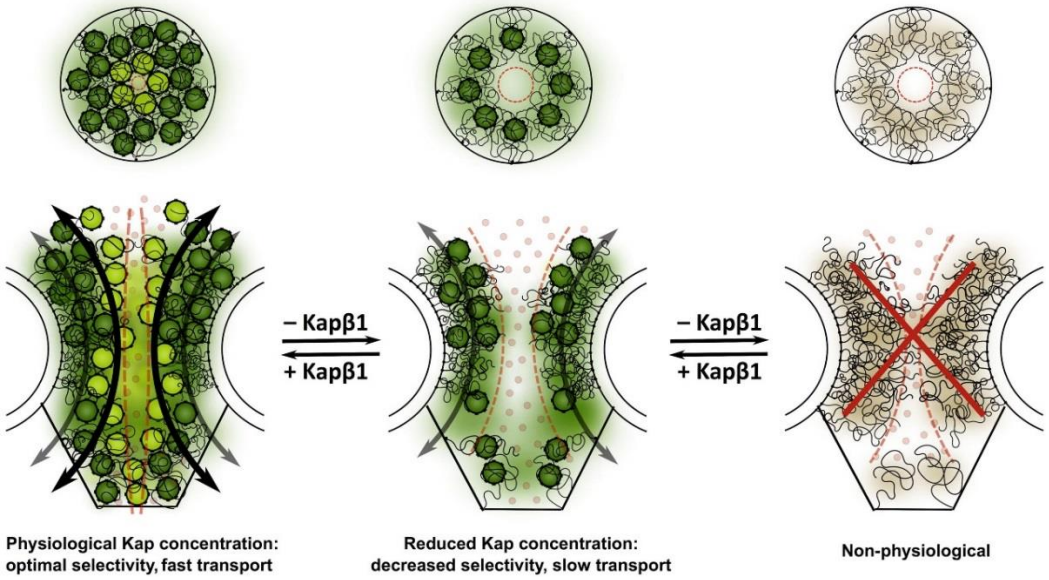

Figure 1.6: The "Kap-centric model": NPCs operated by Kap-centric control. Kaps are integral constituents of the NPC at physiological steady-state conditions and form as such an essential component of the NPC barrier functionality. **Left***:* Physiological Kap concentrations lead to a swelling of the FG domains and a narrowing of the central channel. The majority of Kaps are strongly bound ($K_D \approx 10^{-7}$ M, dark green) and limit the availability of FG domains for the smaller, transiently bound fraction ($K_D \approx 10^{-5}$ M, light green) which therefore promote fast passage through the central plane of the NPC. **Middle**: A reduction of the Kap concentration renders the NPC more penetrable to unspecific molecules because of widening of the aqueous channel. Additionally, lack of competing Kaps increases the availability of free FG repeats and slows down the translocation of Kaps **Right***:* A NPC fully depleted from any transport receptors is non-physiological. Figure reproduced from Kapinos et al. (2014) .

1.3 Aim of the Thesis

During my PhD from 2013 onwards, work from our group[11,100,104] contributed substantially to the development of a picture (the "Kap-centric Model") that reconciles both mechanistic and kinetic requirements of the NPC selectivity barrier. By incorporating transport receptors as intrinsic constituents, this holistic biochemical view allows various ambiguities of former transport models to be resolved (see Section 1.2.3).

However, these studies were performed on planar surfaces and are therefore lacking spatial confinement as a key characteristic of the NPC. The present thesis is therefore an effort to test this model under nanoscale confinement. It is thereby not the first approach to engineer an artificial NPC-like sorting machine. Jovanovic-Talisman *et al.*[102] managed already in 2009 to reconstitute the barrier functionality in membranes perforated by nanopores and anticipated that Kaps are indispensable to establish selectivity. Nevertheless, this was a bulk study performed by means of confocal fluorescence microscopy, which did not permit to draw any conclusions about the mechanistic details of the selectivity barrier. In 2011, collaborative efforts of our group funneled in the formation of individual artificial NPC. Although Kowalczyk *et al.*[105] were able to implement selectivity and to measure translocation speeds comparable to native NPC on a single molecule level, they did not consider the Kap dependence yet.

The objective of this thesis is to study selective transport on NPC-like bio-interfaces. For the sake of comparability, this demands a protein immobilization strategy which is applicable on planar surfaces as well as nanoconfined volumes under physiological conditions. Furthermore, it shall simulate the *in vivo* situation better than assays formed on bare gold or glass. This is the scope of **Chapter 2** and **Chapter 3**, where I report how to use supported lipid bilayers as substrate for FG Nup immobilization on planar surfaces and how these are interacting with Kapβ1. Moreover, it requires solid-state nanopores that resemble the geometry of native NPCs. The reproducible fabrication and characterization of such geometries made from glass nanocapillaries is covered in **Chapter 4**. Subsequently, I conclude on these efforts to build artificial NPCs from Chapter 2, 3 and 4 and show how they can be combined in future in the conclusion and outlook **Chapter 5.**

1.4 References

1. Terry, L. J., Shows, E. B. & Wente, S. R. Crossing the nuclear envelope: hierarchical regulation of nucleocytoplasmic transport. *Science* **318,** 1412–1416 (2007).
2. Stewart, M. Molecular mechanism of the nuclear protein import cycle. *Nat. Rev. Mol. Cell Biol.* **8,** 195–208 (2007).
3. Reichelt, R. *et al.* Correlation between structure and mass distribution of the nuclear pore complex and of distinct pore complex components. *J. Cell Biol.* **110,** 883-894 (1990).
4. Maul, G. G. & Deaven, L. Quantitative determination of nuclear pore complexes in cycling cells with differing DNA content. *J. Cell Biol.* **73,** 748–760 (1977).
5. Wente, S. R. & Rout, M. P. The nuclear pore complex and nuclear transport. *Cold Spring Harb. Perspect. Biol.* **2,** a000562-1– a000562-19 (2010).
6. Rout, M. P. *et al.* The Yeast Nuclear Pore Complex. *J. Cell Biol.* **148,** 635–652 (2000).
7. Ribbeck, K. & Görlich, D. Kinetic analysis of translocation through nuclear pore complexes. *EMBO J.* **20,** 1320–1330 (2001).
8. Peters, R. Translocation Through the Nuclear Pore Complex: Selectivity and Speed by Reduction-of-Dimensionality. *Traffic* **6,** 421–427 (2005).
9. Lim, R. Y. *et al.* Nanomechanical basis of selective gating by the nuclear pore complex. *Science (80-.).* **318,** 640–643 (2007).
10. Yamada, J. *et al.* A Bimodal Distribution of Two Distinct Categories of Intrinsically Disordered Structures with Separate Functions in FG Nucleoporins. *Mol. Cell. Proteomics* **9,** 2205–2224 (2010).
11. Kapinos, L. E., Schoch, R. L., Wagner, R. S., Schleicher, K. D. & Lim, R. Y. H. Karyopherin-centric control of nuclear pores based on molecular occupancy and kinetic analysis of multivalent binding with FG nucleoporins. *Biophys. J.* **106,** 1751–1762 (2014).
12. Floch, A. G., Palancade, B. & Doye, V. *Fifty years of nuclear pores and nucleocytoplasmic transport studies: Multiple tools revealing complex rules*. *Methods in Cell Biology* **122,** 1–40 (2014).
13. Chatel, G. & Fahrenkrog, B. Dynamics and diverse functions of nuclear pore complex proteins. *Nucleus* **3,** 162–171 (2012).
14. Strambio-De-Castillia, C., Niepel, M. & Rout, M. P. The nuclear pore complex: bridging nuclear transport and gene regulation. *Nat. Rev. Mol. Cell Biol.* **11,** 490–501 (2010).

15. Raices, M. & D'Angelo, M. A. Nuclear pore complex composition: a new regulator of tissue-specific and developmental functions. *Nat. Rev. Mol. Cell Biol.* **13,** 687–699 (2012).

16. Lim, R. Y. H., Huang, B. & Kapinos, L. E. How to operate a nuclear pore complex by Kap-centric control. *Nucleus* **6,** 366–372 (2015).

17. Beck, M. & Hurt, E. The nuclear pore complex: understanding its function through structural insight. *Nat. Rev. Mol. Cell Biol.* **18,** 73–89 (2016).

18. Cronshaw, J. M., Krutchinsky, A. N., Zhang, W., Chait, B. T. & Matunis, M. J. Proteomic analysis of the mammalian nuclear pore complex. *J. Cell Biol.* **158,** 915–927 (2002).

19. Anderson, D. J. & Hetzer, M. W. Nuclear envelope formation by chromatin-mediated reorganization of the endoplasmic reticulum. *Nat. Cell Biol.* **9,** 1160–1166 (2007).

20. Sakiyama, Y., Mazur, A., Kapinos, L. E. & Lim, R. Y. H. Spatiotemporal dynamics of the nuclear pore complex transport barrier resolved by high-speed atomic force microscopy. *Nat. Nanotechnol.* **11,** 717–724 (2016).

21. Eibauer, M. *et al.* Structure and gating of the nuclear pore complex. *Nat. Commun.* **6,** 7532-1–7532-9 (2015).

22. Unwin, P. N. T. & Milligan, R. A. A Large Particle Associated with the Perimeter of the Nuclear Pore Complex. *J. Cell Biol.* **93,** 63–75 (1982).

23. Akey, C. W. Interactions and structure of the nuclear pore complex revealed by cryo-electron microscopy. *J Cell Biol* **109,** 955–970 (1989).

24. Jarnik, M. & Aebi, U. Toward a more complete 3-D structure of the nuclear pore complex. *J. Struct. Biol.* **107,** 291–308 (1991).

25. Stoffler, D. *et al.* Cryo-electron tomography provides novel insights into nuclear pore architecture: Implications for nucleocytoplasmic transport. *J. Mol. Biol.* **328,** 119–130 (2003).

26. Beck, M. *et al.* Nuclear pore complex structure and dynamics revealed by cryoelectron tomography. *Science* **306,** 1387–1390 (2004).

27. Sabri, N. *et al.* Distinct functions of the Drosophila Nup153 and Nup214 FG domains in nuclear protein transport. *J. Cell Biol.* **178,** 557–565 (2007).

28. Beck, M., Lucić, V., Förster, F., Baumeister, W. & Medalia, O. Snapshots of nuclear pore complexes in action captured by cryo-electron tomography. *Nature* **449,** 611–615 (2007).

29. Alber, F. *et al.* The molecular architecture of the nuclear pore complex. *Nature* **450,** 695–701 (2007).

30. Grossman, E., Medalia, O. & Zwerger, M. Functional Architecture of the Nuclear Pore Complex. *Annu. Rev. Biophys.* **41,** 557–584 (2012).

31. Peleg, O. & Lim, R. Y. H. Converging on the function of intrinsically disordered nucleoporins in the nuclear pore complex. *Biological Chemistry* **391,** 719–730 (2010).

32. Denning, D. P., Patel, S. S., Uversky, V., Fink, A. L. & Rexach, M. Disorder in the nuclear pore complex: the FG repeat regions of nucleoporins are natively unfolded. *Proc. Natl. Acad. Sci. U. S. A.* **100,** 2450–2455 (2003).

33. Terry, L. J. & Wente, S. R. Flexible gates: dynamic topologies and functions for FG nucleoporins in nucleocytoplasmic transport. *Eukaryot. Cell* **8,** 1814–1827 (2009).

34. Paulillo, S. M. *et al.* Nucleoporin domain topology is linked to the transport status of the nuclear pore complex. *J. Mol. Biol.* **351,** 784–798 (2005).

35. Fahrenkrog, B. *et al.* Domain-specific antibodies reveal multiple-site topology of Nup153 within the nuclear pore complex. in *Journal of Structural Biology* **140,** 254–267 (2002).

36. Krull, S., Thyberg, J., Björkroth, B., Rackwitz, H.-R. & Cordes, V. C. Nucleoporins as components of the nuclear pore complex core structure and Tpr as the architectural element of the nuclear basket. *Mol. Biol. Cell* **15,** 4261–4277 (2004).

37. Solmaz, S. R., Chauhan, R., Blobel, G. & Melčák, I. Molecular architecture of the transport channel of the nuclear pore complex. *Cell* **147,** 590–602 (2011).

38. Chatel, G., Desai, S. H., Mattheyses, A. L., Powers, M. A. & Fahrenkrog, B. Domain topology of nucleoporin Nup98 within the nuclear pore complex. *J. Struct. Biol.* **177,** 81–89 (2012).

39. Strawn, L. A., Shen, T., Shulga, N., Goldfarb, D. S. & Wente, S. R. Minimal nuclear pore complexes define FG repeat domains essential for transport. *Nat. Cell Biol.* **6,** 197–206 (2004).

40. Boulikas, T. Putative nuclear localization signals (NLS) in protein transcription factors. *J. Cell. Biochem.* **55,** 32–58 (1994).

41. Xu, D., Farmer, A. & Chook, Y. M. Recognition of nuclear targeting signals by Karyopherin-β proteins. *Curr. Opin. Struct. Biol.* **20,** 782–790 (2010).

42. Bayliss, R., Littlewood, T. & Stewart, M. Structural basis for the interaction between FxFG nucleoporin repeats and importin-beta in nuclear trafficking. *Cell* **102,** 99–108 (2000).

43. Bednenko, J., Cingolani, G. & Gerace, L. Importin beta contains a COOH-terminal nucleoporin binding region important for nuclear transport. *J. Cell Biol.* **162,** 391–401 (2003).

44. Isgro, T. A. & Schulten, K. Binding Dynamics of Isolated Nucleoporin Repeat Regions to Importin-β. *Structure* **13,** 1869–1879 (2005).

45. Timney, B. L. *et al.* Simple rules for passive diffusion through the nuclear pore complex. *J. Cell Biol.* **215,** 57-76 (2016).

46. Panté, N. & Kann, M. Nuclear pore complex is able to transport macromolecules with diameters of about 39 nm. *Mol. Biol. Cell* **13,** 425–434 (2002).

47. Ma, J. & Yang, W. Three-dimensional distribution of transient interactions in the nuclear pore complex obtained from single-molecule snapshots. *Proc. Natl. Acad. Sci. U. S. A.* **107,** 7305–7310 (2010).

48. Ribbeck, K. & Gorlich, D. Kinetic analysis of translocation through nuclear pore complexes. *EMBO J.* **20,** 1320–1330 (2001).

49. Siebrasse, J. P. & Peters, R. Rapid translocation of NTF2 through the nuclear pore of isolated nuclei and nuclear envelopes. *EMBO Rep.* **3,** 887–892 (2002).

50. Yang, W., Gelles, J. & Musser, S. M. Imaging of single-molecule translocation through nuclear pore complexes. *Proc. Natl. Acad. Sci. U. S. A.* **101,** 12887–12892 (2004).

51. Yang, W. & Musser, S. M. Nuclear import time and transport effi ciency depend on importin beta concentration. *J. Cell Biol* **174,** 951–961 (2006).

52. Görlich, D., Panté, N., Kutay, U., Aebi, U. & Bischoff, F. R. Identification of different roles for RanGDP and RanGTP in nuclear protein import. *EMBO J.* **15,** 5584–5594 (1996).

53. Macara, I. G. Transport into and out of the nucleus. *Microbiol. Mol. Biol. Rev.* **65,** 570–594 (2001).

54. Cingolani, G., Bednenko, J., Gillespie, M. T. & Gerace, L. Molecular Basis for the Recognition of a Nonclassical Nuclear Localization Signal by Importin β. *Mol. Cell* **10,** 1345–1353 (2002).

55. Rexach, M. & Blobel, G. Protein import into nuclei: association and dissociation reactions involving transport substrate, transport factors, and nucleoporins. *Cell* **83,** 683–692 (1995).

56. Conti, E., Uy, M., Leighton, L., Blobel, G. & Kuriyan, J. Crystallographic Analysis of the Recognition of a Nuclear Localization Signal by the Nuclear Import Factor Karyopherin α. *Cell* **94,** 193–204 (1998).

57. Pemberton, L. F. & Paschal, B. M. Mechanisms of Receptor-Mediated Nuclear Import and Nuclear Export. *Traffic* **6,** 187–198 (2005).

58. Cingolani, G., Petosa, C., Weis, K. & Müller, C. W. Structure of importin-beta bound to the IBB domain of importin-alpha. *Nature* **399,** 221–229 (1999).

59. Kobe, B. Autoinhibition by an internal nuclear localization signal revealed by the crystal structure of mammalian importin α. *Nat. Struct. Biol.* **6,** 388–397 (1999).

60. Moroianu, J., Blobel, G. & Radu, A. Nuclear protein import: Ran-GTP dissociates the karyopherin alphabeta heterodimer by displacing alpha from an overlapping binding site on beta. *Proc. Natl. Acad. Sci. U. S. A.* **93,** 7059–7062 (1996).

61. Hieda, M. *et al.* A monoclonal antibody to the COOH-terminal acidic portion of Ran inhibits both the recycling of Ran and nuclear protein import in living cells. *J. Cell Biol.* **144,** 645–655 (1999).

62. Matsuura, Y. & Stewart, M. Nup50/Npap60 function in nuclear protein import complex disassembly and importin recycling. *EMBO J.* **24,** 3681–3689 (2005).

63. Kutay, U., Bischoff, F. R., Kostka, S., Kraft, R. & Görlich, D. Export of importin alpha from the nucleus is mediated by a specific nuclear transport factor. *Cell* **90,** 1061–1071 (1997).

64. Matsuura, Y. & Stewart, M. Structural basis for the assembly of a nuclear export complex. *Nature* **432,** 872–877 (2004).

65. Klebe, C., Bischoff, F. R., Ponstingl, H. & Wittinghofer, A. Interaction of the nuclear GTP-binding protein Ran with its regulatory proteins RCC1 and RanGAP1. *Biochemistry* **34,** 639–647 (1995).

66. Bischoff, F. R. & Görlich, D. RanBP1 is crucial for the release of RanGTP from importin β-related nuclear transport factors. *FEBS Lett.* **419,** 249–254 (1997).

67. Izaurralde, E., Kutay, U., Von Kobbe, C., Mattaj, I. W. & Gö Rlich, D. The asymmetric distribution of the constituents of the Ran system is essential for transport into and out of the nucleus. *EMBO J.* **16,** 6535–6547 (1997).

68. Nachury, M. & Weis, K. The direction of transport through the nuclear pore can be inverted. *Proc. Natl. Acad. Sci.* **96,** 9622–9627 (1999).

69. Ribbeck, K., Lipowsky, G., Kent, H. M., Stewart, M. & Gö Rlich, D. NTF2 mediates nuclear import of Ran. *EMBO J.* **17,** 6587–6598 (1998).

70. Bayliss, R. *et al.* Interaction between NTF2 and xFxFG-containing nucleoporins is required to mediate nuclear import of RanGDP. *J. Mol. Biol.* **293,** 579–593 (1999).

71. Renault, L., Kuhlmann, J., Henkel, A. & Wittinghofer, A. Structural Basis for Guanine Nucleotide Exchange on Ran by the Regulator of Chromosome Condensation (RCC1). *Cell* **105,** 245–255 (2001).

72. Kalab, P., Weis, K. & Heald, R. Visualization of a Ran-GTP Gradient in Interphase and Mitotic Xenopus Egg Extracts. *Science* **295,** 2452-2456 (2002).

73. Vetter, I. R., Arndt, A., Kutay, U., Görlich, D. & Wittinghofer, A. Structural View of the Ran–Importin β Interaction at 2.3 Å Resolution. *Cell* **97,** 635–646 (1999).

74. Fukuhara, N., Fernandez, E., Ebert, J., Conti, E. & Svergun, D. Conformational variability of nucleo-cytoplasmic transport factors. *J. Biol. Chem.* **279,** 2176–2181 (2004).

75. Conti, E., Müller, C. W. & Stewart, M. Karyopherin flexibility in nucleocytoplasmic transport. *Curr. Opin. Struct. Biol.* **16,** 237–244 (2006).

76. Liu, S. M. & Stewart, M. Structural Basis for the High-affinity Binding of Nucleoporin Nup1p to the Saccharomyces cerevisiae Importin-β Homologue, Kap95p. *J. Mol. Biol.* **349,** 515–525 (2005).

77. Milles, S. & Lemke, E. A. Mapping Multivalency and Differential Affinities within Large Intrinsically Disordered Protein Complexes with Segmental Motion Analysis. *Angew. Chemie Int. Ed.* **53,** 7364–7367 (2014).

78. Ben-Efraim, I. & Gerace, L. Gradient of increasing affinity of importin β for nucleoporins along the pathway of nuclear import. *J. Cell Biol.* **152,** 411–417 (2001).

79. Bayliss, R., Littlewood, T., Strawn, L. A., Wente, S. R. & Stewart, M. GLFG and FxFG nucleoporins bind to overlapping sites on importin-β. *J. Biol. Chem.* **277,** 50597–50606 (2002).

80. Pyhtila, B. & Rexach, M. A gradient of affinity for the karyopherin Kap95p along the yeast nuclear pore complex. *J. Biol. Chem.* **278,** 42699–42709 (2003).

81. Mammen, M., Choi, S. K. & Whitesides, G. M. Polyvalent interactions in biological systems: Implications for design and use of multivalent ligands and inhibitors. *Angew. Chemie - Int. Ed.* **37,** 2754–2794 (1998).

82. Wagner, R. S., Kapinos, L. E., Marshall, N. J., Stewart, M. & Lim, R. Y. H. Promiscuous Binding of Karyopherinβ1 Modulates FG Nucleoporin Barrier Function and Expedites NTF2 Transport Kinetics. *Biophys. J.* **108,** 918–927 (2015).

83. Chook, Y. M. & Süel, K. E. Nuclear import by karyopherin-βs: Recognition and inhibition. *Biochim. Biophys. Acta - Mol. Cell Res.* **1813,** 1593–1606 (2011).

84. Peters, R. Translocation through the nuclear pore: Kaps pave the way. *BioEssays* **31,** 466–477 (2009).

85. Paradise, A., Levin, M. K., Korza, G. & Carson, J. H. Significant Proportions of Nuclear Transport Proteins with Reduced Intracellular Mobilities Resolved by Fluorescence Correlation Spectroscopy. *J. Mol. Biol.* **365,** 50–65 (2007).

86. Riddick, G. & Macara, I. G. A systems analysis of importin-alpha-beta mediated nuclear protein import. *J. Cell Biol.* **168,** 1027–1038 (2005).

87. Grünwald, D., Singer, R. H. & Rout, M. Nuclear export dynamics of RNA-protein complexes. *Nature* **475,** 333–341 (2011).

88. Frey, S. & Görlich, D. A Saturated FG-Repeat Hydrogel Can Reproduce the Permeability Properties of Nuclear Pore Complexes. *Cell* **130,** 512–523 (2007).

89. Frey, S. & Gorlich, D. FG/FxFG as well as GLFG repeats form a selective permeability barrier with self-healing properties. *Embo J.* **28,** 2554–2567 (2009).

90. Patel, S. S., Belmont, B. J., Sante, J. M. & Rexach, M. F. Natively Unfolded Nucleoporins Gate Protein Diffusion across the Nuclear Pore Complex. *Cell* **129,** 83–96 (2007).

91. Patel, S. S. & Rexach, M. F. Discovering Novel Interactions at the Nuclear Pore Complex Using Bead Halo. *Mol. Cell. Proteomics* **7,** 121–131 (2008).

92. Ma, J., Goryaynov, A., Sarma, A. & Yang, W. Self-regulated viscous channel in the nuclear pore complex. *PNAS* **109,** 7326–7331 (2012).

93. Peters, R. Functionalization of a nanopore: The nuclear pore complex paradigm. *Biochimica et Biophysica Acta - Molecular Cell Research* **1793,** 1533–1539 (2009).

94. Adam, G. & Delbrueck, M. in *Structure Chemistry and Molecular Biology* (eds. Rich, A. & Davidson, N.) 198–215 (1968).

95. de Gennes, P. G. Polymers at an interface; a simplified view. *Advances in Colloid and Interface Science* **27,** 189–209 (1987).

96. Milner, S. T. Polymer brushes. *Science* **251,** 905–914 (1991).

97. Lim, R. Y. H. *et al.* Flexible phenylalanine-glycine nucleoporins as entropic barriers to nucleocytoplasmic transport. *Proc. Natl. Acad. Sci.* **103,** 9512–9517 (2006).

98. Chattopadhyay, K., Elson, E. L. & Frieden, C. The kinetics of conformational fluctuations in an unfolded protein measured by fluorescence methods. *Proc. Natl. Acad. Sci. U. S. A.* **102,** 2385–2389 (2005).

99. Schoch, R. L., Kapinos, L. E. & Lim, R. Y. H. Nuclear transport receptor binding avidity triggers a self-healing collapse transition in FG-nucleoporin molecular brushes. *Proc. Natl. Acad. Sci. U. S. A.* **109,** 16911–16916 (2012).

100. Schleicher, K. D. *et al.* Selective transport control on molecular velcro made from intrinsically disordered proteins. *Nat. Nanotechnol.* **9,** 525–530 (2014).

101. Zeitler, B. & Weis, K. The FG-repeat asymmetry of the nuclear pore complex is dispensable for bulk nucleocytoplasmic transport in vivo. *J. Cell Biol.* **167,** 583–590 (2004).

102. Jovanovic-Talisman, T. *et al.* Artificial nanopores that mimic the transport selectivity of the nuclear pore complex. *Nature* **457,** 1023–1027 (2009).

103. Tokunaga, M., Imamoto, N. & Sakata-Sogawa, K. Highly inclined thin illumination enables clear single-molecule imaging in cells. *Nat. Methods* **5,** 159–161 (2008).

104. Wagner, R. S., Kapinos, L. E., Marshall, N. J., Stewart, M. & Lim, R. Y. H. Promiscuous Binding of Karyopherinβ1 Modulates FG Nucleoporin Barrier Function and Expedites NTF2 Transport Kinetics. *Biophys. J.* **108,** 918–927 (2015).

105. Kowalczyk, S. W. *et al.* Single-molecule transport across an individual biomimetic nuclear pore complex. *Nat. Nanotechnol.* **6,** 433–438 (2011).

Chapter 2

Lipid Bilayers as Substrates for FG Nup Immobilization

2 Lipid Bilayers as Substrates for FG Nup Immobilization

2.1 Introduction

Intrinsically disordered proteins constitute about 30% of the eukaryotic proteome[1,2]. In contrast to structured proteins, IDP sequences combine a low mean hydrophobicity with an overall net charge leading to physiochemical properties reminiscent of random coils[3,4]. They act as versatile biological players involved in molecular recognition, catalysts of chemical reactions and protein fusions, alternative splicing etc. (*i.e.* activities complementary to those of structured proteins)[5–8]. While most of these processes rely on the extreme dynamic fluctuations of individual IDPs, several formidable biological challenges are governed by cooperative effects. Most prominent examples are the control of axonal caliber by steric exclusion of disordered neurofilaments[9], the inducement of lipid membrane curvature by disordered endocytic adaptors[10] or the collective non-monotonic conformational changes of the NPC selectivity barrier associated FG Nup domains[11] (see Section 1.2.3).

For the individual FG rich domains within the NPC, intrinsic disorder is a prerequisite, which permits rapid multivalent and multispecific interactions with Kaps[8,12] (see Section 1.2.2). Also, the steric pressure driven, brush-like ensemble conformation of pristine (depleted of Kaps) FG domain layers depends on random coil behavior and hence ultimately on intrinsic disorder of individual FG domains[13]. The observed molecular brush formation does thereby not preclude intra- and inter-FG domain cohesion, *e.g.* attractive hydrophobic F-F interaction may be present[14]. The strength of these bindings are still debated but are most likely very weak since they are transiently outcompeted ($K_D \approx 10^{-3}$ M) by NTRs[15–17] (which is true for all presented transport models in Section 1.2.3).

Several *in vitro* studies that motivate a NCT model of Kap-centric control (see "Kap-centric Model" in Section 1.2.3) were performed on covalently tethered FG domain brushes. Schoch *et al.* (2012)[18], Kapinos *et al.* (2014)[13] and Wagner *et al.* (2015)[19] constrained FG domains (from human Nup214, Nup98, Nup153, and Nup62 and its yeast ortholog Nsp1) to planar gold surfaces *via* covalent sulfide bonds, forming brush-like conformations with FG repeat densities reproducing the interior of a NPC. The kinetic and structural relationship of this FG domain brushes with physiological Kapβ1 concentrations was then assessed by means of a novel SPR based technique[20]. Schleicher *et al.* (2014)[21] on the other hand, utilized a silanization based surface chemistry to form Nup153 brushes *via* covalent N-terminal linkage to planar glass substrates and measured Kapβ1-facilitated, two-

dimensional cargo diffusion. Here, the envisaged goal is to test the proposed Kap-centric mechanism in glass nanocapillaries (GNCs; see Chapter 4) within a nanoscale, hourglass-shaped tip opening that resembles a native NPC scaffold. The silanization based approach previously used to functionalize planar glass surfaces was however not applicable for GNCs modification mainly due to sterical effects. Regardless, covalently end-grafted FG domain brushes are a suboptimal representation of the *in vivo* situation anyway. Hence, this demands for a new FG Nup immobilization strategy, which is equally applicable to the nanoconfined volumes of GNCs and, for the sake of comparability, to planar surfaces.

Anchoring of FG domains onto supported lipid bilayers (SLBs) formed *via* spontaneous liposome spreading[22–26] has proven to be the procedure of choice and shall be the scope of the present Chapter. In particular, histidine (His_6) tagged FG Nups domains are specifically conjugated to SLBs with varying fractions of metal ion chelator (NTA(Ni)) lipids (DGS)[27]. Depending on the level of crowding in the FG Nup layer on top of the SLB, the collective conformation of FG Nup domain ensembles undergoes a transition from the mushroom to the brush-like regime (similar to observation of covalently attached FG domains[13,18,19]). While the lipid fluidity of the underlying SLB is mainly preserved (*i.e.* mobile substrate), DGS NTA(Ni) lipids conjugated to His_6 FG Nup domains are stabilized by the intermolecular interaction within the FG Nup layer (*i.e.* "immobile brush"). These stabilized lipids act as obstacles to the mobility of other, non-stabilized lipid species within the SLB and hamper their lateral diffusion[28–30].

The dependence of the lateral diffusion of non-stabilized lipids on the attachment of FG Nup domains was examined by fluorescence recovery after photobleaching (FRAP) measurements of Rhodamine (Rh) labelled tracer lipids (PE; see Section 2.3). By using fluorescently labelled FG Nup domains, two-color FRAP experiments allow one to simultaneously monitor the recovery of Rh PE and DGS - FG Nups complexes (see Section 2.4). Comparing their diffusional behavior provides the means to investigate the influence of crowding effects on the mobility of individual domains within the FG Nup layer. Thereby, two different yeast nucleoporin Nsp1 fragments are used to study the influence of multivalent intermolecular interactions amongst individual disordered domains on their lateral diffusion: A disordered fragment from yeast Nsp1 with 1 FG and 11 FSFG repeats (Nsp1FF12) and the same fragment with all phenylalanine mutated to serine (Nsp1SS12). Inspecting their different diffusional behavior enables to address hindering

contribution of the hydrophobic F-F interactions directly, since all other parameters remain unchanged (see Section 2.5).

Finally, the functionality of lipid anchored yeast Nsp1FF12, yeast Nsp1SS12, human Nup153 and Nup98 FG domain brushes is scrutinized by comparing their binding kinetics with Kapβ1 to previous studies[13], where the same domains were covalently end-grafted. SPR measurements reveal that these FG Nup layers show similar kinetics, although the underlying SLB substrate remains fluid (see Section 2.6).

2.2 Theory and Background

2.2.1 Supported Lipid Bilayers from Liposomes

The creation of supported lipid bilayers by the spontaneous spreading of lipid vesicles (liposomes) on hydrophilic supports[31,32] is a three-step process: liposome adsorption, rupture and spreading (Figure 2.1)[24,33–35]. General parameters governing these three steps are the liposome composition, size, surface charge, surface roughness, solution pH, ionic strength, and osmotic pressure[36–38]. The adsorption from the bulk solution onto a glass substrate is mainly affected by electrostatic interactions and van der Waal forces between the liposome and the substrate, whereas the presence of divalent cations has been shown to promote the process (Figure 2.1A)[39]. Adsorbed liposomes are thought to deform until the gain in adhesion energy is balanced by the cost of bilayer bending[24], *i.e.* the interaction with the support induces stress in the liposome membrane. In the early stages, liposome-liposome fusion may take place as an intermediate step preceding rupture, which is probably not required for SLB formation on glass[35,36,38]. The rupture itself strongly depends on the above mentioned parameters, and the vesicles can spread upon contact with the support or not at all[26]. However, in the here presented cases (see below), rupture seems to be triggered by the density of adsorbed liposomes, *i.e.* the support-induced stress is enhanced by the hydrodynamic coupling of neighboring vesicles (Figure 2.1B)[37,40]. Once a critical density is reached, liposomes rupture and form islands of supported lipid bilayers. The resulting edges of these islands are energetically unfavorable as the hydrophobic hydrocarbon chains need to be screened from the aqueous solvent by a strong membrane curvature[41,42]. Hence, these edges provide the thermodynamic driving force which promotes the cascade-like spreading of the SLB islands[40]. Eventually, this propagation leads to full coverage (Figure 2.1C) whereas the quality of the bilayer depends strongly on the surface roughness and liposome size.

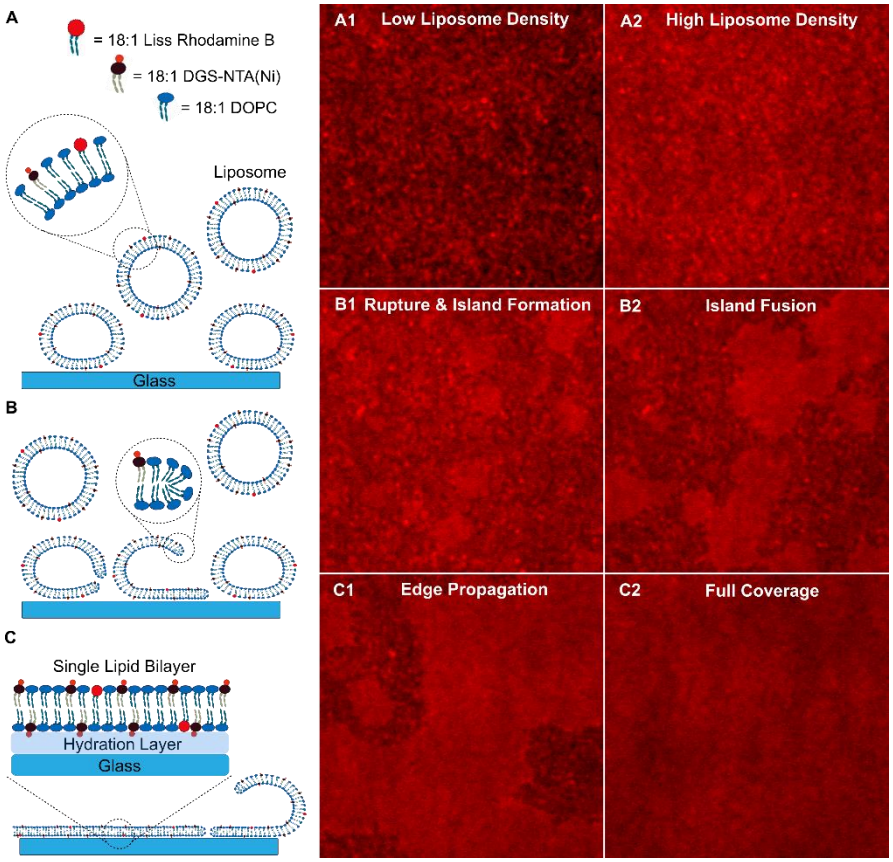

Figure 2.1: Supported lipid bilayer formation by spontaneous liposome spreading. **Left**: Schematics of the three formation steps. xz cross-sections of liposomes are shown. **Right**: TIRF images of the formation process. FOV is 20 µm x 20 µm. Total lipid concentration is 2 mM in PBS, thereof 20 %mol DGS NTA(Ni) and 0.1 %mol Rh PE. **A**, Liposomes (~30 nm) adsorb to a hydrophilized glass slide. Surface attached liposomes are thought to deform due to interactions with the glass support. **B**, Liposomes rupture once a critical density is reached. The resulting islands possess energetically unfavorable edges. **C**, The edges drive the spreading of the islands by fusing with neighboring islands, surface-attached liposomes and freely diffusing liposomes. Eventually, edge propagation leads to full coverage with an intact supported lipid bilayer.

2.2.2 Fluorescence Recovery after Photobleaching

Fluorescence recovery after photobleaching (FRAP) was chosen from the various fluorescence techniques[43] available to determine diffusion and binding kinetics of lipids and proteins in and on SLBs for three reasons. First, FRAP is the experimentally simplest amongst the techniques (compared to FCS or single molecule tracking). Second, it is more robust in the presence of immobile species[44] and third, it is compatible with a fluorophore concentration used for ordinary imaging[45]. A representative FRAP experiment of fully recovering two-dimensional Rh PE tracer diffusion is depicted in Figure 2.2. After recording the fluorescence intensity (FI_0) in a given region of interest (ROI = 15 µm^2), the fluorophores in that ROI are bleached (bleaching depth of 40 %, $FI_{bleach} = 0.6\ FI_0$) by a short high power laser exposure (50 ms). Over time, bleached Rh PE tracers are replaced by non-

bleached tracers, which laterally diffuse through the ROI. This purely diffusive, isotropic and unhindered (all tracers Rh PE undergo Brownian motion) motion recovers the fluorescence intensity in the ROI ($FI(t)$), eventually up to the initial value ($FI_0 = FI_\infty$), *i.e.* no immobile fraction is present.

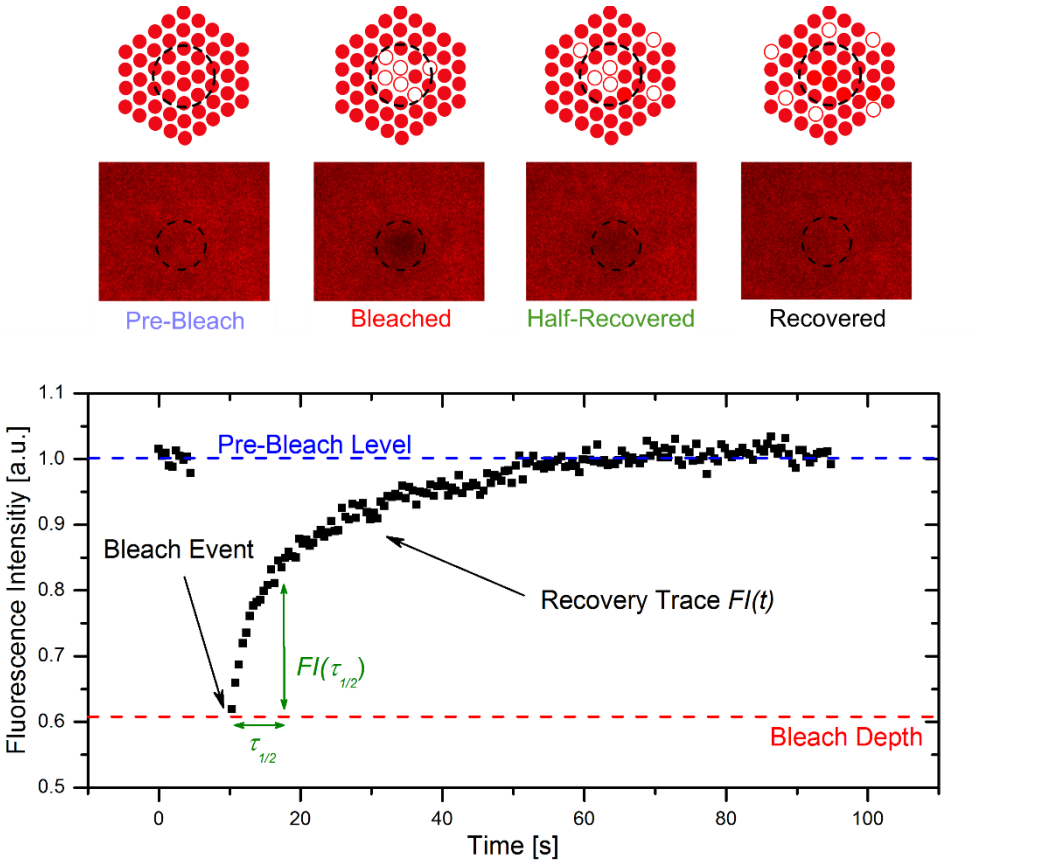

Figure 2.2: Principle of fluorescence recovery after photobleaching (FRAP). The fluorescence recovery (trace and images) of 0.1 %mol Rh PE tracers within an SLB (DOPC) is shown. The dashed circle in the images corresponds to a ROI of 15 µm², the dashed circle in the schematics is purely descriptive. Schematics are not true scale. The measurement starts with the acquisition of a pre-bleach value, *i.e.* the average fluorescence signal in a given ROI (usually 10 – 100 µm²). The fluorophores in the ROI are then bleached by exposing them to a high power laser beam (bleach depth usually 30 – 80 % of the initial value, exposure time should be << $\tau_{1/2}$). Subsequently, the fluorescence signal in the ROI starts to recover either by pure in-diffusion of non-bleached fluorophores (as it is the case here), exchange of bleached and non-bleached species at a binding site or the combination of the two. Note: Concentration within the ROI does not change during a FRAP experiment under the assumption that reactions are at equilibrium and that diffusion is flow free.

The time dependent fluorescence recovery in the ROI ($FI(t)$) after bleaching for the two dimensional case can be described as

$$FI(t) = \frac{\alpha P}{\pi r^2} \iint_0^r C(x,y,t)\, dx\, dy \quad (2.1)$$

with *C(x,y,t)* the evolution of fluorophore concentration within the ROI, *P* the laser intensity (where *P = 0* outside the ROI) and *α* a constant which incorporates all the quantum yields (absorption, emission and detection) and laser power attenuation[46]. In general, diffusion dominant recovery is however not the only possible mechanism. *C(x,y,t)* is determined by the underlying physics and needs to be derived from the consideration of the actual problem.

Several analytical and numerical solutions for the description of FRAP recovery curves acquired in various experimental settings have been reported[47]. Here, the two simplest cases shall be introduced: the above mentioned limit of pure diffusion and the limit of binding reaction dominated recovery. Three required assumptions to do so are that bleaching of the fluorophore to a non-fluorescent species is a simple irreversible first-order reaction, that the bleaching time is much shorter than half time of recovery ($\tau_{1/2}$) and that the bleaching region is circular[48].

1. Diffusion-limited recovery

If no or little binding is occurring, *i.e.* most fluorophores are free ($k_{on} / k_{off} << 1$), only diffusion needs to be considered. For the case of isotropic and uniform diffusion, the problem reduces to the second Fickian law

$$\frac{\partial C}{\partial t} = D\nabla^2 C \quad (2.2)$$

and an analytical solution was given by Soumpasis (1983)[46]

$$FI(t) = FI_\infty e^{-\frac{\tau_{1/2}}{2t}}\left(I_0\left(\frac{\tau_{1/2}}{2t}\right) + I_1\left(\frac{\tau_{1/2}}{2t}\right)\right) \quad (2.3)$$

where I_0 and I_1 are modified Bessel functions and FI_∞ is the maximal recovered fluorescence intensity for $t \rightarrow \infty$.

2. Reaction-limited recovery

The situation is particularly simple in the case where recovery is not limited by diffusion but by the availability of binding sites within the ROI ($r^2 / D << k_{off}^{-1}$). The problem can be stated as

$$\frac{\partial C}{\partial t} = -k_{off}\, C \quad (2.4)$$

and it has been shown analytically by Bulinski *et al.* (2001)[49] that k_{off} is identical with the rate constant of the fluorescence recovery

$$FI(t) = FI_{\infty} - FI_{\infty}\, e^{-k_{off}*t} \quad (2.5)$$

Mention of other situations (*e.g.* full models incorporating the combination of diffusion and binding reactions with immobile[50] or mobile binding sites[51]) shall be omitted, because it turned out that the two limits suffice to describe the here presented data adequately. However, interested readers are referred to a comprehensive review by Loren *et al.* (2015)[47].

The half time of recovery $\tau_{1/2}$ (see Figure 2.2) can be interpreted as characteristic lateral diffusion time and relates to a phenomenological diffusion constant by

$$D = 0.224\, \frac{r^2}{\tau_{1/2}} \quad (2.6)$$

with *r* the radius of a circular ROI (the bleached area)[48]. By numerically solving for $\tau_{1/2}$, Equation (2.6) allows one to compare different FRAP experiments to each other regardless of the underlying physics of fluorescence recovery.

2.2.3 Effect of Obstacle on the Lipid Diffusion

The phenomenological diffusion constant *D* can be related to the microscopic properties of the diffusing Rh PE tracer in the SLB. The diffusion of a fluorescent species (Rh PE) similar in size to the lipid mainly constituting the SLB (DOPC) is usually treated using the free area theory[52]. All lipids in the SLB are assumed to perform a thermally driven Brownian motion. For each step of this two dimensional random walk, a lipid requires sufficient free area to move. To perform such a step (or jump) however it has to overcome a certain activation energy E_a [ref. 44]. This activation energy depends on frictional coupling of the lipid with other lipid molecules, with the aqueous bulk solution and with the solid surface[29,52]. The tracer diffusion in dependence of the average free area in the membrane $a_f = a_t - a^*$ (where a_t is the total average area per lipid and a^* the closed packed disc area) is given by

$$D_{tracer} = D_0\, e^{-(\frac{\vartheta a^*}{a_f} + \frac{E_a}{kT})} \quad (2.7)$$

with ϑ a correction factor for overlapping free areas and *k* the Boltzmann constant. Note: The diffusion within the free area D_0 is constant and the overall phenomenological diffusion constant depends only on the probability distribution of free areas in the system and the Boltzmann distribution of the activation energy.

When the lateral lipid diffusion is hindered by obstacles, a modified free-area model applies. The degree of hindrance is thereby given by the obstacle area fraction, which is equal to the concentration *c* of DGS NTA(Ni)), (assuming similar head group areas $A_{DOPC} \approx A_{DGS\ NTA(Ni)} \approx A_{Rh\ PE}$), such that $D_{tracer} \rightarrow D_{tracer}(c)$. For a given concentration *c* and a normalized tracer diffusion constant $D^*_{tracer}(c) = D_{tracer}(c) / D_{tracer}(0)$ this model follows a second order dependence and simply writes[29,53]

$$D^*_{tracer}(c) = 1 + ac + bc^2 \quad (2.8)$$

Depending on the values of the coefficients *a* and *b,* the repulsion by the obstacles is best described by a hard-core or a soft-core model (see Appendix Chapter 2). The latter accounts for an increase of the scattering cross-section by a soft-shell around the obstacle radius *R*, *i.e.* the presence of an annular region of partially ordered lipids with a characteristic coherence length ξ [ref. 53].

Depicting the lipid layer as a close packed honeycomb lattice allows one to interpret the two dimensional diffusion as random jumps between adjacent lattice sites[28]. The jump rate of Rh PE ($j_{tracers}$) is proportional to the measured diffusion constants $D_{tracers}$. Accordingly, assuming the obstacles are mobile as well, the jump rate of the DGS NTA(Ni) (j_{obs}) corresponds to the overall diffusion constant, D_{obs} [ref. 28]. The jump rate ratio can hence be defined as the ratio of the jump rate of tracers to the jump rate of obstacles at very low $c \approx 0$, $\gamma = j_{tracers} / j_{obs} = D_{tracers}(c \approx 0) / D_{obs}(c \approx 0)$.

Since the obstacles are now mobile, diffusion of tracers is a function of γ as well ($D_{tracer}(c) \rightarrow D_{tracer}(c, \gamma)$) and the normalized hindered diffusion is described by the relative Rh PE diffusion constant $D^*_{tracer}(c, \gamma) = D_{tracer}(c, \gamma) / D_{tracer}(0, \infty)$. The analytical expression for $D^*_{tracer}(c, \gamma)$ by means of a hard-core assumption with mobile obstacles is[28,54–56]

$$D^*_{tracer}(c, \gamma) = (1 - c) * f(c, \gamma) \quad (2.9)$$

where $f(c, \gamma)$ is a correlation factor depending on the jump rate ratio and the obstacle concentration:

$$f(c,\gamma) = \frac{\sqrt{\{[(1-\gamma)(1-c)*f_0+c]^2+4*\gamma*(1-c)*f_0^2\}}-[(1-\gamma)(1-c)*f_0+c]}{2*\gamma*(1-c)*f_0} \quad (2.10)$$

and $f_0 = 1 / (2 + (2 * \gamma - 1))$ for a honeycomb lattice. Consequently, fitting Equation (2.9) to $D^*_{tracer}(c)$ with γ as free fitting parameter allows one to determine diffusion constant of the obstacles, $D_{obs}(c = 0)$.

For the situation, where fluorescently labelled, His_6-tagged FG domains are attached to the DGS NTA(Ni) lipids to form DGS - FG Nup complexes, D_{obs} is directly addressable *via* FRAP. Here, it is hypothesized that upon complex formation the long-range diffusion of DGS NTA(Ni) within the SLB depends on the crowding of FG domains on top. The crowding itself however is mainly determined by the available binding site density, which is in turn just the number of DGS NTA(Ni) per area of SLB. The obstacle diffusion D_{obs} therefore becomes dependent on the DGS NTA(Ni) concentration, *i.e.* $D_{obs} \rightarrow D_{obs}(c)$ and $\gamma \rightarrow \gamma(c) = D_{tracers}(c) / D_{obs}(c)$. Inserting Equation (2.10) into Equation (2.9) and resolving for c allows one to calculate the concentration of obstacles that are effectively involved in complex formation for every measured pair of $D_{tracers}(c)$ and $D_{obs}(c)$

$$c_{eff} = \frac{1-\gamma(c)*D^*_{tracers}(c,\gamma)^2-(1-\gamma(c))*D^*_{tracers}(c,\gamma)}{3*\gamma(c)*D^*_{tracers}(c,\gamma)+\frac{1}{1+2*\gamma(c)}} \quad (2.11)$$

Assuming that the different lipid species have a similar head group area ($A_{DOPC} \approx A_{DGS\ NTA(Ni)} \approx A_{Rh\ PE}$), the grafting distance g between individual FG domains scales simply with $c_{eff}^{-1/2}$, $g = c_{eff}^{-1/2}$. For high enough c_{eff}, adjacent FG domains overlap, *i.e.* the grafting distance is in the range or smaller than the hydrodynamic radius r_{hyd} of the attached domain, $g \leq r_{hyd}$. $D_{obs}(g)$ is then not only influenced by viscous drag of domains on top of the SLB and their collisions, but also by additional molecular interactions.

According to the Flory theory, this FG domain-overlap results in an increased excluded volume interaction F_{ev}, such that the domains start stretching away from the lipid layer. Under the assumption that a constant number of monomers distributes uniformly within the FG layer (*i.e.* mean field approximation) and that

the FG domains are random coils (*i.e.* Gaussian model), the free energy contribution of the excluded volume per unit area is given by[57–59]

$$F_{ev} = \frac{kTh}{V_0}(1-\varphi)\ln(1-\varphi) \quad (2.12)$$

where V_0 is the monomer volume, h the height of the FG Nup layer and φ the volume fraction. Possible attractive intermolecular interactions (*e.g.* hydrophobic F-F interactions) might add another energy contribution[14]

$$F_\chi = \frac{kTh}{V_0}\left(\frac{\chi\varphi^2}{2}\right) \quad (2.13)$$

with χ an interaction parameter (attractive interaction for $\chi < 0$).

Here, a free area model (see Equation 2.7) is hypothesized for the diffusion of FG domains on top of the SLB. In such a scenario, possible intermolecular interactions manifest themselves as the activation energy E_a, which individual DGS – FG Nup complexes have to overcome to explore free area. The excluded volume interaction is then replaced by a free area dependency, simply approximated by the ratio $(\vartheta r_{hyd}^2)/(g^2 - r_{hyd}^2)$, with ϑ the correction factor for overlapping free areas. The lateral diffusion constant for DGS – FG Nup in dependence of the grafting distance then writes

$$D_{obs}(g) = D_{obs}(c \approx 0)e^{-\left(\frac{\vartheta r_{hyd}^2}{g^2 - r_{hyd}^2} + \frac{E_a}{kT}\right)} = D_{obs}(c \approx 0)e^{-\left(\frac{\vartheta r_{hyd}^2}{g^2 - r_{hyd}^2} + \left|\frac{F_\chi}{kt}\right|\right)} \quad (2.14)$$

where $D_{obs}(c \approx 0) = D_{obs}(g \to \infty)$. Replacing the volume fraction and the layer height in Equations (2.13) by (see Appendix Chapter 2)

$$\varphi = \frac{g^{((\nu^{-1})-3)}}{V_0 b^{\nu^{-1}}} \text{ and } h = \frac{N b^{\nu^{-1}}}{g^{(\nu^{-1})-1}} \quad (2.15)$$

leads to

$$\frac{F_\chi}{kt} = \frac{\chi N g^{(\nu^{-1}-5)}}{2{V_0}^3 b^{\nu^{-1}}} \quad (2.16)$$

where N the number of monomers with Kuhn length b and ν the Flory parameter ($\nu = 1/3$ for a poor solvent and $\nu = 3/5$ for a good solvent).

2.3 Diffusion Behavior without FG Domain Attachment

Highly monodisperse liposome solutions (PDI < 0.1) were used to spontaneously form single lipid bilayers of different compositions on glass supports (see Figure 2.1 and Figure 2.3A). Independent of the DGS – NTA(Ni) concentration, Rh PE recovery curves fit to a modified, one-component exponential decay (Equation 2.3)[46]. Equation (2.3) describes purely diffusive, isotropic recovery processes[50], and the high goodness of fit (Adj. $R^2 > 0.925$, see Table 2.1) hence implies a purely diffusive Rh PE recovery for all tested lipid compositions. Besides, the adequate description of the recovery curves by a simple one-component decay is either indicative for partitioning of the tracers into one leaflet[60] or for an identical half time of recovery $\tau_{1/2}$ in both leaflets of the SLB. The fact that SLBs were formed by liposome spreading (see Section 2.2.1) points towards strong hydrodynamic coupling between the glass support and the proximal leaflet. Hydrodynamic effects could hence govern the overall recovery behavior *via* strong transmembrane interactions, *i.e.* the inter-leaflet diffusional coupling leads to a levelling of the Rh PE tracer diffusion throughout the SLB[61].

However, this scenario is discarded by the strong 2nd order dependence of the normalized Rh PE diffusion constant $D^*_{tracer}(c)$ on the DGS NTA(Ni) concentration c (Figure 2.3C). Depending on c, the lateral normalized diffusion constant is reduced up to 60 % compared to SLBs composed only by DOPC (99.9 %mol) and Rh PE (0.1 %mol). Changes of this magnitude induced by stronger hydrodynamic coupling due to increasing fractions of DGS NTA(Ni) presume strong electrostatic interaction between the glass substrate and the NTA(Ni) enriched SLB and a substantial and coordinated rearrangement of water molecules at the interface of the proximal leaflet and the hydration layer. Although NTA(Ni) complexes might potentially influence the adjacent solvent coordination, significant electroviscous contribution to the drag within the hydration layer is ruled out by the ionic strength in the saline saturated measurement buffer (150 mM NaCl).

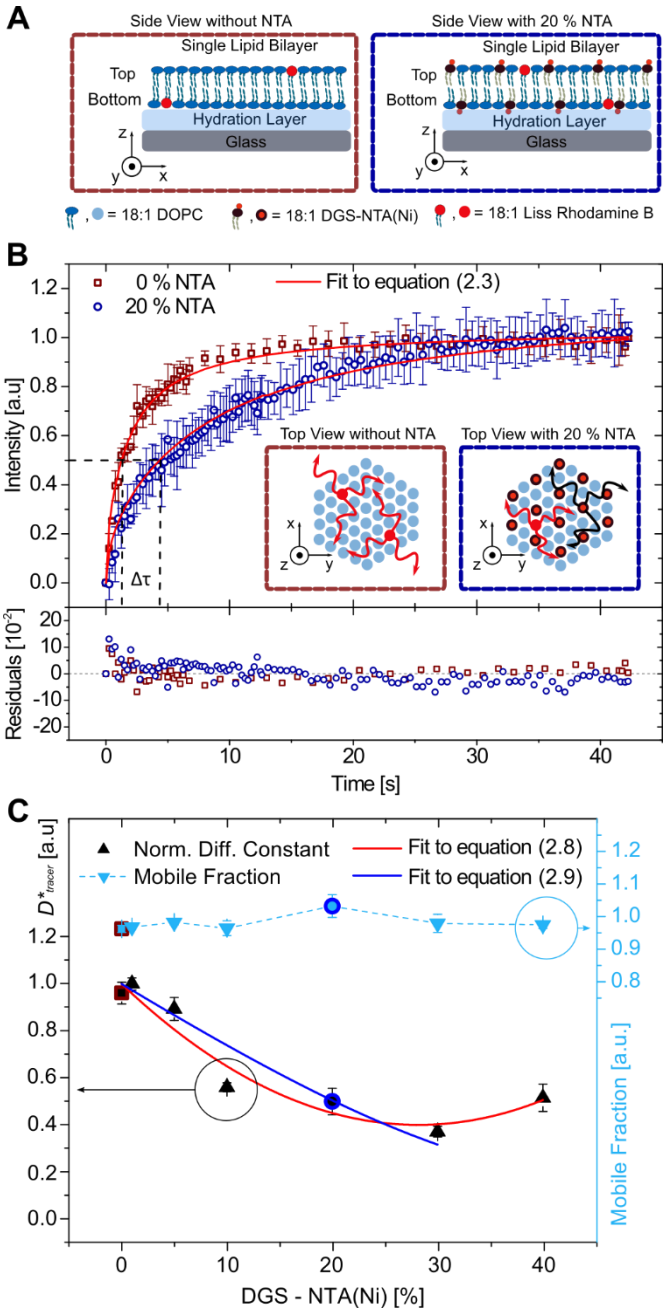

Figure 2.3: Lipid diffusion within supported lipid bilayers. **A**, Schematics of xz cross-sections of SLBs without and with 20 % DGS NTA(Ni) lipids. Schematics are not drawn to scale. The thickness of the hydration layer is ~1 nm [ref. [62]], the thickness of the SLB ~8 nm. **B**, Representative full-scale normalized FRAP curves for Rh PE recovery ($n_{0\%}$ = 5 and $n_{20\%}$ = 5). Curves for all lipid compositions are fitted with the purely diffusion limited solution Equation 2.3. The inset schematics depict the top view on an assumed hexagonal close-packed lattice. Schematics are not drawn to scale**. C**, Normalized Rh PE diffusion decreases with increasing fraction of DGS NTA(Ni). A modified free area model (red; Equation 2.8) is fitted to the entire range and leads to an unphysical minimum at ~30%. This motivates the omission of the data obtained at 40% DGS NTA(Ni) and fitting of the reduced range 0-30% with a hard-core model including mobile obstacles (blue; Equation 2.9). Rh PE recovers fully for all given lipid compositions. The bigger data points at 0% and 20 % DGS NTA(Ni) are colored according to the respective FRAP curves in (**B**) and schematics in (**A**).

Hence, there is strong evidence, that the DGS NTA(Ni) obstructs the Rh PE mobility on the length scale of the employed ROI. The degree of hindrance is thereby given by the obstacle area fraction equal to the DGS NTA(Ni) concentration c (assuming that the different lipids have a comparable head group area, $A_{DOPC} \approx A_{DGS\ NTA(Ni)} \approx A_{Rh\ PE}$). Applying the modified free-area model for obstructed diffusion (Equation 2.8)[29,53] allows one to determine whether the repulsion by DGS NTA(Ni) is best described by a hard-core or a soft-core model. Here, we find a = -4.26 and b = 7.56 (with 95% confidence bounds of ± 1.24 and ± 3.61 respectively) with an adj. R^2 = 0.991, leading to a ratio R/ξ = 1.24 ± 0.15 (see Appendix Chapter 2). Thus, interactions between Rh PE and DGS NTA(Ni) lack a soft repulsive component, implying that DGS NTA(Ni) does not induce order into surrounding DOPC. The curve for $D^*_{tracer}(c)$ reaches a minimum with no physical meaning for $c \approx 30\%$. The minimum simply indicates that the approximations of the modified free-area model and therefore the hard-core interpretation does not hold for $c > 30\%$.

Table 2.1: Rh PE diffusion dependence on unbound DGS NTA(Ni) content. Diffusion is calculated by means of Equation (2.6) from $\tau_{1/2}$. Mobile fraction, half time and adjusted R^2 were obtained from fits to Equation (2.3)

%NTA	Diffusion [µm²s⁻¹]	Mobile Fraction	Adjusted R²	N / n
0	0.665 ± 0.032	0.964 ± 0.011	0.969 ± 0.004	3 / 13
1	0.692 ± 0.018	0.970 ± 0.004	0.972 ± 0.002	4 / 18
5	0.618 ± 0.034	0.984 ± 0.008	0.970 ± 0.005	4 / 15
10	0.387 ± 0.013	0.966 ± 0.023	0.975 ± 0.003	3 / 16
20	0.345 ± 0.039	1.034 ± 0.035	0.952 ± 0.006	4 / 21
30	0.256 ± 0.016	0.981 ± 0.028	0.955 ± 0.004	4 / 21
40	0.356 ± 0.040	0.976 ± 0.011	0.925 ± 0.007	4 / 20

While D_{tracer} depends on the DGS NTA(Ni) concentration for the range of 0 – 40 %, the mobile fraction mf_{tracer} of the Rh PE tracers does not (Figure 2.3c, Table 2.1). By means of a full scale double normalization (where FI_0 = 1 and the first post-bleach value FI_p = 0) mf_{tracer} is equal to the maximal recovered fluorescence intensity FI_∞, $mf = FI_\infty / FI_0 = FI_\infty \in [0, 1]$. The full fluorescence recovery for Rh PE tracers ($mf_{tracer} \approx 1$) then suggests that the different lipid compositions form a single phase and that DGS NTA(Ni) are mobile (otherwise the percolation limit where $D^*_{tracer} \rightarrow 0$ and $mf_{tracer} \rightarrow 0$ would be at c = 41%)[28,29].

Taken together, the above results justify an analysis by means of a hard-core model with mobile obstacles[28,54–56] for a DGS NTA(Ni) concentration $c \leq 30$ %. Fitting equation (2.9) to $D^*_{tracer}(c)$ with γ as free fitting parameter then allows one to determine $D_{obs}(0)$. Describing the lipid layer as a close packed honeycomb lattice (Figure 2.3b) and assuming a lipid head area of 0.71 nm², we obtain γ = 4.35

(with 95% confidence bounds of ± 7.54) with an adj. R^2 = 0.906. This means that on average DGS NTA(Ni) diffuses ~4 times slower than the Rh PE tracers.

2.4 Diffusion Behavior with FG Domain Attachment

DGS NTA(Ni) containing lipid bilayers served as substrates for the immobilization of various disordered FG domains. For example, His_6-tagged Nsp1FF12 was anchored specifically to the NTA(Ni) modified lipid heads in the top leaflet (Figure 2.4A). Covalently attached Alexa488 labels near the His_6 tags allow one to determine the diffusion constants of these DGS NTA(Ni) – Nsp1FF12 Alexa488 complexes (hereafter DGS – Nsp1FF12) and Rh PE tracers *via* simultaneous two-color FRAP experiments. Representative recovery curve averages for a DGS NTA(Ni) content of 10% (Figure 2.4B; $n_{DGS - Nsp1FF12}$ = 4, $n_{Rh\ PE}$ = 4) emphasize the major differences in the recovery behavior. Rh PE recovers fully and ~10 times faster than the DGS – Nsp1, which saturate at ~60 % of the pre-bleached intensity (see Table 2.2). While Rh PE still recovers according to Equation (2.3) regardless of the Nsp1FF12 on top of the SLB, DGS – Nsp1FF12 curves are more accurately characterized by Equation (2.5) which describes a reaction dominated process[50], *i.e.* interactions between the Nsp1FF12 domains rather than pure diffusion determines their fluorescence recovery. As for Equation (2.3), the maximal recovered fluorescence intensity FI_∞ is interchangeable with the mobile fraction mf_{obs} of DGS – Nsp1FF12 under full scale normalization. The mobile fraction of reaction-dominated recovery can also be interpreted as the dynamic equilibrium concentration of bound Nsp1FF12 domains. For the presented case of 10% DGS NTA(Ni), a fraction of 40% remains in an immobile bound form. Note: The temporal resolution is kept constant while measuring recovery, which leads to an overweighting of the slower phase in the fitting process. To alleviate this bias, the transition point from fast to slow phase is defined as the asymptotic crossover point (half of the slope is used for the fast phase asymptote) and the number of points on both sides equalized (Figure 2.4B; see Appendix Chapter 2)

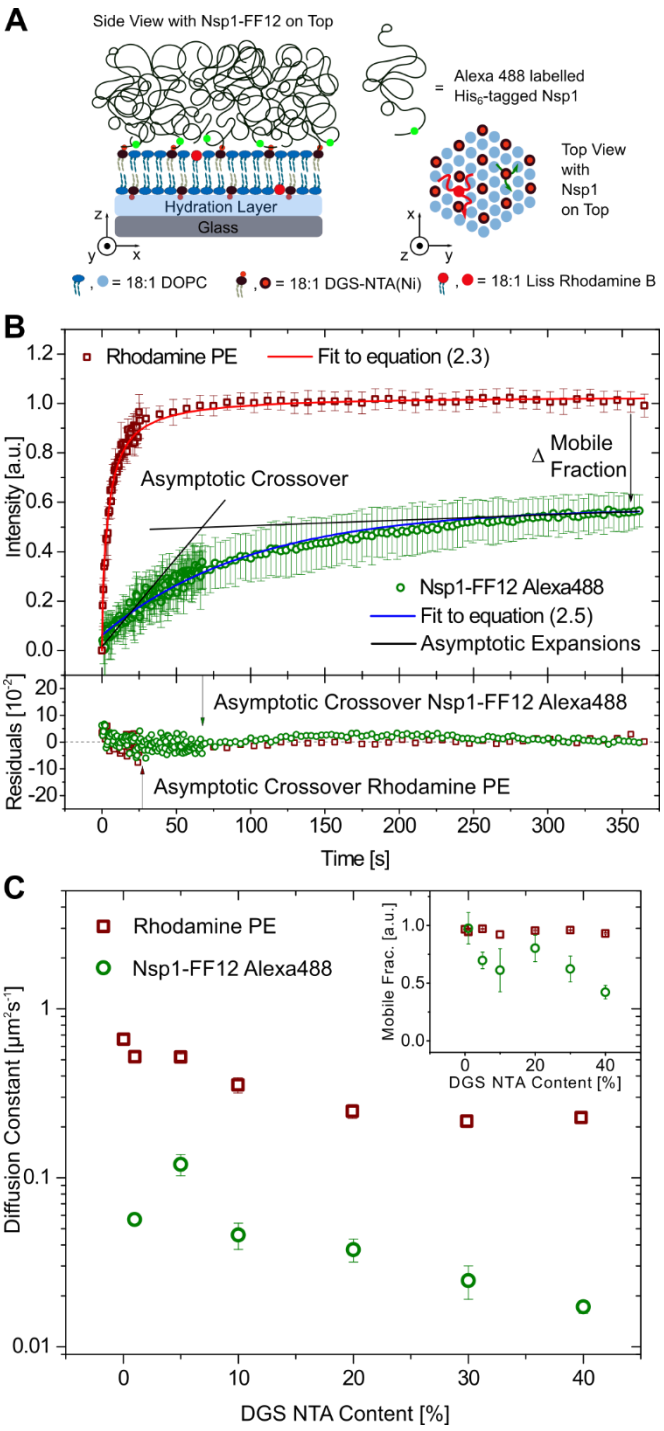

Figure 2.4: Supported lipid bilayers as substrate for FG Nup immobilization. **A**, Schematics of xz cross-section and xy top view of SLBs with Alexa488 labelled Nsp1FF12 attached. Schematics are not drawn to scale. **B**, Representative full-scale normalized FRAP curves for the recovery of DGS - Nsp1FF12 and Rh PE ($n_{DGS-Nsp1}$ = 4, $n_{Rh\ PE}$ = 4) at a concentration of 10% DGS NTA(Ni). The asymptotic crossover point is defined to compensate for the over-weighted slow phase during fitting (see main text and Appendix Chapter 2). **C**, Comparison of simultaneously measured D_{tracer} and D_{obs} over a range of 0% – 40% DGS NTA (Table 2.2 and 2.3). Inset: As for the case where no FG domains are attached, Rh PE recovers fully for all given lipid compositions. In contrast, the mobile fraction of Nsp1FF12 decays with increasing concentration of DGS NTA(Ni).

As expected from the notion, that FG domains crowd on top of the SLB (Figure 2.4A), diffusion of DGS – Nsp1FF12 drops with increasing DGS NTA(Ni) content *c* (Figure 2.4C). The diffusion at the highest measured *c* ($D_{obs}(c = 40\%)$) compared to the diffusion at lowest measured *c* ($D_{obs}(c = 1\%)$) is ∼3 times slower (seeTable 2.2). The jump rate ratio changes from ∼4 for 0% DGS NTA(Ni) (see Section 2.3) to ∼13 for a DGS NTA(Ni) content of 40 % (see Table 2.3). Strikingly, the mobile fraction mf_{obs} of the DGS – Nsp1 FF12 complexes decreases from ∼1 (c = 1%) to ∼0.4 (c = 40%), while the Rh PE tracers recover fully ($mf_{tracer} \approx 1$) for all given compositions (Figure 2.4C inset). In other words, while the lipid fluidity of the underlying SLB is preserved, DGS – Nsp1FF12 is stabilized by the Nsp1FF12 interactions within the FG domain layer.

The fact that the recovery of DGS – Nsp1FF12 is reaction dominated for all lipid compositions (adj. $R^2 > 0.92$) is suggestive for a process were Nsp1FF12 forms transient aggregates. The occurrence of those depends on the level of crowding, *i.e.* the probability of formation of such short-lived intermolecular complexes increases with the availability of Nsp1FF12 domains. DGS lipids bound to individual domains involved in aggregates are immobilized for the time the domain remains associated. As the aggregates dissipate, DGS – Nsp1FF12 is free to diffuse again and eventually form new aggregates. This interpretation is backed by the significant reduction of the mobile fraction for increasing *c* (*e.g.* mf_{obs} (c = 40%) ≈ 0.4). The higher the DGS – Nsp1FF12 density, the higher the probability of domain-domain encounters and the average number of FG motifs involved in intermolecular interaction per domain.

The average grafting distance between Nsp1FF12 domains is given by the areal density of possible anchoring points. This density is hence equal to the concentration of DGS NTA(Ni), *c*. Assuming again, that the different lipid species have a similar head group area ($A_{DOPC} \approx A_{DGS\ NTA(Ni)} \approx A_{Rh\ PE}$), the average grafting distance scales with $c^{-1/2}$. However, the efficiency of DGS NTA(Ni) ε needs to be considered such that the effective grafting distance scaling becomes $(\varepsilon c)^{-1/2} = c_{eff}^{-1/2}$. Equation (2.11) is applied to deduce c_{eff} from the two measured diffusion constants $D_{tracer}(c)$ and $D_{obs}(c)$. The obtained c_{eff} are normalized by $c_{eff}(c = 1\%)$ and compared to the normalized fluorescence intensity of Nsp1FF12 Alexa488 ($FI_{488}(c)$ / $FI_{488}(c = 1\%)$) prior to bleaching. The overlap of the normalized $c_{eff}(c)$ which is solely derived from diffusional dependencies *via* Equation (2.11) and the normalized $FI_{488}(c)$ which is purely based on fluorescence observations is remarkable (Figure 2.5 top). Note: Quantitative interpretation of fluorescence

signals is only meaningful if they are derived from relations, *i.e.* related to calibration beads etc. Here, FI_{488} (c = 1%) is used under the assumption that ε(c = 1%) = 1. FI_{488} (c = 10%) is not considered because it was not acquired within the same measurement series.

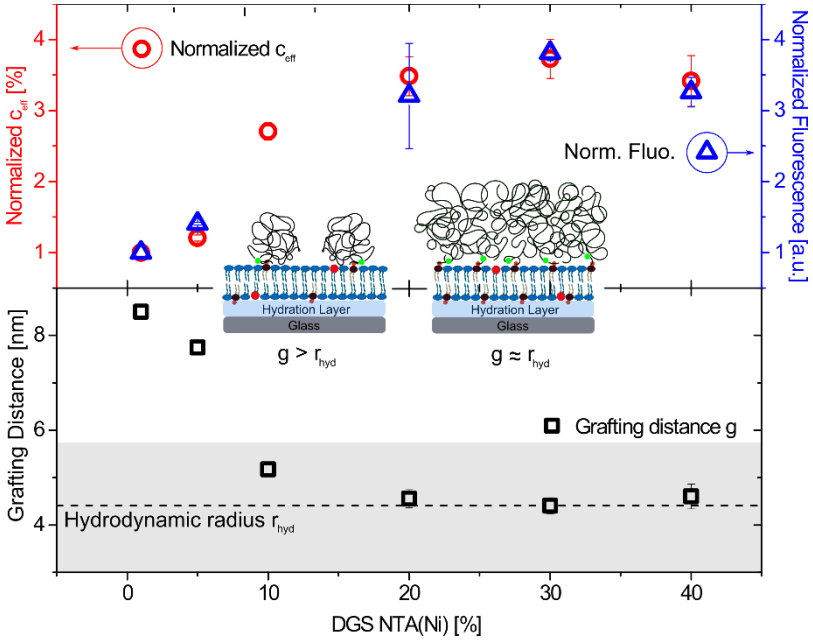

Figure 2.5: Dependence of the Nsp1FF12 grafting distance on DGS NTA(Ni) content. **Top,** Comparison of the normalized effective concentration c_{eff} (left) calculated from the two measured diffusion constants $D_{tracer}(c)$ and $D_{obs}(c)$ and the normalized pre-bleached fluorescence signals (right) of Nsp1FF12 Alexa488. Circled symbols are axis indicators. **Bottom,** Grafting distance g as obtained from conversion of the effective DGS – Nsp1FF12 concentration. Dashed line indicates the hydrodynamic radius of Nsp1FF12 as measured in PBS solution with DLS, $r_{hyd} \approx 4.3 \pm 1.4$ nm.

The average grafting distance g is obtained from the conversion of c_{eff} (Figure 2.5 bottom). Interestingly, g saturates around the hydrodynamic radius $r_{hyd} \approx 4.3 \pm 1.4$ nm of Nsp1FF12. The overall conformation of the Nsp1FF12 domains on top of the SLB hence enters a brush-like regime ($g \leq r_{hyd}$) for $c \geq 20\%$.

Table 2.2: DGS – Nsp1 FF12 diffusion dependence on DGS NTA(Ni). Diffusion is calculated from $\tau_{1/2}$ by means of Equation (2.6). Mobile fraction, half time and adjusted R^2 were obtained from fits to Equation (2.5).

%NTA	Diffusion [µm^{2}s^{-1}]	Mobile Fraction	Adjusted R^2	N / n
1	0.043 ± 0.007	0.975 ± 0.135	0.952 ± 0.009	1 / 5
5	0.119 ± 0.016	0.695 ± 0.071	0.945 ± 0.012	2 / 10
10	0.030 ± 0.005	0.611 ± 0.186	0.924 ± 0.032	2 / 8
20	0.027 ± 0.003	0.801 ± 0.115	0.959 ± 0.012	2 / 8
30	0.020 ± 0.005	0.623 ± 0.112	0.930 ± 0.012	2 / 11
40	0.016 ± 0.002	0.421 ± 0.058	0.861 ± 0.015	1 / 5

Table 2.3: Rh PE Diffusion Dependence of DGS NTA(Ni) Content After Nsp1 FF12 Incubation. Diffusion is calculated from $\tau_{1/2}$ by means of Equation (2.6). Mobile fraction, half time and adjusted R^2 were obtained from fits to Equation (2.3).

%NTA	Diffusion [$\mu m^2 s^{-1}$]	Mobile Fraction	Adjusted R^2	N / n
0	0.628 ± 0.034	0.978 ± 0.005	0.965 ± 0.004	2 / 10
1	0.495 ± 0.027	1.013 ± 0.011	0.944 ± 0.015	2 / 10
5	0.491 ± 0.019	0.999 ± 0.010	0.970 ± 0.003	2 / 10
10	0.298 ± 0.032	1.023 ± 0.012	0.946 ± 0.011	2 / 4
20	0.234 ± 0.022	1.038 ± 0.014	0.955 ± 0.006	2 / 8
30	0.204 ± 0.016	1.005 ± 0.009	0.959 ± 0.003	2 / 9
40	0.214 ± 0.011	1.020 ± 0.009	0.930 ± 0.006	2 / 11

2.5 The Influence of Hydrophobic F-F Interactions

Inspired by recent work of Vovk *et al.* (2016)[14], a de Gennes – Alexander polymer brush model based approach is applied (Equations 2.12 through 2.16) to inspect the effect of attractive interactions on the diffusional behavior of DGS NTA – Nsp1FF12 Alexa488 (see Appendix Chapter 2). To do so, His_6-tagged Nsp1SS12 - a variant of Nsp1FF12 where all the Phenylalanine (F) are replaced by Serine (S) - was used to form DGS NTA – Nsp1SS12 Alexa488 complexes (hereafter DGS – Nsp1SS12). This allows one to directly scrutinize the contribution of F-F interactions to $D_{obs}(g)$, since all other parameters remain unchanged. However, in order to describe possible attractive interactions among domains, Vovk and colleagues introduced an interaction parameter χ dependent term ($F\chi$; Equation 2.13) into the free energy description of surface grafted FG Nup brushes. They were able to show that the layer height-to-grafting distance dependence of the different FG Nup brushes tested within the studies of Schoch *et al.* (2012)[18], Kapinos *et al.* (2014)[13], and Wagner *et al.* (2015)[19] behaves indeed as predicted by their theory. Specifically, they demonstrate that the layer height obeys a power law $h \sim g^p$, whereas the exponent p is correlated with χ (see Appendix Chapter 2). Thereby, brushes made from Nup214, Nup98, Nup153, and Nup62 and Nsp1 all lie between the boundaries p = 2/3 and p = 2. These limits correspond to an ideal non-cohesive, purely entropically stabilized (χ = 0) and a strongly cohesive, entirely collapsed polymer brush (χ = -2.5). In polymer physics jargon, one can also refer to a good solvent (Flory parameter v = 3/5) and a poor solvent (v = 1/3), respectively (with v^{-1}-1 = p).

Here, the free energy of interaction $F\chi$ is incorporated as contribution to the activation energy in a hypothesized free area model of unperturbed DGS – FG Nup diffusion, *i.e.* $D_{obs}(g\rightarrow\infty) = D_{obs}(c \approx 0)$ (see Equations 2.12 through 2.16). Diffusion is thereby pictured as the detachment from locally increased densities of DGS - FG Nup complexes into temporal voids within the FG Nup layer, *i.e.* FG Nup brushes on top of SLBs undergo spatiotemporal density fluctuations. Detached FG Nups temporary recoil and the DGS – FG Nup complexes displace until the over all dynamics drives them to rejoin transient aggregates. Measured diffusion constants therefore decline with shorter grafting distances (*i.e.* lower probability of free area) and stronger intermolecular interactions (*i.e*. increased lifetime of aggregates). Diffusion constants for DGS – Nsp1FF12 and DGS – Nsp1SS12 in dependence of their respective average grafting distance are shown in Figure 2.6. The additional F-F interaction lead to a faster decay of the DGS – Nsp1FF12 diffusion constant.

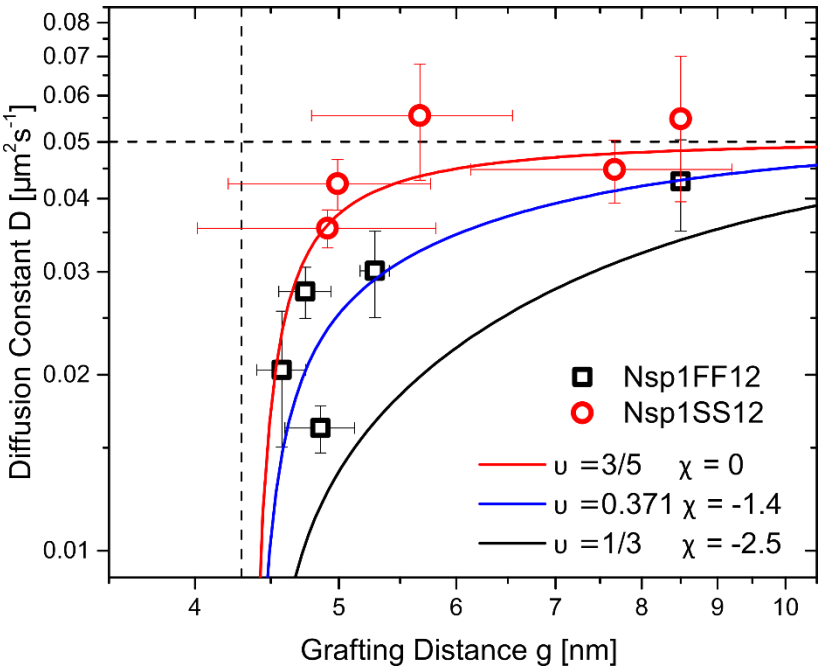

Figure 2.6: DGS – Nsp1FF12 and DGS – Nsp1SS12 diffusion constants in dependence of their respective average grafting distance. The additional hydrophobic F-F interactions lead to a stronger dependence on the grafting distance for DGS – Nsp1FF12. The red (ν = 3/5, χ = 0), blue (ν = 0.371, χ = -1.4) and black (v = 1/3, χ = -2.5) line are simulations of the exponential decay of the unperturbed DGS – FG Nup diffusion by Equation 2.14 ($D_{obs}(c \approx 0) \approx 0.05\ \mu m^2 s^{-1}$ (horizontal line), $r_{hyd} \approx 4.3$ nm (vertical line), Kuhn length b = 1.52 nm, $l = V_0^{1/3}$ = 1 nm, N = 71 chosen according to Vovk *et al.* (2016)[14]).

Table 2.4: DGS – Nsp1S Diffusion Dependence on DGS NTA(Ni). Diffusion is calculated from $\tau_{1/2}$ by means of Equation (2.6). Mobile fraction, half time and adjusted R^2 were obtained from fits to Equation (2.5).

%NTA	Diffusion [$\mu m^2 s^{-1}$]	Mobile Fraction	Adjusted R^2	N / n
1	0.055 ± 0.015	0.604 ± 0.129	0.686 ± 0.102	2 / 9
5	0.045 ± 0.006	0.873 ± 0.105	0.927 ± 0.009	2 / 12
20	0.055 ± 0.012	0.754 ± 0.152	0.848 ± 0.048	2 / 7
30	0.042 ± 0.004	0.566 ± 0.156	0.829 ± 0.047	2 / 7
40	0.036 ± 0.003	0.931 ± 0.073	0.885 ± 0.026	2 / 10

Table 2.5: Rh PE Diffusion Dependence of DGS NTA(Ni) Content After Nsp1SS12 Incubation. Diffusion is calculated from $\tau_{1/2}$ by means of Equation (2.6). Mobile fraction, half time and adjusted R^2 were obtained from fits to Equation (2.3).

%NTA	Diffusion [$\mu m^2 s^{-1}$]	Mobile Fraction	Adjusted R^2	N / n
0	0.585 ± 0.085	1.015 ± 0.022	0.943 ± 0.003	1 / 5
1	0.493 ± 0.092	1.013 ± 0.013	0.939 ± 0.004	2 / 9
5	0.412 ± 0.056	1.040 ± 0.012	0.943 ± 0.004	2 / 12
20	0.331 ± 0.075	1.030 ± 0.017	0.932 ± 0.010	2 / 8
30	0.268 ± 0.076	1.023 ± 0.019	0.920 ± 0.021	2 / 9
40	0.240 ± 0.063	0.997 ± 0.013	0.906 ± 0.006	2 / 16

2.6 FG Nup Layer Interaction with Kapβ1

Finally, the binding kinetics of Kapβ1 with lipid anchored brushes are compared to the kinetics with covalently end-grafted FG Nup brushes on gold by means of surface plasmon resonance (SPR; Note: SPR chips for the lipid based assays are hydrophobic. Liposomes therefore spread into supported lipid monolayers (SLM) and not into SLBs).

First, Nsp1FF12 and its variant Nsp1SS12 were investigated, since Nsp1SS12 should not bind Kapβ1 specifically due to the mutation from F to S. Indeed, regardless of the underlying substrate binding of Kapβ1 to Nsp1SS12 layers is entirely absent (see Figure 2.7A). The equilibrium analysis of Kapβ1 interaction with Nsp1FF12 on the other hand, displays a two phase behavior as expected from the Kap-centric notion (see Section 1.2.3) whereby the dissociation constants K_D obtained from two-component Langmuir isotherm fits are similar for both cases ($K_{D,1}$ ≈ 150 nM and $K_{D,2}$ ≈ 3 µM). An analysis of the layer heights h based on the methodology innovated by Schoch *et al.* (2013)[20] revealed $h_{Nsp1FF12,lipid}$ ≈ 4.9 nm and $h_{Nsp1FF12,Au}$ ≈ 6.7 nm indicative for a sparse layer thereby showing a comparable capacity of incorporating ~1 layer of Kapβ1 (see Figure 2.7B; lipid mediated immobilization is corrected for the lipid height).

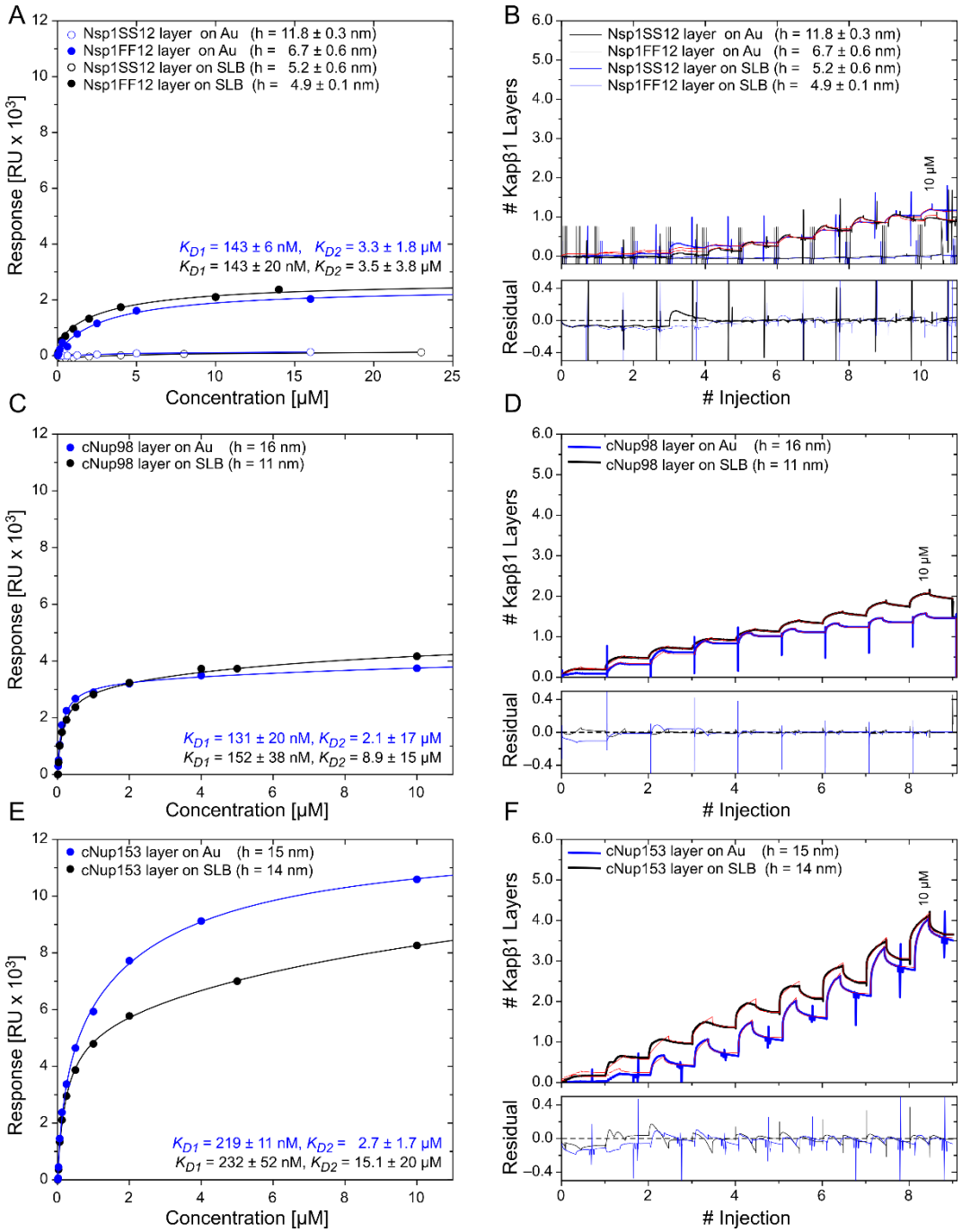

Figure 2.6: Comparison of Kapβ1 interactions with FG Nup brushes on different substrates. SPR measurements of Kapβ1 binding towards FG Nup layers immobilized on gold and on SLMs reveal similar kinetics, specificity and conformational responses. (**A**), (**C**) and (**E**) The equilibrium analysis of Kapβ1 interaction displays a two phase behavior towards yeast Nsp1FF12, human Nup98 and Nup153 FG domain layers but no specific binding to Nsp1SS12. Solid lines represent two-component Langmuir isotherm fits. (**B**), (**D**) and (**F**) Kinetic analysis shows that the conformational changes of lipid anchored FG Nup layers upon titration of Kapβ1 are reminiscent of covalently grafted brushes, *i.e.* Nup153 layers undergo a "compact extension" and Nup98 layers show "partial penetration" independent of the underlying substrate. Red lines in are fits to the kinetic model as found in Schoch *et al.* (2013)[20].

Second, layers built from human Nup153 and Nup98 FG domains were tested, since they showed distinct conformational differences upon Kapβ1 interaction in previous SPR studies on gold[13]. In particular, Nup153 layers were described to undergo a "compact extension" (*i.e* multiple layers of Kapβ1 are incorporated) and Nup98 layers show "partial penetration" (*i.e.* Kap β1 is incapable to penetrate the layer due to intrinsic cohesion). The analysis of layer heights leads to $h_{Nup153,lipid}$ = 14 nm ($h_{Nup153,Au}$ = 15 nm) and $h_{Nup98,lipds}$ = 11 nm ($h_{Nup98,Au}$ = 16 nm), indicative for a close-packed conformation (Figure 2.7B; $r_{hyd,Nup153}$ = 5.1 ± 3.2 nm and $r_{hyd,Nup98}$ = 5.6 ± 1.6 nm [ref. 13]). Again, the equilibrium analysis of Kapβ1 interaction displays a two phase behavior for all four brush assays and two-component Langmuir isotherm fits yield comparable dissociation constants K_D ($K_{D,1}$ ≈ 100 – 200 nM and $K_{D,2}$ ≈ 10 µM) independent of the underlying substrate (Figure 2.7C and E). The conformational changes of lipid anchored FG Nup layers upon titration are also reminiscent of covalently grafted brushes (Figure 2.7B). While Nup98 - after applying 10 µM Kapβ1 - is only partially penetrated by ∼1 Kapβ1 layer, Nup153 incorporates up to ∼3 Kapβ1 layers. For a better comparability, association and dissociation times and numbers of injections in the sensograms have been normalized.

Two-dimensional kinetic maps derived from the sensograms of Kapβ1 binding allow one to resolve different kinetic states. The fractional abundance of the "slow phase" and "fast phase" kinetic states for Nsp1FF12, Nup98 and Nup153 FG domains grafted to Au or DGS NTA(Ni) containing lipid layers coincide remarkably (see Appendix Chapter2).

2.7 Conclusion

His_6-tagged FG domains anchored onto planar glass surfaces *via* their interaction with NTA(Ni) modified lipids proved to show the same characteristics upon Kapβ1 binding as covalently end-grafted domains on planar Au surfaces *via* sulfide bonds. However, a lipid-based substrate for FG domain immobilization resembles the *in vivo* situation better than assays formed on bare metal or glass. The direct comparability of the binding kinetics with Kapβ1 amongst the different assays hence strengthens the findings and conclusions drawn from previous *in vitro* studies[13,18,19,21], *i.e.* Kap-centric regulation of the NCT. Moreover, the here presented immobilization assay brings further advantages: First, it is straightforward applicable to different substrates, as seen for hydrophilized glass (forming a SLB) and hydrophobically modified Au (forming a SLM) surfaces. Second, it provides the means for a fluorescence based deduction of the average grafting distance amongst immobilized FG domain brushes as shown by two-color FRAP and third, it allows one to determine the effect of attractive interactions on the intrinsic brush dynamics.

Furthermore, the notion of an immobile molecular brush on top of a mobile lipid substrate is fascinating *per se*. It opens the door towards speculations of how surface anchored IDPs might regulate the milieu of underlying cellular membranes *in vivo*, such as stabilizing lipid rafts *via* a localized increase of the drag force within the SLB or by opposing lipid phase separation by sterical exclusion.

2.8 Materials and Methods

2.8.1 Preparation of the Sample Chamber

Homemade PDMS (10:1 Sylgard(R) 184, Dow Corning) cells containing two connected reservoirs (80 µl) were attached to borosilicate coverslips (24 x 60 mm, Nr. 1, Menzel Glass) *via* O_2 plasma activation (13.56 MHz, 50 W, 5 sccm, 30 s, Femto, DienerElectronics) and post-baking (10 min at 120 °C). The coverslip surface was hydrophilized immediately before applying filtered (0.22 µm, TRP) PBS solution (pH 7.2, 150 mM NaCl, Gibko) to the reservoirs by exposure to a second O_2 plasma treatment (13.56 MHz, 12.5 W, 5 sccm, 5 min). Subsequently, the PBS was exchanged with liposome solution to permit single lipid bilayer (SLB) formation by spontaneous spreading (Figure 2.1) on the coverslip surface for 10 min. The entire cell was immersed in a large volume of fresh PBS buffer for 45 – 60 min under constant shaking to remove remaining, non-ruptured SUVs. Prior to multicolor FRAP measurements, SLBs were functionalized by incubation overnight at 4 °C with different, fluorescently labelled Nsp1 fragments in PBS (see above) *via* NTA(Ni) – His_6 interaction.

2.8.2 Liposome Composition, Formation and Characterization

Liposomes of varying contents of 1,2-dioleoyl-*sn*-glycero-3-phosphocholine (DOPC, 99.9 – 59.9 %mol) and 1,2-dioleoyl-*sn*-glycero-3-[(N-(5-amino-1-carboxypentyl)iminodiacetic acid)succinyl] (nickel salt) (DGS NTA(Ni), 0 – 40 %mol) were labelled with a stable amount of 0.1 %mol 1,2-dioleoyl-*sn*-glycero-3-phosphoethanolamine-N-(lissamine rhodamine B sulfonyl) (ammonium salt) (Rh PE). All lipids have been purchased from Avanti Polar Lipids, Inc. in powder form. The lipids have been dissolved in chloroform prior to use, mixed together in the desired composition in a round flask and blow dried with N_2. Chloroform moieties were removed by desiccation for at least 2 h at 20 mbar and large multilaminar vesicles (LMVs) were then formed by five freezing-thaw cycles (freezing in liquid N_2 followed by thawing in a 42 °C water bath and vigourous vortexing for 30 s) in PBS (pH 7.2, 150 mM NaCl, Gibko) to a final lipid concentration of 2 mM. LMVs were homogenized both by sonication (30 min at 80 kHz, pulsed, 21 °C, Elmasonic P) and by extrusion (50 nm and 30 nm track-etched polycarbonate membranes, 10 extrusions each, Whatman) to form small unilamellar vesicles (SUVs) of ~ 30 nm. Monodispersity and size of the SUVs have been assessed by dynamic light scattering measurement immediately after formation and prior to usage.

2.8.3 Kapβ1 Constructs, Expression and Purification

Full-length human Kapβ1 was amplified by PCR and inserted into a *NcoI–BamHI* digested pETM-11 expression vector (EMBL Protein Expression and Purification Facility). N-terminal His_6-tagged Kapβ1 was expressed in E. coli BL21 (DE3) cells at 30 °C overnight and purified on a Ni-NTA column (buffer 1: 10 mM TrisHCl, pH 7.5, 100 mM NaCl, 1mM DTT; eluted with 80–500 mM imidazole) followed by gel-filtration Superdex 200 (Superdex 200 16/600, GE Healthcare). Purified protein was analysed by 15% SDS–PAGE and selected fractions containing Kapβ1 were pooled and dialysed back against buffer 1. The His_6 tag was cleaved by incubation with 1:100 units of TEV proteases overnight at 4 °C. The cleaved construct was again purified on a Ni-NTA column and the flow through collected and concentrated. Absence of the His_6-tag was confirmed by Western blotting (Anti-His: 1:1000, Anti-Mouse: 1:1000). For FRAP experiments, Kapβ1 was labelled with Alexa Fluor647 carboxylic acid, succinimidyl ester (Alexa Fluor647 NHS ester) in filtered PBS buffer using the standard labelling procedure for amine-reactive probes (Invitrogen Protocols). Conjugation efficiency was determined by spectrophotometry (Nanodrop 2000).

2.8.4 FRAP Procedure

Fluorescence recovery after photobleaching measurements were performed on a 3i spinning disk confocal based on a Zeiss Axio Observer stand, equipped with a 0.75 NA 40x plan fluorite objective (EC Plan NeoFLUOR, Zeiss), three diode lasers (488 nm, 555 nm and 639 nm), appropriate emission and excitation band pass filter cubes and an ultrasensitive back-illuminated EMCCD camera (Evolve(R) 512, Photometrics). The FRAP region was chosen to be 15 μm^2 throughout all measurements but acquisition speed has been varied between 100 ms and 1 s, depending on the experiments, number of channels and exposure times used.

2.8.5 Recovery Analysis

FRAP curves were analyzed by a custom-made Matlab program, which I termed FRAPalyzer©. Four different models have been considered: pure diffusion, reaction dominant first-order, reaction dominant second-order and a full reaction-diffusion model derived from first principles[50]. To distinguish between the models, adjusted R^2 of the fits were compared and the models chosen accordingly. It turned out that neither the reaction dominant second-order nor the full model performed significantly better than the pure diffusion or reaction dominant first-order limits. Results obtained by these two models were compared by means of a phenomenological diffusion constant derived from Axelrod *et al.*[48] solution for

circular ROIs. All relevant data can be found in the main text. Further analysis information (Matlab code, model derivations etc.) can be found in the Appendix of Chapter 3.

2.8.6 TIRF Imaging

The total internal reflection fluorescence images were obtained with a Leica DMI6000B inverted microscope stand, equipped with a TIRF module (AM TIRF MC, Leica Microsystems), a 1.46 NA 100x oil immersion objective (TIRF, Leica Microsystems) with an additional tube magnification of 1.6, three solid diode lasers with wavelengths of (488 nm, 561 nm, and 635 nm), appropriate emission and excitation band pass filter cubes and an EMCCD camera (C9100-02, Hamamatsu, Japan), resulting pixel size is 50 nm/pixel. Samples were automatically illuminated at the correct angle to achieve an evanescent wave decay length of 70 nm in TIRF mode. EM gain and exposure time were kept constant during acquisition.

2.8.7 SPR Measurements and Analysis

SPR measurements were performed on bare Au (SIA Kit Au, GE Healthcare) or hydrophobic, alkanethiol modified Au sensor chips (HPA, GE Healthcare) in a Biacore T200 instrument (GE Healthcare). Au sensor surfaces were sonicated in acetone, isopropanol and ethanol for 15 min, respectively, and blow dried with N_2 followed by 30 min UVO cleaning (Model 42A-220; Jelight Company Inc.) and mounted on the sample holder for immediate SPR usage. HPA sensor chips were used as obtained. Detailed description of the SPR measurement and analysis protocols can be found in the Appendix of Chapter 2.

2.9 References

1. Ward, J. J., Sodhi, J. S., McGuffin, L. J., Buxton, B. F. & Jones, D. T. Prediction and Functional Analysis of Native Disorder in Proteins from the Three Kingdoms of Life. *J. Mol. Biol.* **337,** 635–645 (2004).
2. Wright, P. E. & Dyson, H. J. Linking folding and binding. *Current Opinion in Structural Biology* **19,** 31–38 (2009).
3. Uversky, V. N. & Dunker, A. K. Multiparametric analysis of intrinsically disordered proteins: Looking at intrinsic disorder through compound eyes. *Analytical Chemistry* **84,** 2096–2104 (2012).
4. Uversky, V. N. A decade and a half of protein intrinsic disorder: Biology still waits for physics. *Protein Science* **22,** 693–724 (2013).
5. Tzeng, S.-R. & Kalodimos, C. G. Protein activity regulation by conformational entropy. (2012). *Nature* **488,** 236–240 (2012)
6. Tompa, P. Intrinsically disordered proteins: A 10-year recap. *Trends in Biochemical Sciences* **37,** 509–516 (2012).
7. Uversky, V. N. Multitude of binding modes attainable by intrinsically disordered proteins: a portrait gallery of disorder-based complexes. *Chem. Soc. Rev.* **40,** 1623–1634 (2011).
8. Liu, Z. & Huang, Y. Advantages of proteins being disordered. *Protein Science* **23,** 539–550 (2014).
9. Kumar, S., Yin, X., Trapp, B. D., Hoh, J. H. & Paulaitis, M. E. Relating interactions between neurofilaments to the structure of axonal neurofilament distributions through polymer brush models. *Biophys. J.* **82,** 2360–2372 (2002).
10. Busch, D. J. *et al.* Intrinsically disordered proteins drive membrane curvature. *Nat. Commun.* **6,** 7875-1–7875-11 (2015).
11. Lim, R. Y. *et al.* Nanomechanical basis of selective gating by the nuclear pore complex. *Science* **318,** 640–643 (2007).
12. Uversky, V. N. & Dunker, A. K. Understanding protein non-folding. *Biochimica et Biophysica Acta - Proteins and Proteomics* **1804,** 1231–1264 (2010).
13. Kapinos, L. E., Schoch, R. L., Wagner, R. S., Schleicher, K. D. & Lim, R. Y. H. Karyopherin-centric control of nuclear pores based on molecular occupancy and kinetic analysis of multivalent binding with FG nucleoporins. *Biophys. J.* **106,** 1751–1762 (2014).
14. Vovk, A. *et al.* Simple biophysics underpins collective conformations of the intrinsically disordered proteins of the nuclear pore complex. *Elife* **5,** 10785-1–10785-29 (2016).

15. Milles, S. *et al.* Plasticity of an Ultrafast Interaction between Nucleoporins and Nuclear Transport Receptors. *Cell* **163,** 734–745 (2015).

16. Tu, L.-C., Fu, G., Zilman, A. & Musser, S. M. Large cargo transport by nuclear pores: implications for the spatial organization of FG-nucleoporins. *EMBO J.* **32,** 3220–3230 (2013).

17. Raveh, B. *et al.* Slide-and-exchange mechanism for rapid and selective transport through the nuclear pore complex. *Proc. Natl. Acad. Sci. U. S. A.* **113,** 2489-2497 (2016).

18. Schoch, R. L., Kapinos, L. E. & Lim, R. Y. H. Nuclear transport receptor binding avidity triggers a self-healing collapse transition in FG-nucleoporin molecular brushes. *Proc. Natl. Acad. Sci. U. S. A.* **109,** 16911-1–16911-6 (2012).

19. Wagner, R. S., Kapinos, L. E., Marshall, N. J., Stewart, M. & Lim, R. Y. H. Promiscuous Binding of KaryopherinÎ²1 Modulates FG Nucleoporin Barrier Function and Expedites NTF2 Transport Kinetics. *Biophys. J.* **108,** 918–927 (2015).

20. Schoch, R. L. & Lim, R. Y. H. Non-interacting molecules as innate structural probes in surface plasmon resonance. *Langmuir* **29,** 4068–4076 (2013).

21. Schleicher, K. D. *et al.* Selective transport control on molecular velcro made from intrinsically disordered proteins. *Nat. Nanotechnol.* **9,** 525–530 (2014).

22. Lazzara, T. D., Behn, D., Kliesch, T.-T., Janshoff, A. & Steinem, C. Phospholipids as an alternative to direct covalent coupling: Surface functionalization of nanoporous alumina for protein recognition and purification. *J. Colloid Interface Sci.* **366,** 57–63 (2012).

23. Yusko, E. C. *et al.* Controlling protein translocation through nanopores with bio-inspired fluid walls. *Nat. Nanotechnol.* **6,** 253–260 (2011).

24. Richter, R. P., Bérat, R. & Brisson, A. R. Formation of solid-supported lipid bilayers: An integrated view. *Langmuir* **22,** 3497–3505 (2006).

25. Hernández-Ainsa, S. *et al.* Lipid-coated nanocapillaries for DNA sensing. *Analyst* **138,** 104–106 (2013).

26. Lind, T. K. & Cárdenas, M. Understanding the formation of supported lipid bilayers via vesicle fusion—A case that exemplifies the need for the complementary method approach (Review). *Biointerphases* **11,** 20801-1–20801-12 (2016).

27. Eisele, N. B., Labokha, A. a., Frey, S., Görlich, D. & Richter, R. P. Cohesiveness tunes assembly and morphology of FG nucleoporin domain meshworks - Implications for nuclear pore permeability. *Biophys. J.* **105,** 1860–1870 (2013).

28. Saxton, M. J. Lateral diffusion in an archipelago. The effect of mobile obstacles. *Biophys. J.* **52,** 989–997 (1987).

29. Deverall, M. a. *et al.* Membrane lateral mobility obstructed by polymer-tethered lipids studied at the single molecule level. *Biophys. J.* **88,** 1875–86 (2005).

30. Schram, V., Tocanne, J. F. & Lopez, A. Influence of obstacles on lipid lateral diffusion: computer simulation of FRAP experiments and application to proteoliposomes and biomembranes. *Eur. Biophys. J.* **23,** 337–348 (1994).

31. Watts, T. H., Brian, A. A., Kapplert, J. W., Marrackt, P. & Mcconnell, H. M. Antigen presentation by supported planar membranes containing affinity-purified I-Ad. *Immunology* **81,** 7564–7568 (1984).

32. McConnell, H. M., Watts, T. H., Weis, R. M. & Brian, A. A. Supported planar membranes in studies of cell-cell recognition in the immune system. *BBA - Rev. Biomembr.* **864,** 95–106 (1986).

33. Richter, R., Mukhopadhyay, A. & Brisson, A. Pathways of lipid vesicle deposition on solid surfaces: a combined QCM-D and AFM study. *Biophys. J.* **85,** 3035–3047 (2003).

34. Castellana, E. T. & Cremer, P. S. Solid supported lipid bilayers: From biophysical studies to sensor design. *Surf. Sci. Rep.* **61,** 429–444 (2006).

35. Hamai, C., Yang, T., Kataoka, S., Cremer, P. S. & Musser, S. M. Effect of average phospholipid curvature on supported bilayer formation on glass by vesicle fusion. *Biophys. J.* **90,** 1241–1248 (2006).

36. Johnson, J. M., Ha, T., Chu, S. & Boxer, S. G. Early steps of supported bilayer formation probed by single vesicle fluorescence assays. *Biophys. J.* **83,** 3371–3379 (2002).

37. Seantier, B., Breffa, C., Felix, O. & Decher, G. Dissipation-enhanced quartz crystal microbalance studies on the experimental parameters controlling the formation of supported lipid bilayers. *J. Phys. Chem. B* **109,** 21755–21765 (2005).

38. Schönherr, H., Johnson, J. M., Lenz, P., Frank, C. W. & Boxer, S. G. Vesicle adsorption and lipid bilayer formation on glass studied by atomic force microscopy. *Langmuir* **20,** 11600–11606 (2004).

39. Cremer, P. S. & Boxer, S. G. Formation and Spreading of Lipid Bilayers on Planar Glass Supports. *J. Phys. Chem. B* **103,** 2554–2559 (1999).

40. Zhdanov, V. P. & Kasemo, B. Comments on rupture of adsorbed vesicles. *Langmuir* **17,** 3518–3521 (2002).

41. Kasson, P. M. & Pande, V. S. Molecular dynamics simulation of lipid reorientation at bilayer edges. *Biophys. J.* **86,** 3744–3749 (2004).

42. Jiang, F. Y., Bouret, Y. & Kindt, J. T. Molecular dynamics simulations of the lipid bilayer edge. *Biophys. J.* **87,** 182–192 (2004).

43. Chen, Y., Lagerholm, B. C., Yang, B. & Jacobson, K. Methods to measure the lateral diffusion of membrane lipids and proteins. *Methods* **39,** 147–153 (2006).

44. Macháň, R. & Hof, M. Lipid diffusion in planar membranes investigated by fluorescence correlation spectroscopy. *BBA - Biomembr.* **1798,** 1377–1391 (2010).

45. Guo, L. *et al.* Molecular diffusion measurement in lipid bilayers over wide concentration ranges: A comparative study. *ChemPhysChem* **9,** 721–728 (2008).

46. Soumpasis, D. M. Theoretical analysis of fluorescence photobleaching recovery experiments. *Biophys. J.* **41,** 95–97 (1983).

47. Lorén, N. *et al.* Fluorescence recovery after photobleaching in material and life sciences: putting theory into practice. *Q. Rev. Biophys.* **48,** 323–387 (2015).

48. Axelrod, D., Koppel, D. E., Schlessinger, J., Elson, E. & Webb, W. W. Mobility measurement by analysis of fluorescence. *Biophys. J.* **16,** 1055–1069 (1976).

49. Bulinski, J. C., Odde, D. J., Howell, B. J., Salmon, T. D. & Waterman-Storer, C. M. Rapid dynamics of the microtubule binding of ensconsin in vivo. *J. Cell Sci.* **114,** 3885–3897 (2001).

50. Sprague, B. L., Pego, R. L., Stavreva, D. A. & McNally, J. G. Analysis of binding reactions by fluorescence recovery after photobleaching. *Biophys. J.* **86,** 3473–3495 (2004).

51. Kang, M., Day, C. A., Di Benedetto, E. & Kenworthy, A. K. A quantitative approach to analyze binding diffusion kinetics by confocal FRAP. *Biophys. J.* **99,** 2737–2747 (2010).

52. Vaz, W. L. C., Goodsaid-Zalduondo, F. & Jacobson, K. Lateral diffusion of lipids and proteins in bilayer membranes. *FEBS Lett.* **174,** 199–207 (1984).

53. Almeida, P. F., Vaz, W. L. & Thompson, T. E. Lateral diffusion and percolation in two-phase, two-component lipid bilayers. Topology of the solid-phase domains in-plane and across the lipid bilayer. *Biochemistry* **31,** 7198–7210 (1992).

54. Tahir-Kheli, R. A. Correlation factors for atomic diffusion in nondilute multicomponent alloys with arbitrary vacancy concentration. *Phys. Rev. B* **28,** 3049–3056 (1983).

55. Van Beijeren, H. & Kutner, R. Mean square displacement of a tracer particle in a hard-core lattice gas. *Phys. Rev. Lett.* **55,** 238–241 (1985).

56. Jacobson, K. Lateral diffusion in membranes. *Cell Motil.* **3,** 367–373 (1983).

57. Alexander, S. Adsorption of chain molecules with a polar head a scaling description. *J. Phys.* **38,** 983–987 (1977).

58. de Gennes, P. G. Conformations of Polymers Attached to an Interface. *Macromolecules* **13,** 1069–1075 (1980).

59. de Gennes, P. G. Polymers at an interface; a simplified view. *Advances in Colloid and Interface Science* **27,** 189–209 (1987).

60. Jönsson, P., Beech, J. P., Tegenfeldt, J. O. & Höök, F. Shear-Driven Motion of Supported Lipid Bilayers in Microfluidic Channels. *J. Am. Chem. Soc.* **131,** 5294–5297 (2009).

61. Zhang, L. & Granick, S. Lipid diffusion compared in outer and inner leaflets of planar supported bilayers. *J. Chem. Phys.* **123,** 211104-1–211104-4 (2005).

62. Zwang, T. J., Fletcher, W. R., Lane, T. J. & Johal, M. S. Quantification of the Layer of Hydration of a Supported Lipid Bilayer. *Langmuir* **26,** 4598–4601 (2010).

63. Sakiyama, Y., Mazur, A., Kapinos, L. E. & Lim, R. Y. H. Spatiotemporal dynamics of the nuclear pore complex transport barrier resolved by high-speed atomic force microscopy. *Nat. Nanotechnol.* **11,** 719–723 (2016).

Chapter 3

Karyopherinβ1 Interacting with Lipid Bilayer Immobilized FG Nup Layers

3 Karyopherinβ1 Interacting with Lipid Bilayer Immobilized FG Nup Layers

3.1 Introduction

Determining the diffusion behavior of Kapβ1 within an FG domain layer by the means of FRAP turned out not to be feasible. The required high concentration of layer-bound labelled Kapβ1 for proper recovery analysis is not maintained for the entire envisioned Kapβ1 titration range due to the exchange with unlabelled Kapβ1 in solution. Titration of labelled Kapβ1 on the other hand introduces an impractically high fluorescent background.

Here, fluorescence correlation spectroscopy (FCS) techniques were employed to overcome these limitations. At the expense of complicated experimental procedures, sophisticated data analysis and long measurement times, correlation based approaches bear a crucial advantage over FRAP: Correlation increases with decreasing sample size, *i.e.* the number of fluorescent particles correlated to each other. A thorough introduction is accounting for the details of the here applied FCS techniques (see Section 3.2). The presented extensions to classical FCS lay the foundation for the later experiments on FG domain layer-bound Kapβ1.

Similar to the samples for the recovery experiments in Chapter 2, FG domains were anchored onto SLBs formed *via* spontaneous liposome spreading. The influence of Nsp1FF12 layer formation on the lateral diffusivity of RhPE tracers was then determined by the means of fluorescence lifetime correlation spectroscopy (FLCS) z-scans (see Section 3.3).

Immobilized Nsp1FF12 layers were incubated with labelled Kapβ1 and exposed to different concentrations of unlabelled Kapβ1 in the liquid phase. Fluorescent lifetime cross-correlation spectroscopy (FLCCS) sheds light on the microscopic details of Kapβ1 motion within these crowded FG domain layers over the entire titration range of Kapβ1 from 1 nM to 10 µM (see Section 3.4).

3.2 Theory and Background

3.2.1 Fluorescence Correlation Spectroscopy

FCS is based on the temporal autocorrelation of intensity fluctuations *FI(t)* within a well-defined confocal volume V_0 (see inset Figure 3.1)[1–4]. These fluctuations predominantly originate from diffusion of the fluorescent species through, as well as photophysical or photochemical reactions within this volume. The autocorrelation function (ACF) hence contains information about physical parameters such as diffusion time and local concentration, but also about the kinetics of intermolecular or intramolecular reactions.

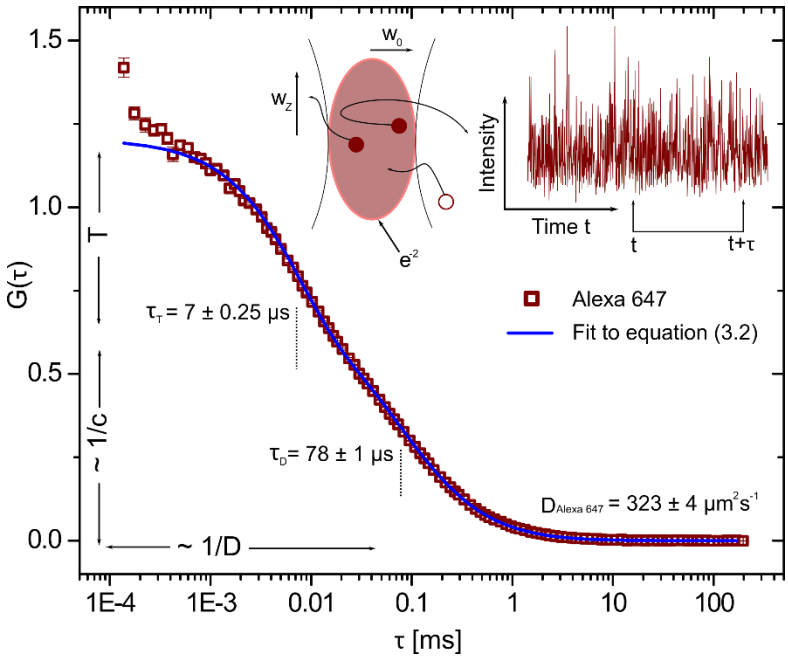

Figure 3.1: Principle of fluorescence correlation spectroscopy (FCS). Fluorescence intensity fluctuations *FI(t)* within a confocal volume V_0 - defined by the extent in the focal plane w_0 and along the z-axis w_z - are auto correlated over a range of lag times τ according to Equation (3.1). The obtained autocorrelation curve (ACF) contains information about the origin of the intensity fluctuations in different time domains (see main text). The above autocorrelation function for the fluctuations from 2.5 nM Alexa 647 in PBS within a $V_0 \approx 1$fl are fitted by a model including triplet state kinetics (see Equation 3.2). The fit reveals a substantial triplet state fraction of 0.423 ± 0.006 with a characteristic triplet decay time τ_T of 7 ± 0.25 µs and a diffusion time τ_D of 78 ± 1 µs leads to a diffusion constant of 323 ± 4 $\mu m^2 s^{-1}$ (compared to a literature value in water of 330 ± 10 $\mu m^2 s^{-1}$)[5].

The ACF is a measure of the self-similarity of the fluorescent signal after a lag time τ (see inset Figure 3.1) and is defined by

$$G(\tau) = \frac{<FI(t)FI(t+\tau)>}{<FI(t)>^2} \quad (3.1)$$

where the angle brackets indicate averaging over all values of time *t*. A representative autocorrelation function obtained by FCS of freely diffusing Alexa 647 dye is shown in Figure 3.1 and discussed subsequently.

The number of fluorescent particle *N(t)* within the confocal volume is unlikely to change significantly within very short time intervals. Therefore, intensity fluctuations faster than $\sim 10^{-5}$ s and hence changes in *G(τ)* do not stem from diffusive variations of the number of fluorophores.

On a nanosecond timescale, *G(τ)* rises to a maximum due to photon antibunching[6]. The ACF in Figure 3.1 only displays the subsequent decay as *FI(t)* in the present example is correlated to *FI(t+τ)* only for lag times $\tau > 10^{-7}$ s. Intensity fluctuations on the low microsecond timescale are caused by photophysical or photochemical effects such as intersystem-crossing to non-fluorescent triplet states with characteristic lifetimes τ_T in the range of $\sim 10^{-6}$ s (here $\tau_T \approx 7$ µs)[7].

At longer timescales, *G(τ)* is dominated by fluctuations in *N(t)* due to the translational diffusion of fluorescent molecules into or out of the confocal volume V_0. For lag times much longer than the average residence time τ_D within V_0 (hereafter called the diffusion time), the particle numbers *N(t)* and *N(t+τ)* are not correlated anymore and the ACF drops to zero, *i.e.* $G(\infty) \rightarrow 0$.

Due to these distinct time domains, overall autocorrelation curves can be separated into the respective contributions from the particle motion and triplet kinetics, *e.g.* $G(\tau) = G(\tau)_{kinetics} * G(\tau)_{motion}$ (if the translational diffusion is unaltered by fast intra- and intermolecular interactions)[8].

Assuming that the spatial distribution of the detected light can be approximated by a 3D Gaussian distribution, the fit model for the simple case of single-component, three-dimensional Brownian motion of free dye including triplet states kinetics is given by[7]

$$G(\tau)_{3D} = \underbrace{\frac{(1-T+Te^{-\frac{\tau}{\tau_T}})}{(1-T)}}_{G(\tau)_{kinetics}} \frac{1}{N} \underbrace{\frac{1}{1+(\frac{\tau}{\tau_D})} \sqrt{\frac{1}{1+(\frac{\tau}{\tau_D})(\frac{w_0}{w_z})^2}}}_{G(\tau)_{3D\ motion}} \quad (3.2)$$

with *T* the triplet state fraction, *N* the average number of fluorescent particles *<N(t)>*, w_0 the radius of the confocal volume in lateral and w_z in axial direction, *i.e.* the boundaries describing the decay of the 3D Gaussian distribution to e^{-2} (see inset Figure 3.1). Equation 3.2 also reveals that the amplitude *G(0)* is inversely proportional to *N* if all fluctuations arise only from local deviations in the particle concentration, *i.e. T = 0* (or by omission of the contributions from reaction kinetics $G(\tau)_{kinetics}$).

In the case of multiple non-interacting components *M* the overall autocorrelation function is the linear combination of the individual $G_i(\tau)$ weighted by their fractional contribution F_i to the total fluorescence[9]

$$G(\tau)_{3D,Multi} = \sum_{i=1}^{M} F_i\, G(\tau)_{i,3D} \quad (3.3)$$

As for the analysis of FRAP recovery curves (see Section 2.2.1), numerous models for the description of ACFs acquired in various experimental settings have been reported. The choice of the right fitting model thereby relies on the *a priori* knowledge of the sample properties and qualitative interpretation of the ACF shape. In the following sections fitting models relevant for the present study will be introduced one by one. However, exhaustive derivations of the respective models are omitted and the interested reader will be referred to the corresponding literature.

3.2.2 Fluorescence Lifetime Correlation Spectroscopy

FCS measurements as introduced in Section 3.2.1 suffer from several correlated and uncorrelated parasitic signal components. The most abundant correlated artifacts are detector dependent afterpulses, *i.e.* false photon counts resulting from transient effects induced by a real, arriving photon. These transient effects occur usually on the micro- or sub microsecond timescale and can be misinterpreted as fast photophysical or photochemical processes of the fluorescent species under investigation.

In contrast, uncorrelated sources of parasitic signals such as thermal noise or scattered light lower the amplitude *G(0)* and lead consequently to an overestimation of *N* (see Section 3.2.1). This effect is most prominent for low fluorophore concentrations, due to the reduced signal-to-noise ratio, and close to interfaces as a result of enhanced scattering.

Fluorescence lifetime correlation spectroscopy (FLCS)[10], the fusion of classical FCS with time-correlated single photon counting (TCSPC), allows for the elimination of both the correlated and the uncorrelated artifacts. The difference between FLCS and FCS is illustrated in Figure 3.2 by means of a supported lipid bilayer containing traces of fluorescently labelled lipids[11].

While FCS measurements can be performed under continuous wave (CW) illumination, TCSPC (and therefore FLCS) depends on a pulsed, sub-nanosecond excitation. In TCSPC, arrival times of single fluorescence photons are measured relative to the respective excitation pulse with picosecond precision (see Figure 3.2A)[12]. The arrival times are expressed in multiples of the time resolution (here 16 ps), also called channel numbers *j*. Simultaneously, and similar to FCS, photon arrival times are also recorded with respect to the start of the experiment with nanosecond resolution (here 25 ns). Thus, detected photons in FLCS are tagged with two independent timings.

Arrival time histograms A_j (the overall fluorescence decay) are obtained by sorting the TCSPC arrival times according to their delay, *i.e.* channel number *j* (see Figure 3.2B). These histograms incorporate photons from any source (s = 1, 2, …, S-1, S) in the sample and are hence a linear combination of individual decay patterns $p_j^{(s)}$ multiplied by the number of photons $q^{(s)}$ received from the respective source s,

$$A_j = \sum_{s=1}^{S} q^{(s)} p_j^{(s)} \quad (3.4)$$

In the present example (see Figure 3.2B), the arrival time histogram is only composed by the photons emitted by the fluorescently labelled lipids and an uncorrelated background of scattered light and thermal noise, *i.e.* two sources.

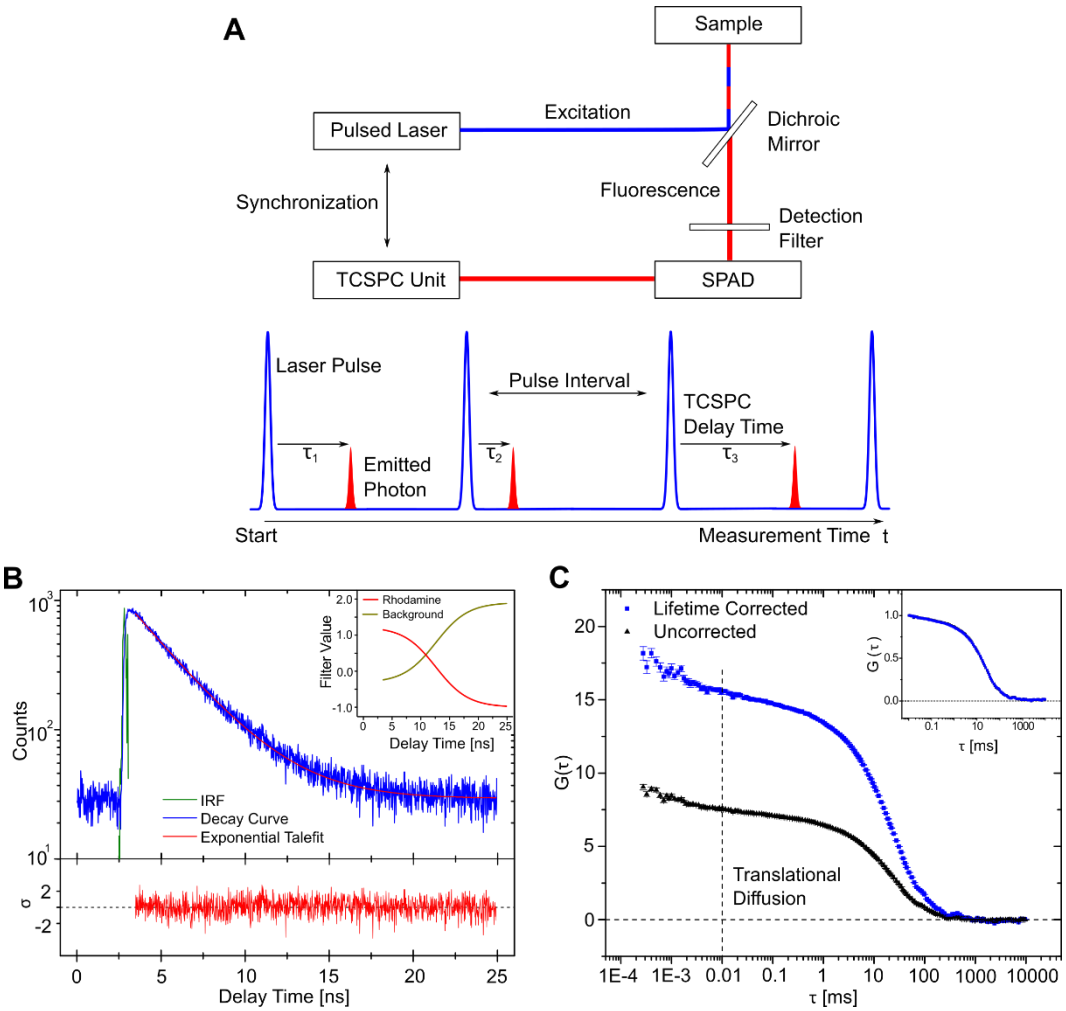

Figure 3.2: Principle of fluorescence lifetime correction based on time-correlated single photon counting (TCSPC). **A**, Schematics of TCSPC. Arrival times of single fluorescence photons - emitted by fluorophores in the sample plane - at the single photon avalanche detector (SPAD) are measured relative to the respective excitation pulse with picosecond resolution (here 16 ps). Sorting the photons according to their arrival times into a histogram with a bin size equal to the time resolution (also called channel number) results in a fluorescence decay curve. **B**, Fluorescence decay curve of Rhodamine B labelled lipids in a supported lipid bilayer. The fluorescence decay after the excitation pulse (whose shape is given by the instrument response function IRF) is fitted by a single exponential decay with the decay constant equal to the fluorescence lifetime τ_F (here 2.8 ± 0.05 ns). To perform the lifetime correction, contributions of each detected photon to the ACF are weighed depending on its arrival time by filter functions calculated from the decay curve. Inset: Filter functions for the case of Rhodamine B and uncorrelated background. **C**, Comparison between uncorrected (FCS) and corrected (FLCS) autocorrelation functions reveals a pronounced influence on the amplitude of the ACF and hence on the apparent number of particles within the illumination area. Inset: The lifetime filtering has no effect on the measured diffusion time, which is illustrated by the perfect overlay of the corrected and uncorrected curve after normalization at 10 µs (thereby only including the time domain relevant for translational diffusion).

Photons originating from the background are uniformly distributed amongst the channel numbers *j* and do not alter the shape of the overall fluorescence decay. The distribution A_j follows therefore exclusively the shape of the decay pattern of the fluorescently labelled lipids and a single exponential decay fit (the fluorescence lifetime) is sufficient to describe A_j.

Contrary to FCS, where each detected photon contributes equally to $G(\tau)$, in FLCS single photons contribute to the autocorrelation function of each source $G(\tau)^{(s)}$ with a certain weight depending on their arrival time (see inset Figure 3.2B)

$$G(\tau)^{(s)} = \frac{<\sum_j f_j^{(s)} A_j(t) \sum_j f_j^{(s)} A_j(t+\tau)>}{<\sum_j f_j^{(s)} A_j(t)>^2} \quad (3.5)$$

The thorough mathematical derivation of the so called filter function $f_j^{(s)}$ and their characteristic features can be found elsewhere[13]. However, the pronounced effect of lifetime filtering on the autocorrelation curve of fluorescently labelled lipids is demonstrated in Figure 3.2C and 3.3D. As expected, the uncorrelated background leads to a lowering of $G(0)$ which is corrected in the case of lifetime filtering. The correction does not comprise the determination of the diffusion time τ_D, shown by the coinciding normalized FCS and FLCS autocorrelation curves (see inset Figure 3.2C).

3.2.3 Z-Scan Fluorescence Lifetime Correlation Spectroscopy

In case of free three-dimensional diffusion (see Section 3.2.1) determination of diffusion constants D from τ_D requires a previous external calibration of the confocal volume V_0. This is usually performed in a solution of a reference fluorophore of known D. In addition to the error sources introduced in Section 3.2.2, this external calibration of V_0 introduces further deviations to the FCS determination of D and N.

For FCS/FLCS measurements on planar samples of negligible thickness compared to w_z, such as SLBs, the most dominant source of artifacts is the irreproducible axial positioning with respect to the waist of the focus along the z-axis[14]. If the sample plane does not coincide with the waist of the focus, areas with radii larger than w_0 are illuminated due to the divergence of the laser beam, which in turn leads to higher values for τ_D and N (see Figure 3.3).

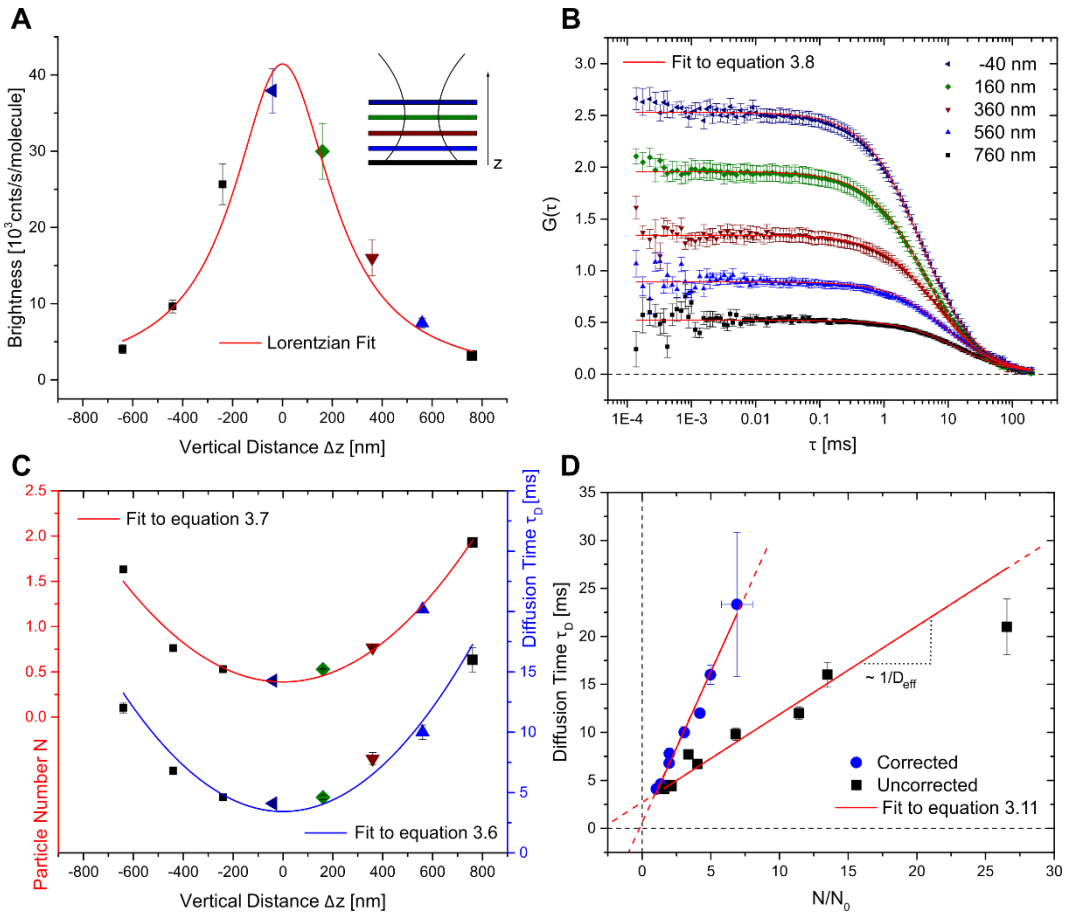

Figure 3.3: Principle of z-scan fluorescence lifetime correlation spectroscopy (FLCS). If the sample plane does not coincide with the waist of the focus, areas with radii larger than w_0 are illuminated due to the divergence of the laser beam (inset of **A.** Note: Colored sample plane positions correspond to the colored data points in **A**, **B** and **C**). Therefore, the brightness drops (**A**) and the apparent N and τ_D increase (**B** and **C**) with increasing distance Δz between the beam waist and a SLB containing Rh PE tracers. This leads to an overestimation of D_{eff} for the case of non-lifetime corrected ACFs along the z-axis (***D***). **A**, Fluorophore brightness in dependence of the distance Δz between the beam waist and the SLB. The profile of a focused laser beam was shown to follow a Lorentz distribution[11]. This translates into a Lorentzian profile of fluorophore brightness along the z-axis, since the probability of emitting a fluorescence photon is proportional to the intensity of the exciting laser beam (which drops proportional to $w(\Delta z)^2$). This dependence is used to find the true position of the sample plane with the maximum brightness at $\Delta z = 0$. **B**, FLCS ACFs measured at different distances Δz. The smaller the illumination area the fewer fluorophore are excited and the higher is the amplitude of the ACFs. $N(\Delta z)$ and $\tau_D(\Delta z)$ are obtained by fits to Equation (3.8) with T = 0. **C**, $N(\Delta z)$ and $\tau_D(\Delta z)$ follow a parabolic dependence. Fits to Equation (3.6) and (3.7) result in the parameters D, c_s and w_0 (here w_0 = 255 ± 11 nm, c_s = 3.15 ± 0.13 pmol m^{-2} and D = 4.72 ± 0.24 µm^{2}s^{-1} for λ = 530 nm). **D**, FCS diffusion law. Although τ_D is not affected by lifetime correction for a single ACF (see Figure 3.2C) the error in particle estimation N from uncorrected ACFs propagates into the determination of D_{eff} (see Equation 3.11; for the corrected curves shown in (**B**) D_{eff} = 5.13 ± 0.37 µm^{2}s^{-1} and $t_0 \approx 0$. For the uncorrected case (ACFs not shown), D_{eff} = 17.86 ± 2.30 µm^{2}s^{-1} and t_0 = 2.68 ± 0.31 ms. Note: Literature value of Rh PE diffusion in DOPC SLBs formed on mica is 4.0 ± 0.5 µm^{2}s^{-1} ref.[15]).

Here, z-scans are applied to overcome this problem in a calibration free manner. The principle of z-scans is again depicted by means of a SLB containing traces of fluorescently labelled lipids (see Figure 3.3 A-C). Autocorrelation functions *G(τ)* are sequentially measured at different positions of the SLB along the optical axis *z*. Assuming a Lorentzian profile of the effective confocal volume along *z* [ref. 7], the diffusion time τ_D and average particle number *N* exhibit a quadratic dependence on the distance between the SLB and the beam waist *Δz*,

$$\tau_D(\Delta z) = \frac{{w_0}^2}{4D}\left(1 + \frac{\lambda^2 \Delta z^2}{\pi^2 {w_0}^4}\right) \quad (3.6)$$

and

$$N(\Delta z) = \pi c_S {w_0}^2 \left(1 + \frac{\lambda^2 \Delta z^2}{\pi^2 {w_0}^4}\right) \quad (3.7)$$

with *λ* the wavelength of the excitation light in the medium and c_s the local surface concentration of the diffusing fluorescently labelled lipids[16].

The fit model for the three-dimensional diffusion (see Equation 3.2) needs to be adjusted to describe the autocorrelation acquired from the two-dimensional diffusing lipids. The fit model for the simple case of single-component, two-dimensional Brownian motion including triplet states kinetics is given by[16]

$$G(\tau)_{2D} = \underbrace{\frac{(1-T+Te^{-\frac{\tau}{\tau_T}})}{(1-T)}}_{G(\tau)_{kinetics}} \underbrace{\frac{1}{N}\frac{1}{1+(\frac{\tau}{\tau_D})}}_{G(\tau)_{2D\ motion}} \quad (3.8)$$

Accordingly, the fit model for two-dimensional diffusion of multiple non-interacting species can be written (compare with the three-dimensional case in Equation 3.3)

$$G(\tau)_{2D,Multi} = \sum_{i=1}^{M} F_i\, G(\tau)_{i,2D} \quad (3.9)$$

Parabolic fits with Equation (3.6) and (3.7) to $\tau_D(\Delta z)$ and $N(\Delta z)$ (acquired by fits of Equation 3.8 or 3.9 to autocorrelation functions obtained at different positions *Δz*) then yield the desired parameters *D*, c_s and w_0.

Besides being a calibration free method to determine the parameters D, c_s and w_0, Z-scans provide additional information on the underlying type of diffusion by analyzing the dependence of τ_D on the radius of the illumination area $w(\Delta z)$ at the SLB. For lateral diffusion this dependency - the so called FCS diffusion law - is given by[17]

$$\tau_D(\Delta z) = t_0 + \frac{w(\Delta z)^2}{4D_{eff}} \quad (3.10)$$

The intercept t_0 equals 0 for free Brownian motion, but is non-zero when diffusion is hindered ($t_0 > 0$ for permeable microdomains) or guided ($t_0 < 0$ within meshworks)[17] and the effective diffusion coefficient D_{eff} is then different from D measured at a single value $w(\Delta z)$. Finally, combining Equation (3.10) with Equations (3.6) and (3.7) results in[18]

$$\tau_D(\Delta z) = t_0 + \frac{{w_0}^2}{4D_{eff}}\left(\frac{N(\Delta z)}{N_0}\right) \quad (3.11)$$

with N_0 the average number of particles in the beam waist cross-section (πw_0^2) obtained with Equation (3.7). Fits of this z-scan FCS diffusion law to $\tau_D(\Delta z)$ and $N(\Delta z)$ from ACFs with and without lifetime correction show how the error in the particle number N estimation propagates into the determination of D_{eff} (see Figure 3.3D), although τ_D from a single ACF remains unaffected by the correction (see inset Figure 3.2C). The previously introduced FLCS is hence crucial for the unbiased application of the FCS diffusion law (Equation 3.11) as well as the proper assessment of w_0 from fitting Equation 3.7 to $N(\Delta z)$.

Due to intermolecular interactions, lateral self-diffusion in crowded environments (like SLBs containing interacting obstacles or polymer brushes) is likely to be hindered and results in a nonlinear diffusion law according to which the mean-square-displacement $\langle x(t)^2 \rangle$ is proportional to a power law $\sim t^\alpha$ ($0 < \alpha < 1$)[19]. The mean-square-displacement which describes free two-dimensional Brownian motion ($\langle x(t)^2 \rangle = 4Dt$) is thereby modified by introducing an anomalous diffusion exponent α such that

$$w(\Delta z)^2 = 4\Gamma\tau_D(\Delta z)^\alpha \quad (3.12)$$

with Γ an anomalous diffusion constant of unit $[\Gamma] = m^2 s^{-\alpha}$.

The deviation from free diffusion also manifests in a different shape of $G(\tau)$ and the anomalous exponent has to be introduced in Equations (3.2), (3.3), (3.7) and (3.8) by replacing the term (τ/τ_D) by $(\tau/\tau_D)^{\alpha}$. Single ACFs hence not only contain information about the diffusion time but also give insight into the molecular crowding within the length scale of w_0.

3.2.4 Fluorescence Lifetime Cross-Correlation Spectroscopy

So far, the introduced FCS and FLCS measurements in Sections 3.2.1 and 3.2.2 are based on the excitation of a single fluorescent species with one distinct laser line measured with a single color channel (one detector), *i.e.* single-colored.

Fluorescence lifetime cross-correlation spectroscopy (FLCCS) is essentially the extension of the FLCS procedure utilizing two spectrally separated fluorescent species excited with two distinct laser lines and measured in two color channels (two detectors; see Figure 3.4A), *i.e.* dual-color; or two fluorescence species with overlapping fluorescence spectra but different lifetimes, excited by the same laser line and measured with a single color channel. If the two fluorescence species move together through the confocal volume (or the illumination cross-section) their respective fluorescence intensity fluctuations will coincide, *i.e.* cross-correlate. Consequently, FLCCS provides a sensitive means to measure the molecular interactions between differently labelled fluorescent species.

Standard FCCS often suffers from cross talk into the wrong color channel leading to false positive cross-correlation[20]. In dual-color FLCCS, when two laser lines are used, usage of alternating laser pulses can circumvent this problem. This so called pulse interleaved excitation (PIE) together with a time-gated detection (detection for each color channel synchronized with the respective laser pulses) allows one to completely separate photons originating from different fluorescence species (see Figure 3.4B)[21]. Additionally, lifetime filtering of the intensity fluctuation recorded individually by the two detectors *a* and *b* ensures the elimination of artifacts from any other source (Figure 3.4C; see also Section 3.2.2) and the lifetime corrected cross-correlation function (CCF; compare with Equation 3.5) is defined as

$$G_{a,b}(\tau)^{(S_{a,b})} = \frac{<\sum_j f_{a,j}^{(S_a)} A_{a,j}(t) \sum_j f_{b,j}^{(S_b)} A_{b,j}(t+\tau)>}{<\sum_j f_{a,j}^{(S_a)} A_{a,j}(t)><\sum_j f_{b,j}^{(S_b)} A_{b,j}(t)>} \qquad (3.13)$$

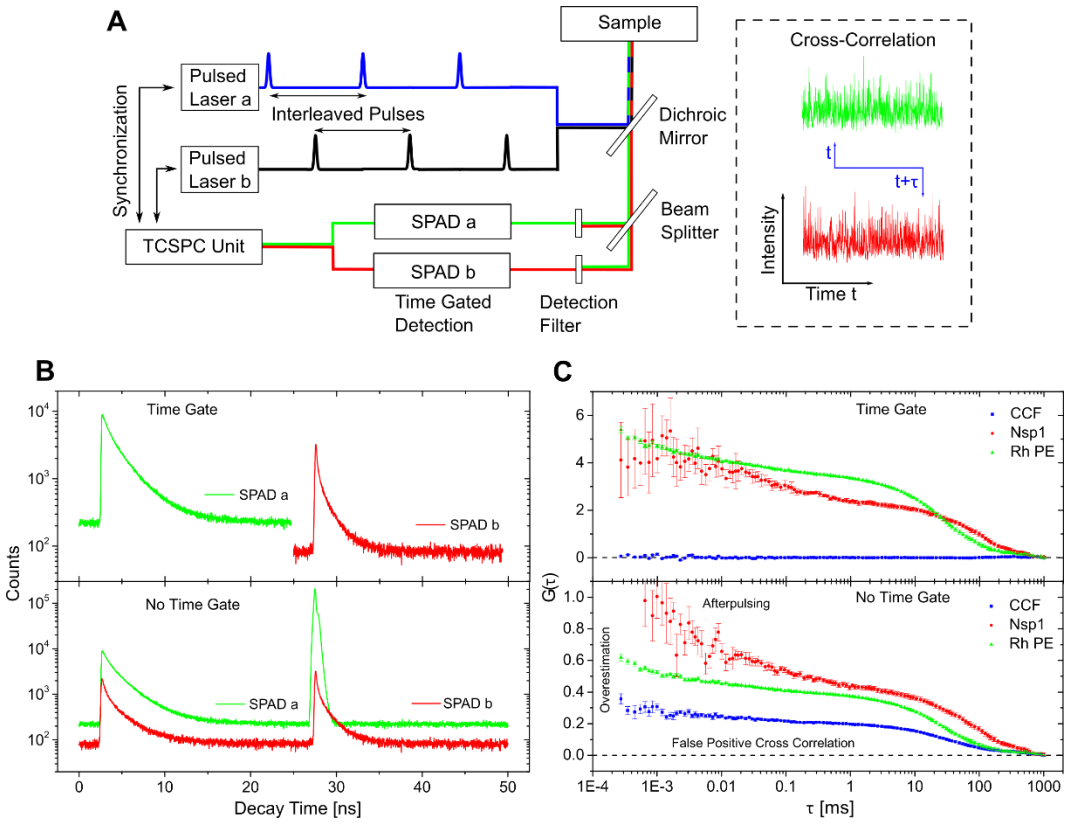

Figure 3.4: Principle of dual-color, time gated, pulsed interleaved excitation (PIE) fluorescence lifetime cross-correlation spectroscopy (FLCCS). **A**, Schematics of dual-color PIE FLCCS. Two pulsed lasers *a* and *b* are synchronized such that their phase shift is equal to half of their pulse intervals (here 20 MHz or 50 ns). The fluorescence signal from a sample containing two fluorophores with different colors is spectrally filtered and detected by the respective SPAD *a* and *b*. The time gates of the SPADs are then again synchronized with their associated pulsed laser, *i.e* SPAD *a* is open for 0 – 25 ns and closed for the remaining 25 ns until Pulsed Laser *a* emits the next pulse (and *vice versa* for SPAD *b* and Pulsed Laser *b*) **B**, Comparison between lifetime decays with and without time gating. Time gating (top) removes all cross talk signal obtained in non-time gated acquisition (bottom). **C**, Comparison between dual-color time gated PIE FLCCS (top) and dual-color PIE FCCS (bottom). Time gating reveals that the measured cross-correlation between Rh PE tracers within an SLB and Nsp1FF12 labelled with Alexa 647 (Nsp1) attached to the SLB originates entirely from cross talk between the two color channels. Time gating also enables an appropriate lifetime correction for both channels, which in turn leads to the suppression of afterpulsing and particle overestimation (see Section 3.2.2).

The amplitude of the cross-correlation curve is a measure of binding and dynamic colocalization between the two fluorescent species[15]. The false-positive cross-correlation from cross talk obtained by PIE FCCS on SLBs therefore implies artificial binding (Figure 3.4C). In the case of dual-color time gated PIE FLCCS (hereafter simply called dual-color FLCCS), where all cross talk is removed, mismatch in the overlap of the illumination areas of the two laser lines, binding stochiometries other than 1:1 as well as non-uniformly labelling complicate a proper interpretation of an apparent CCF[22].

3.3 Z-Scan of Rhodamine Labelled Supported Lipid Bilayers

FLCS z-scans were first performed on SLBs formed with varying contents of Rh PE tracers. Sample homogeneity was tested by multiple z-scans on grids of 2x2 points 3 µm separated from each other. Independent of the tested concentration ($c_{s,\,Rh\,PE}$ = 1 – 600 pmol m^{-2}), Rh PE autocorrelation curves (see Figure 3.3B) fit to a single-component, two-dimensional Brownian motion model (Equation 3.8 with the triplet fraction T = 0 and anomalous diffusion exponent α = 1). All τ_D to N/N_0 dependencies from z-scans on SLBs with various Rh PE concentrations fall on a single line as shown in Figure 3.5A (N = 8, n = 59). A fit to the linear FCS diffusion law (Equation 3.11) then results in t_0 = 2.1 ± 0.71 ms and $w_0^2/4D_{eff}$ = 2.4 ± 0.23 ms. The effective beam waist radius w_0 was determined for each sample individually by applying a fit of the parabolic Equations (3.7) to the respective $N(\Delta z)$ (compare with Figure 3.3C) and averaged (248 ± 38 nm). Solving for D_{eff}, leads to an effective diffusion constant for Rh PE tracers of 6.40 ± 1.15 $\mu m^2 s^{-1}$ close to the value (D = 4.72 ± 0.24 $\mu m^2 s^{-1}$) obtained from an individual z-scan (see Figure 3.3). The intercept value t_0 is close to 0, such that next to the ACF fit model (α = 1) also the application of the FCS diffusion law indicates free Brownian motion of the Rh PE within SLBs formed by DOPC, independent of their concentration.

The quality of the correlation curves obtained for a fixed measurement time (here 1 min per ACF) and laser power (here ~ 1 µW) depends on the number of fluorescent particles within the illumination area. The best SNR was acquired for samples with a Rh PE surface concentration of $c_{s,Rh\,PE} \sim 3$ pmol m^{-2} ($N \approx 0.5$) Hence, this concentration was kept constant for subsequent experiments with labelled SLBs.

In accordance with the FRAP experiments presented in Chapter 2, the effect of DGS-NTA(Ni) modified lipids within the lipid layer and the attachment of Nsp1FF12 on the diffusion of Rh PE tracers was investigated next (Figure 3.5B). t_0 (1.9 ± 0.53 ms) and $w_0^2/4D_{eff}$ (2.64 ± 0.23 ms) obtained from z-scans on SLBs with a content of 20% DGS NTA(Ni) (labelled as RhPE & DGS-NTA; N = 2, n = 27) are comparable to the case without DGS NTA(Ni) (black line). The effective diffusion constant (D_{eff} = 5.82 ± 1.03 $\mu m^2 s^{-1}$) does not differ significantly. The discrepancy between the reduction in tracer diffusion due to DGS NTA(Ni) measured with FRAP (see Section 2.3; Rh PE diffusion drops ~ 50 % for a 20% content of DGS NTA(Ni)) likely originates from the different scales of the two techniques. The tracer molecule may perform a free diffusion locally (as measured with FLCS) but exhibit a lower D for larger areas (as observed by FRAP) due to the mobile character of the obstacle.

However, attachment of Nsp1FF12 (labelled as RhPE & DGS-NTA & NTA; N = 3, n = 22) has a substantial influence on the diffusion of the Rh PE tracers within the SLB. After immobilization of Nsp1FF12 on a SLB with a content of 20% DGS NTA(Ni), the intercept t_0 raises to 5.08 ± 1.7 ms and the slope $w_0^2/4D_{eff}$ to 7.46 ± 1.0 ms, which leads to an effective diffusion constant of 2.06 ± 0.42 $\mu m^2 s^{-1}$. This pronounced three-fold reduction in diffusion is indicative for the immobilization (due to the Nsp1FF12 attachment and their intermolecular interactions) of the obstacles (DGS NTA(Ni) linked to individual Nsp1FF12 molecules) since the effect of immobile obstacles is more pronounced than that of mobile ones.

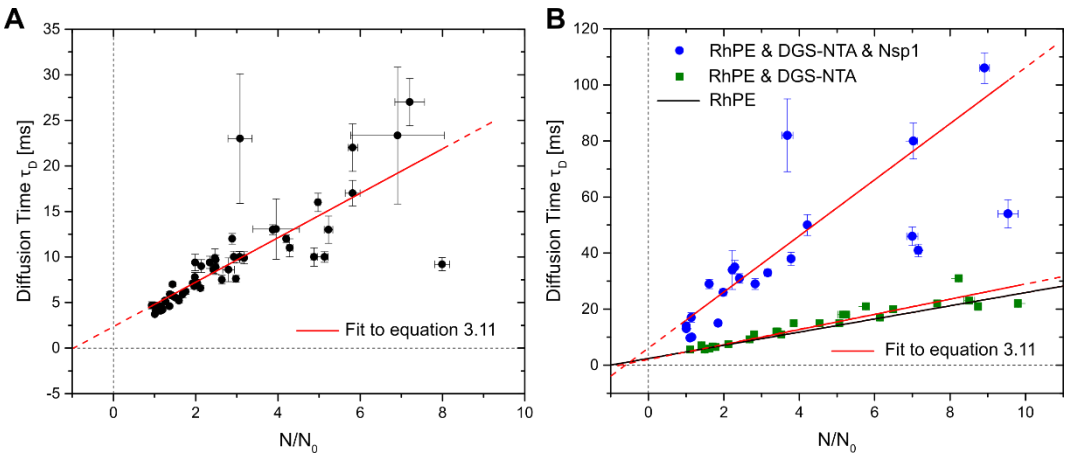

Figure 3.5: Lifetime corrected FCS diffusion law of Rh PE tracers with and without obstacles. **A**, Lateral self-diffusion of Rh PE tracer diffusion in DOPC SLBs is independent of the tracer concentration within a range of 1 – 600 pmol m^{-2}. **B**, Effect of Nsp1FF12 attachment on the Rh PE diffusion. For comparison, fit to the data in (**A**) is included as black line (Rh PE). While the effect of a 20% DGS NTA(Ni) content in the SLB formed by DOPC is neglectable (Rh PE & DGS-NTA), attachment of Nsp1FF12 results in a pronounced reduction of the Rh PE tracer diffusion (RhPE & DGS &Nsp1). The increase in intercept t_0 indicates the formation of microdomains with increased obstacle densities due to the transient formation of Nsp1FF12 aggregates.

The reduction in Rh PE diffusion is accompanied by a shift of the intercept t_0 towards more positive values. The Nsp1FF12 is therefore likely to induce microdomains in the SLB with an increased obstacle density, *i.e.* Nsp1FF12 forms transient aggregates (see also Section 2.4). Furthermore, dual-color FLCCS reveals that there is no correlation between the translational diffusion of Rh PE tracers within an SLB and labelled Nsp1FF12 attached to the SLB (see Figure 3.4C), *i.e.* DGS – Nsp1FF12 complexes act as non-interacting obstacles for the diffusion of Rh PE tracers.

3.4 Karyopherinβ1 Interacting with Immobilized Nsp1FF12 Layers

Interaction between Kapβ1 with Nsp1FF12 layers under the exposure of different Kapβ1 background concentrations in solution was investigated by dual-color FLCCS. To do so, Nsp1FF12 layers attached to SLBs containing Rh PE tracers were exposed to a partially labelled 1nM Kapβ1 solution followed by thorough rinsing (see Section 3.6.2 for details). The remaining labelled Kapβ1 molecules within the Nsp1FF12 layer are hence strongly bound, $K_d \sim 10^{-7}$ M (see Section 2.6). Dual-color z-scans then enable to obtain the dependence of the fluorophore brightness on the beam waist-to-sample plane distance Δz (see Figure 3.3A) for both channels, whereas the Lorentzian profile of the Rh PE tracers is later used as an intrinsic ruler (see below).

The subsequently employed experimental procedure is reminiscent of classical SPR experiments (see Section 2.6). Two measurements for each applied concentration (1 nM – 10 µM) of unlabelled Kapβ1 have been performed: One after an association phase of 10 min and one after a dissociation phase of 20 min. In other words, concentration after the association phase c_{ass} refers to the situation where the exchange of Kapβ1 molecules between the layer and the solution is at steady state and the concentration after the dissociation phase c_{diss} refers to the situation where all weakly bound molecules dissociated from the layer subsequent to the exposure to c_{ass} and only a "long-lived" Kapβ1 fraction remains in the FG layer. Each dual-color FLCCS measurement then consists of the acquisition at two different points for 5 – 8 min.

Representative ACFs and CCF for Rh PE and Kapβ1 obtained at c_{ass} = 1nM are shown in Figure 3.6A. Lag times τ were limited to 10^{-4} – 10^{0} s, since other effects than translational diffusion are not in the scope of the experiments and triplet state can be excluded for this time range. While multi-component two-dimensional fits (Equation 3.9 with T = 0) led to unphysical solutions, Rh PE and Kapβ1 autocorrelation curves are well described by a single-component, two-dimensional hindered motion model (Equation 3.8 with anomalous exponent $\alpha \leq 1$; see Figure 3.6A). The brightness signal of Rh PE is then used to determine the true illumination area radius $w(\Delta z)$ by means of the previously acquired brightness-to-Δz dependency. This allows one to utilize the apparent diffusion times $\tau_D(\Delta z)$ and values for the anomalous exponent α from the fits to the ACFs to calculate the anomalous diffusion constant Γ (see Equation 3.12).

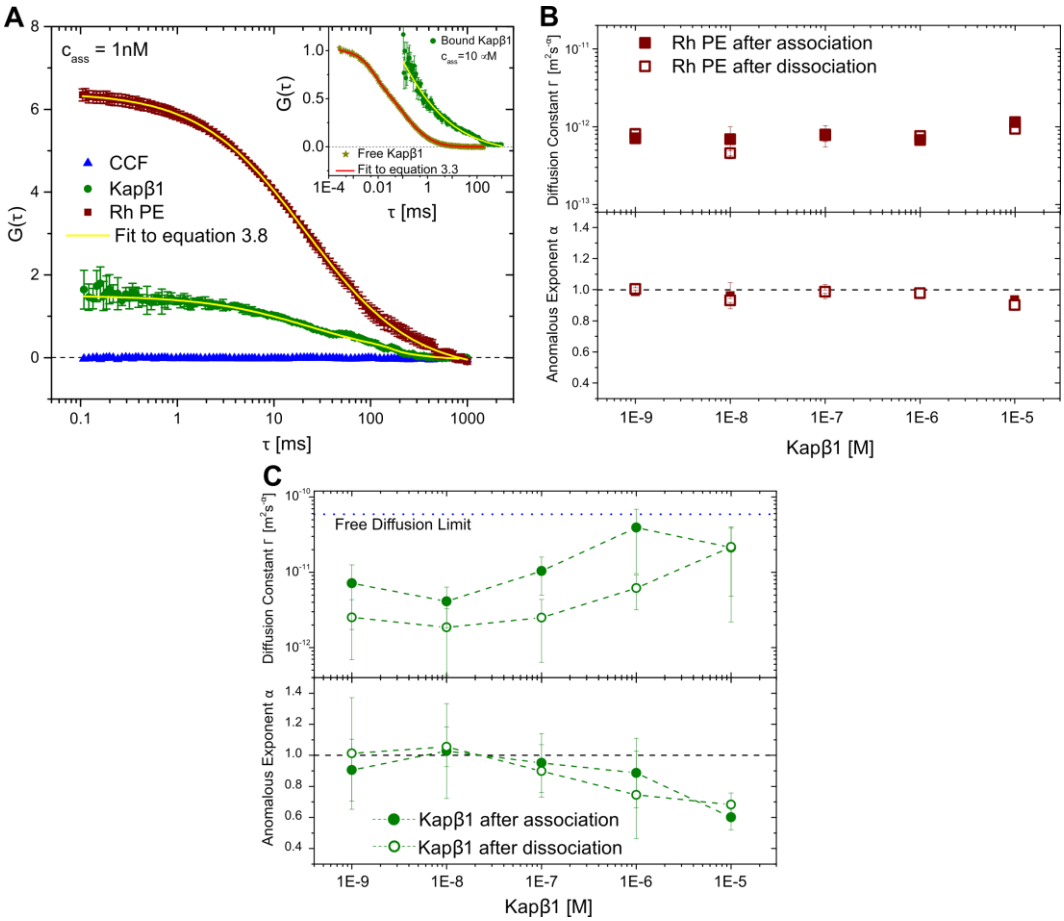

Figure 3.6: Influence of Karyopherinβ1 concentration on its interaction with Nsp1FF12 layers investigated by dual-color FLCCS. **A**, Comparison of representative ACFs of Rh PE and Kapβ1 acquired at an association concentration of 1nM. ACFs are well fitted by a single component model of hindered motion (Equation 3.8 with T = 0 and $\alpha \leq 1$). Rh PE and Kapβ1 do not associate as the CCF is 0 for all measured concentrations (1 nM -10 µM). Inset: Correlation characteristics of bound and free Kapβ1 differ fundamentally (here c_{ass} = 10 µM). The ACF of free Kapβ1 (D_{free} = 57 ± 9 µm^{2}s^{-1}) was fitted by a three-dimensional multi-component model (Equation 3.3, M = 2, T = 0 and α = 1) to account for free Alexa dye. **B**, The anomalous diffusion constant Γ (top) as well as the anomalous exponent α (bottom) of Rh PE tracers remain unaffected by the concentration of Kapβ1 within the layer and in solution. **C**, The anomalous diffusion constant Γ (top) of layer bound Kapβ1 increases regardless of the higher occupancy within the Nsp1FF12 layer as indicated by the simultaneous decay of the anomalous exponent α (bottom; error bars are the SD over N = 2, n = 6).

The influence of the concentration of unlabelled Kapβ1 after the association c_{ass} and dissociation c_{diss} phase on Γ and the α of Rh PE and of Nsp1FF12 layer bound labelled Kapβ1 is shown in the Figures 3.6B and D. The slightly non-normal motion of Rh PE remains largely unaffected by the presence of additional Kapβ1 in the layer (Γ between 0.5 -1 µm^{2}s$^{-\alpha}$ and $\alpha \approx 0.95$ for all concentrations c_{ass} and c_{diss}; see Figure 3B). This is to some extent also reflected by the absence of any cross-correlation between Rh PE and the layer-bound Kapβ1 for all measured concentrations (see Figure 3.6A for the representative case of c_{ass} = 1 nM).

Contrarily, the anomalous diffusion constant Γ and the anomalous exponent α for the layer-bound Kapβ1 (Figure 3.6C) both exhibit a strong dependence on the concentration levels c_{ass} and c_{diss} (see also Table 3.1). Surprisingly, Γ increases with higher concentrations although the declining α values indicate enhanced molecular crowding. Since this trend is apparent for both c_{ass} and c_{diss} it is clear that the decrease of α originates exclusively from the increased occupancy of Kapβ1 within the Nsp1FF12 layer. Interpreting this dependency is however cumbersome due to the α-dependent units of Γ ($[\Gamma] = 1\ \mu m^2 s^{-\alpha}$).

More instructive is the assessment of an apparent, time-dependent (and hence length scale dependent) diffusion constant $D(t) = \Gamma t^{\alpha-1}$ resulting from every pair (Γ, α). The focus lies thereby on timescales on the order of the reported Kapβ1 facilitated translocation times of cargo through the NPC (~ 5 ms, see Section 1.2.2). Moreover, is the lateral displacement of Kapβ1 related to the relevant dimension by a normalization of the mean square displacement $\langle x(t)^2 \rangle = 4D(t)t$ at 5 ms to the inner surface area of a NPC (modelled by the surface of a cylinder of 100 nm height and 50 nm width). Such normalized MSDs calculated from average values of Γ and α for c_{ass} and c_{diss} are presented in Table 3.1. It is evident that even the long-lived Kapβ1 fraction is highly mobile within the Nsp1FF12 layer, *e.g.* a Kapβ1 molecule at c_{diss} = 100 nM (the range of the K_d of long-living Kapβ1) has the capacity to explore an area equivalent of ~4 NPCs within 5 ms. Counterintuitively, the time-dependent lateral displacement within the layer further increases with increasing layer occupancy at c_{diss} = 10 µM to an area equivalent of ~20 NPCs. In other words, although the overall motion of Kapβ1 is strongly hindered ($\alpha_{diss} \approx 0.7$), Kapβ1 movement on the millisecond timescale accessed by the present dual-color FLCCS measurements appears to be boosted.

The similar behavior is observed under steady state conditions c_{ass}. Relative to the case of long-lived Kapβ1, displacement expands with the presence of a weakly bound fraction. Comparison between the shapes of ACFs of Kapβ1 obtained at c_{ass} = 10 µM and freely diffusing Kapβ1 reveals the qualitative differences between free and layer bound Kapβ1 motion (inset Figure 3.6A).

Table 3.1: Concetration dependence of the anomalous diffusion constant Γ and anomalous exponent α of layer-bound Kapβ1.

Kapβ1 [M]	Γ_{ass} [$\mu m^2 s^{-\alpha}$]	α_{ass}	***MSD/NPC***
10^{-9}	7.15 ± 5.41	0.90 ± 0.19	9.7
10^{-8}	4.10 ± 2.28	1.02 ± 0.30	6.7
10^{-7}	10.42 ± 5.47	0.95 ± 0.18	15.3
10^{-6}	39.23 ± 29.60	0.88 ± 0.22	51.5
10^{-5}	21.23 ± 19.04	0.60 ± 0.08	17.8
Kapβ1 [M]	Γ_{diss} [$\mu m^2 s^{-\alpha}$]	α_{diss}	***MSD/NPC***
10^{-9}	2.51 ± 1.81	1.01 ± 0.35	4.1
10^{-8}	1.86 ± 1.43	1.05 ± 0.12	3.2
10^{-7}	2.49 ± 1.85	0.89 ± 0.17	3.3
10^{-6}	6.17 ± 2.98	0.74 ± 0.28	6.5
10^{-5}	21.16 ± 16.81	0.68 ± 0.07	20.1

3.5 Discussion and Conclusion

The present study reveals some remarkable features of Kapβ1 bound to FG domain layers formed on SLBs:

First, Kapβ1 exhibits a surprisingly high in-layer mobility although the multivalent character of the FG - Kapβ1 interaction invokes binding affinities in the nanomolar range ($K_d \sim 10^{-7}$ M). The mean square displacement for Kapβ1 concentrations of 100 nM – in the range of the K_d of long-lived Kapβ1 - would already suffice to explore the entire inner wall of a NPC multiple times within ~ 5 ms (the reported time for Kapβ1 mediated cargo translocation; see Section 1.2.2).

Second, for low layer occupancies (c_{ass}, $c_{diss} \leq 100$ nM) the diffusion seems not to differ significantly from free Brownian motion (α_{ass}, $\alpha_{diss} \sim 1$), portending extremely week and short-lived interactions between the FG domains and Kapβ1.

Third, the apparent Kapβ1 diffusion constant increases with increasing layer occupancy. The decline of the anomalous exponent α for increasing concentrations (down to 0.6 for 10 µM) is in fact the manifestation of a hindered type of diffusion, but does not infer a lack of mobility within the relevant time of cargo translocation. In other words, Kapβ1 maintains fast displacement regardless of the enhanced molecular crowding within the FG domain layer, a prerequisite to enable highly parallelized transport through the NPC. Kapβ1 concentration therefore seems to regulate the speed and the level of parallelization of NCT. This behavior is likely owned to the interplay of Kapβ1 - Kapβ1 repulsion, competition for FG motives and conformational changes of the FG Nup layer triggered by high Kapβ1 occupancy.

3.6 Materials and Methods

3.6.1 Liposome Composition

Liposomes were either formed by 1,2-dioleoyl-*sn*-glycero-3-phosphocholine (DOPC) and labelled with a varying amount of 0.06 - 6 ppm 1,2-dioleoyl-*sn*-glycero-3-phosphoethanolamine-N-(lissamine rhodamine B sulfonyl) (ammonium salt) (Rh PE), by 80 %mol DOPC and 20 %mol 1,2-dioleoyl-*sn*-glycero-3-[(N-(5-amino-1-carboxypentyl)iminodiacetic acid)succinyl] (nickel salt) (DGS NTA(Ni)) or by 80 %mol DOPC and 20 %mol DGS NTA(Ni) labelled with a stable amount of 0.6 ppm Rh PE. Liposome formation and characterization is similar to the protocol found in Section 2.8.1.

3.6.2 Preparation of the Sample Chamber

Homemade PDMS (10:1 Sylgard(R) 184, Dow Corning) cells containing two connected reservoirs (80 µl) were covalently attached to borosilicate coverslips (24 x 60 mm, Nr. 1, Menzel Glass) *via* O_2 plasma activation (13.56 MHz, 50 W, 5 sccm, 30 s, Femto, DienerElectronics) and post-baking (10 min at 120 °C). The coverslip surface was hydrophilized immediately before applying filtered (0.22 µm, TRP) PBS solution (pH 7.2, 150 mM NaCl, Gibko) to the reservoirs by exposure to a second O_2 plasma treatment (13.56 MHz, 12.5 W, 5 sccm, 5 min). Subsequently, the PBS was exchanged with liposome solution to permit single lipid bilayer (SLB) formation by spontaneous spreading on the coverslip surface for 10 min. The entire cell has been immersed in a large volume of fresh PBS buffer for 45 – 60 min under constant shaking to remove remaining, non-ruptured SUVs.

Prior to FLCCS measurements between Rh PE and Nsp1FF12, SLBs containing 0.6 ppm Rh PE and 20% DGS NTA(Ni) were functionalized by incubation overnight at 4 °C with mixtures of fluorescently labelled (Alexa Fluor647 C_2 maleimide) and non-fluorescent (1:150000) Nsp1FF12 fragments in PBS *via* NTA(Ni) – His_6 interaction. Excess Nsp1FF12 fragments were removed twice by immersion of the entire cell in a large volume of fresh PBS buffer. First for 45 – 60 min under constant shaking at room temperature and then overnight at 4°C.

Prior to FLCCS measurements between Rh PE and Kapβ1, SLBs containing 0.6 ppm Rh PE and 20% DGS NTA(Ni) were functionalized by incubation overnight at 4 °C with non-fluorescent Nsp1FF12 fragments in PBS *via* NTA(Ni) – His_6 interaction. Again, excess Nsp1FF12 fragments were removed twice. The resulting Nsp1FF12 layer was subsequently incubated by a 1nM mixture of fluorescently labelled (Alexa Fluor647 NHS ester) and non-fluorescent (1:10) of Kapβ1 for 1 h at RT and

non-bound Kapβ1 afterwards again removed by immersion of the entire cell in a large volume of fresh PBS buffer for 3 h at room temperature or overnight at 4°C under constant shaking. Note: The fact that after this rinsing step Kapβ1 molecules remain layer-bound is indicative for very low $K_D < 10^{-7}$ M.

3.6.3 Kapaβ1 Preparation

The expression and purification procedures for human Kapβ1 can be found in Section 2.8.3. For FLCCS experiments, Kapβ1 was labelled with Alexa Fluor647 carboxylic acid, succinimidyl ester (Alexa Fluor647 NHS ester) in filtered PBS buffer using the standard labelling procedure for amine-reactive probes (Invitrogen Protocols). Conjugation efficiency was determined by spectrophotometry (Nanodrop 2000).

3.6.4 Nsp1FF12 Preparation

The expression and purification procedures for yeast Nsp1 can be found in Section 2.8.4. For FLCCS experiments with Kapβ1, Nsp1FF12 was labelled with Alexa Fluor647 carboxylic acid, succinimidyl ester (Alexa Fluor647 NHS ester) in filtered PBS buffer using the standard labelling procedure for amine-reactive probes (Invitrogen Protocols). Conjugation efficiency was determined by spectrophotometry (Nanodrop 2000).

3.6.5 PIE FLCS/FLCCS Procedure

FLCS and time gated PIE FLCCS measurements were performed on a Olympus IX73 inverted microscope stand equipped with a 1.2 NA water immersion 60x superapochromat objective (UplaSApo, Olympus) and appropriate emission and excitation band pass filters (Semrock and AHF). Two pulsed diode lasers (LDH-P-FA-530 and LDH-D-C-640, PicoQuant) were driven at 40 MHz for FLCS or at 20 MHz for PIE FLCCS (Sepia II, PicoQuant). Depending on the experiment, photon detection was performed by either one or two SPADs (SPCM CD3516H, Excelitas) and picosecond histograms acquired by a TCSPC unit (16 ps resolution, HydraHarp 400). Laser powers were set between 1 – 10 µW, measurement times between 30 s – 10 min and correlation integration times from 0.2 s to 10 s. Measurements in solution were performed 20 µm away from the coverslip with a previously calibrated confocal volume. Z-scans at the coverslip interface were acquired with a step size of 200 nm on grids of 1x1 or 2x2 points (3 µm separated from each other). Correlation curves were analyzed by SymphoTime 64 and Quickfit. The considered models where described in Section (3.2).

3.7 References

1. Elson, E. L. & Magde, D. Fluorescence correlation spectroscopy. I. Conceptual basis and theory. *Biopolymers* **13,** 1–27 (1974).
2. Magde, D., Elson, E. & Webb, W. W. Thermodynamic Fluctuations in a Reacting System—Measurement by Fluorescence Correlation Spectroscopy. *Phys. Rev. Lett.* **29,** 705–708 (1972).
3. Magde, D., Elson, E. L. & Webb, W. W. Fluorescence correlation spectroscopy. II. An experimental realization. *Biopolymers* **13,** 29–61 (1974).
4. Rigler, R., Mets, Ü., Widengren, J. & Kask, P. Fluorescence correlation spectroscopy with high count rate and low background: analysis of translational diffusion. *Eur. Biophys. J.* **22,** 169–175 (1993).
5. Kapusta, P. Absolute Diffusion Coefficients: Compilation of Reference Data for FCS Calibration. at Gmbh, PicoQuant (2010). <https://www.picoquant.com/images/uploads/page/files/7353/appnote_diffusioncoefficients.pdf>
6. Sýkora, J. *et al.* Exploring fluorescence antibunching in solution to determine the stoichiometry of molecular complexes. *Anal. Chem.* **79,** 4040–4049 (2007).
7. Widengren, J., Me, U. & Rigler, R. Fluorescence Correlation Spectroscopy of Triplet States in Solution: A Theoretical and Experimental Study. *J. Phys. Chem* **99,** 13368–13379 (1995).
8. Bacia, K., Haustein, E. & Schwille, P. Fluorescence correlation spectroscopy: Principles and applications. *Cold Spring Harb. Protoc.* **2014,** 709–725 (2014).
9. Krichevsky, O. Fluorescence correlation spectroscopy : the technique. *Reports Prog. Phys.* **65,** 251–297 (2002).
10. Kapusta, P., Macháň, R., Benda, A. & Hof, M. Fluorescence Lifetime Correlation Spectroscopy (FLCS): Concepts, Applications and Outlook. *Int. J. Mol. Sci.* **13,** 12890–12910 (2012).
11. Enderlein, J. & Gregor, I. Using fluorescence lifetime for discriminating detector afterpulsing in fluorescence-correlation spectroscopy. *Rev. Sci. Instrum.* **76,** 33102-1–33102-5 (2005).
12. Becker, W. Advanced time-correlated single photon counting techniques. *Springer Series in Chemical Physics* **81,** Heidelberg Berlin (2005).
13. Kapusta, P., Wahl, M., Benda, A., Hof, M. & Enderlein, J. Fluorescence Lifetime Correlation Spectroscopy. *J Fluoresc* **17,** 43–48 (2007).

14. Benda, A. *et al.* How to determine diffusion coefficients in planar phospholipid systems by confocal fluorescence correlation spectroscopy. *Langmuir* **19,** 4120–4126 (2003).

15. Miszta, A. *et al.* Combination of ellipsometry, laser scanning microscopy and Z-scan fluorescence correlation spectroscopy elucidating interaction of cryptdin-4 with supported phospholipid bilayers. *J. Pept. Sci.* **14,** 503–509 (2008).

16. Macháň, R. & Hof, M. Recent developments in fluorescence correlation spectroscopy for diffusion measurements in planar lipid membranes. *International Journal of Molecular Sciences* **11,** 427–457 (2010).

17. Wawrezinieck, L., Rigneault, H., Marguet, D. & Lenne, P.-F. Fluorescence correlation spectroscopy diffusion laws to probe the submicron cell membrane organization. *Biophys. J.* **89,** 4029–4042 (2005).

18. Humpolíčková, J. *et al.* Probing Diffusion Laws within Cellular Membranes by Z-Scan Fluorescence Correlation Spectroscopy. *Biophys. J.* **91,** 23–25 (2006).

19. Banks, D. S. & Fradin, C. Anomalous diffusion of proteins due to molecular crowding. *Biophys. J.* **89,** 2960–2971 (2005).

20. Bacia, K. & Schwille, P. Practical guidelines for dual-color fluorescence cross-correlation spectroscopy. *Nat. Protoc.* **2,** 2842–2856 (2007).

21. Müller, B. K., Zaychikov, E., Bräuchle, C. & Lamb, D. C. Pulsed Interleaved Excitation. *Biophys. J.* **89,** 3508–3522 (2005).

22. Kim, S. A., Heinze, K. G., Bacia, K., Waxham, M. N. & Schwille, P. Two-Photon Cross-Correlation Analysis of Intracellular Reactions with Variable Stoichiometry. *Biophys. J.* **88,** 4319–4336 (2005).

Chapter 4

Fabrication and Characterization of Glass Nanocapillaries

Parts of this chapter have been published as
Zweifel, L. P., Shorubalko, I. & Lim, R. Y. H. Helium Scanning Transmission Ion Microscopy and Electrical Characterization of Glass Nanocapillaries with Reproducible Tip Geometries. *ACS Nano* **10,** 1918–1925 (2016).

4 Fabrication and Characterization of Glass Nanocapillaries

4.1 Introduction

Solid state nanopores are versatile biophysical tools for label-free single-molecule detection in aqueous solutions[1]. Similar to the macroscopic Coulter counter technique, two salt solution containing reservoirs are connected *via* a single nanopore, across from which an electrical potential is applied. The potential difference between the reservoirs establishes an ionic current that is primarily restricted by the small dimensions of the connecting pore (Figure 4.1A). The ionic current therefore drops upon partial blockage of the pore due to the passage of electrokinetically driven biomolecules from one reservoir to the other. This allows for the identification of nucleic acids[2] and proteins[3] by monitoring the length, amplitude and frequency of these drops in ionic current in various nanopore systems.

Some of the most widely used methods to produce nanopores of differing geometries within membranes of different materials include single ion-track etching, ion beam sculpting as well as focused ion or electron beam milling. Single ion-track etched PET films cover the widest range of different geometries and have been used to fabricate conical[4], cylindrical[5], hourglass[6], cigar[7] and bullet-like[8] shaped nanopores. On the other hand, ion beam sculpting of silicon nitride membranes leads to bowl shapes[9], while nanopores directly milled by a focused ion[10] or electron[11] beam resemble an hourglass shape. Arguably, these fabrication methods can be time consuming and technically demanding. A recent development in nanofabrication therefore seeks to facilitate device production[12].

Of late, glass nanocapillaries (GNCs) fabricated by laser assisted thermal pulling[13] of glass microcapillaries have emerged as a simple and low cost alternative for single molecule detection. Depending on the glass type and pulling parameters, GNC tips with opening diameters from micrometers down to nanometers[14] and opening angles from 5° to 66° are achieved[15]. GNCs have been used to detect folding of λ-phage DNA[13], detection of single protein molecules[16] and protein sensing *via* DNA carriers[17]. GNCs were further able to probe the sizes of different protein molecules[18].

Nonetheless, the insulating nature of glass makes it difficult to characterize GNCs in a non-invasive manner. For instance, the use of scanning electron microscopy (SEM) leads to charging effects and hydrocarbon contamination of the glass

surface[19]. Furthermore heating of the GNC changes its tip geometry[20]. All these effects can greatly influence the current-to-voltage (IV)-characteristics and molecule translocation. Although metal coats can be used for SEM, their presence influences the tip geometry and limits surface functionalization protocols.

Here we show that scanning transmission ion microscopy with Helium ions[21] (HeSTIM), provides a non-invasive means to resolve GNCs with unparalleled accuracy. This is achieved using very low He beam currents, which minimizes unfavorable heating effects omitting the need of metal coatings. Although some contamination occurs due to secondary electron release following He ion bombardment, plasma cleaning effectively removes this contamination such that the GNCs are not altered after HeSTIM imaging. The integrity of the geometrical structure is thereby established by the choice of mild plasma conditions.

Accordingly, HeSTIM allows for an accurate non-destructive deduction of inner and outer geometric properties of the GNC tips like inner opening angle, outer opening angle, opening diameter and overall shape. HeSTIM thus ensures the reproducible fabrication of asymmetric GNCs with hourglass, bullet-like and blunt-ended tip geometries by laser assisted pulling. Subsequent IV measurements validate the structural integrity and consistency between GNCs fabricated in a similar fashion based on their reproducible conductance and ion current rectification (ICR) behavior. Comparable IV characteristics between imaged and non-imaged GNCs from the same pulling procedures prove the non-destructive imaging by HeSTIM. Further, molecular transport experiments show how differences in pore diameter and opening angle manifest in changes to current drops and dwell times. This opens a route towards the controlled functionalization of different but well defined GNC geometries.

4.2 Theory and Background

4.2.1 Ion Transport through GNCs

The physics of ion transport under an external electric field through a nanosized aperture (> 10 nm) is governed by a set of three coupled classical equations:

1. The Nernst-Planck equation describing the flux of the i-th ion species

$$J_i = -D_i \nabla c_i - \frac{z_i F}{RT} D_i c_i \nabla \psi \pm v_c c_i \quad (4.1)$$

where c_i the concentration, F the Faraday constant, R and T the universal gas constant and temperature, z_i the ionic charge, D_i the diffusion coefficient, ψ the electrical potential and v_c the fluid velocity.

2. The Poisson-Boltzmann equation describing the ion distribution normal (z-direction) to a charged surface

$$\frac{d^2\psi(z)}{dz^2} = -\frac{\rho}{\varepsilon\varepsilon_0} = -\frac{e}{\varepsilon\varepsilon_0}\sum_i c_{i,0}\, z_i\, e^{-\frac{z_i\, e\, \psi(z)}{k_b T}} \quad (4.2)$$

where ε_0 is the electrical permittivity of the free space and ε the relative permittivity, e the elementary charge, k_b the Boltzmann constant $c_{i,0}$ the ion concentration at $z = \infty$.

3. The Navier-Stokes equation describing the fluid velocity field v_c under the assumption of constant viscosity, water as an incompressible Newtonian fluid, by neglecting inertia (*i.e.* creeping flow approximation) and no pressure gradient between the trans and the cis sides

$$\eta \nabla^2 v_c = F_b \sum_i z_i c_i \nabla \psi \text{ and } \nabla v_c = 0 \quad (4.3)$$

where η is the viscosity and F_b the body force.

This coupled system of Poisson-Nernst-Planck-Stokes equations is often called space-charge model. A graphical pedigree originating from first principles is shown in Figure 4.2. For a particular geometry, Equations (4.1) through (4.3) are usually solved by finite-element calculations at a high computational cost. Here, experimental data is discussed by the means of a simple analytical model for the

GNC pore resistance R_P. However, the interested reader of ion transport is referred to a comprehensive review by Schoch *et al.* (2008)[22].

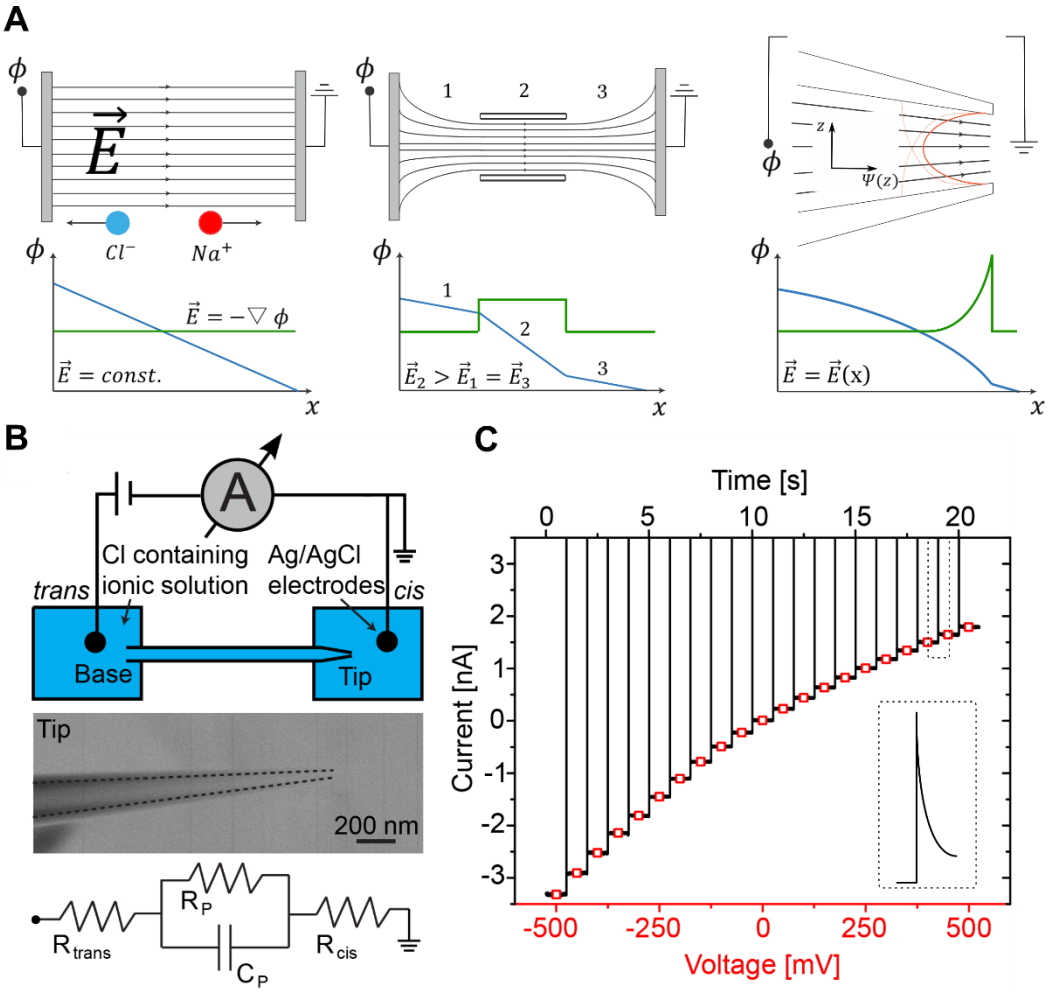

Figure 4.1: Current to Voltage Measurements of Glass Nanocapillaries. **A**, The physical basis of nanopore sensors is that the potential drops mainly over the small dimensions of the connecting pore. An ionic current through the pore therefore drops upon partial blockage (*e.g.* due to the passage of electrokinetically driven biomolecules from one reservoir to the other). The current to voltage characteristics are hence primarily determines by the size and shape of the opening. **B**, Schematic of a PDMS reservoir with an integrated GNC. The cis reservoir is kept at ground while the potential of the trans Ag/AgCl electrode is swept. The HeSTIM image shows a typical blunt ended tip. Dashed lines are guides to the eye that outline the inner cavity. For a transverse applied potential this system is best described by an equivalent model circuit with four main components: R_{trans}, C_P, R_P and R_{cis} (see main text). **C**, A typical current I to voltage V response for a bullet-like GNC (red open boxes). The black trace is the corresponding contiguous time to current trace, where the applied voltage is stepwise increased (+50 mV) after every second, starting from -500 mV. Each voltage step will initially (t → 0) drop entirely over the reservoirs, which leads to the current spikes at the beginning of each step. The current will then decay according to the charging of the capacitance between the solution and GNC wall before it stabilizes at a value solely defined by the pore resistance. Current mean values at a given voltage (red open boxes) are therefore obtained from averaging over stable current-time traces (t > 0.2 s after each voltage step).

Assuming uncharged walls and a constant ion concentration, ion current flow between the two reservoirs via an immersed GNC is best described by the equivalent model circuit depicted in Figure 4.1B. Four main components can be assigned: The capacitance C_P between the solution and GNC wall, the pore resistance R_P and the resistances from the electrodes to the GNC tip and base openings in both reservoirs R_{cis} and R_{trans} respectively, whereas $R_{cis} \approx R_{trans} = R_R$. The capacitance C_P is thereby in parallel with R_P which is in series with the resistance R_R [ref. 23]. Each voltage step will initially ($t \rightarrow 0$) drop entirely over R_R [ref. 24], which leads to a steep current increase (Figure 4.1C). The current will then decay according to the charging of the capacitance C_P before it stabilizes at a value solely defined by R_P ($t > 0$), since $R_R + R_P \approx R_P$. Current mean values at a given voltage are therefore obtained from averaging over stable current-time traces ($t > 0$). The stabilized current between the two reservoirs at a given V and ionic strength is then mainly defined by R_P and hence dominated by the GNC pore diameter d_P. For pores exhibiting Ohmic behavior, an approximation of R_P solely based on the geometry of the GNCs can be performed by the relationship[25]

$$R_p = \frac{4l}{\sigma\,\pi d_B^2} + \frac{2\cot\left(\frac{\Theta}{2}\right)}{\sigma\,\pi}\left(\frac{1}{d_P} - \frac{1}{d_B}\right) \approx \frac{2\cot\left(\frac{\Theta}{2}\right)}{\sigma\,\pi d_P} \rightarrow \sigma = \frac{2\cot\left(\frac{\Theta}{2}\right)}{\pi d_P R_p} \quad (4.4)$$

where σ is the solution conductivity, l is the length of the GNC base, Θ is the full inner opening angle and d_B is the diameter of the base (here 200 µm). Nevertheless, it is the tip shape itself which determines the electrical field line distribution and thus determines the ion transport properties at least as much as the pore size[8,26]. Accordingly, the *I-V* response of a GNC provides a means to interrogate the different tips such as the blunt, bullet and hourglass shaped GNCs presented in Section 4.4.

4.2.2 Effect of Surface Charge on Ion Current

Exclusive geometric considerations to deduce the ionic current from Equation (4.4) are not straightforward due to the departure of the *I-V* curve from Ohmic behavior for some of the GNCs (Figures 4.1 and 4.6). The origin of this ion current rectification (ICR) is being extensively debated[4,14,27]. General agreement exists that ICR is inherent to charged axially asymmetric nanopores (either geometrically or in surface charge distribution) when the pore diameter is of the order of the Debye screening length λ_D [ref. 28]. The GNCs shown in Figure 4.1 and Figure 4.6 fall into this category as their tip geometries are asymmetric along their axes and their glass surfaces bear a fixed surface charge of -0.02 C/m^2 at pH 7.2 [ref.29].

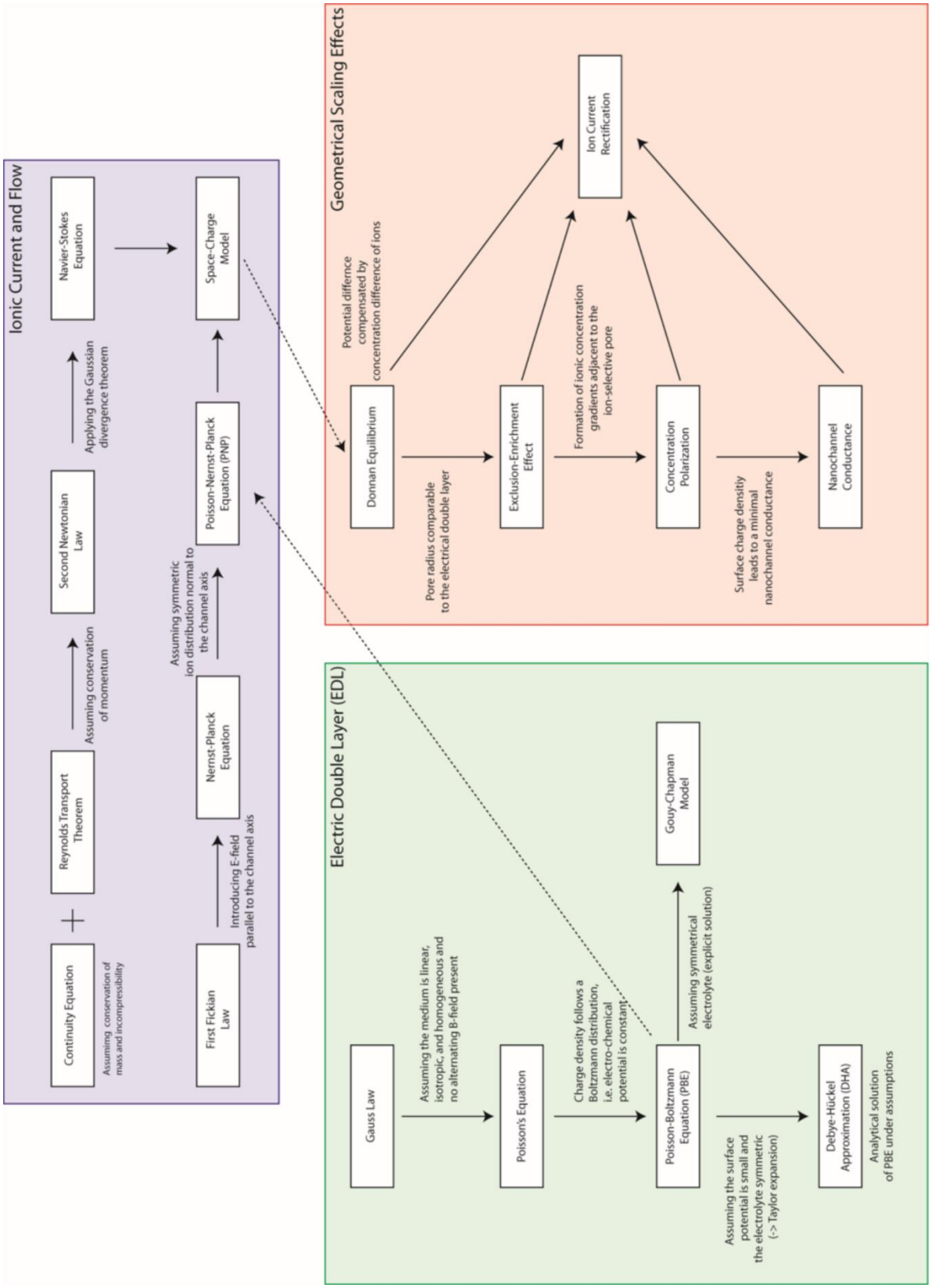

Figure 4.2: Towards Ion Current Rectification from First Principles.

To understand the origin of ICR, finite-element simulations based on Poisson-Nernst-Planck and Navier-Stokes Equations (4.1) through (4.3) have identified a voltage-dependent conductivity ($\sigma \rightarrow \sigma\ (V)$) in the vicinity of the GNC pore mediating ICR[28,30]. As a consequence, the conductivity along the GNC axis shows maxima and minima as opposed to the bulk solution ($\sigma \rightarrow \sigma\ (x,V)$). A maximum of $\sigma\ (x,V)$ located next to the GNC pore opening will thus result in a high current state and a minimum in a low current state. The dependence of minima and maxima positions on the polarity of the applied voltage then leads to the fact that $|I(+V)| \neq |I(-V)|$. A flow chart summarizing the underlying physical origins of ICR is shown in Figure 4.2.

4.2.3 Helium Scanning Transmission Ion Microscopy

The geometries of asymmetrical GNCs were determined by the use of a He focused ion beam microscope. Briefly, a focused He ion beam scans over a sample similar to a traditional SEM[31] (Figures 4.3A and 4.3B). Here, the image is generated from the detection of secondary electrons (SE) that are excited by impinging He ions. In contrast to the most abundant imaging techniques based on electrons (SEM, TEM and STEM) and Gallium ions (Gallium FIB), He ions enable imaging of non-coated, insulating GNCs mainly due to their larger mass than electrons and lower mass than Gallium ions. First, beam currents as low as 0.1 pA were suitable for image generation since SE are mostly excited by the incoming He ions via kinetic emission, leading to an approximately 70 fold higher SE yield δ than electrons ($\delta_e \approx 0.1$ and $\delta_{He} \approx 7$)[32]. The low beam current at the typical acceleration voltages of 25 and 30 kV used throughout this study ensured non-destructive image generation. Higher He beam currents would destroy the GNCs through significant sputtering and heating effects during the image acquisition. Second, given the small He ion scattering cross section, He ion scattering with the sample nuclei is not efficient, *i.e.* He ions are less likely to collide with sample atoms. This results in a considerable penetration depth before the beam diverges[33]. Consequently, SEs from the GNCs are excited within a narrow conical interaction volume over hundreds of nanometers (unlike the bell-shaped interaction volume for electrons or Gallium ions)[32]. Third, the de Broglie wavelength is of orders of magnitudes smaller than for electrons allowing for probe sizes as small as 0.25 nm [ref. 34]. Since the escape depth of SE excited by electronic collisions with He ions is restricted to a few nanometers, the small probing size and low beam divergence predominantly defines the superior spatial resolution over electron and Gallium based imaging techniques.

At different positions on the tip, He ions encounter a tapered glass surface of different thicknesses (Figure 4.3A and B). The number of He ions transmitting the GNCs therefore depends on the actual position the beam impinges on the tip, as the number of nuclear collisions and hence the energy loss is given by the encountered wall thickness. Both the escaping SE and the incoming He ions contribute positive charge to the sample. However, given the insulating nature of the GNCs these contributions are highly localized. Regarding their large penetration depth, non-transmitted He ions are mainly buried and neutralized deep within the GNC wall, while the accumulation of remaining positive holes due to SE emission is restricted to the escape depth near the surface. Because the interaction volume within the escape depth increases with the angle between the local surface normal and the incident beam, charge accumulation per incoming ion increases against the edges of the GNC. The transmitted component of the beam travels further and excites additional SE from the Aluminum background below the GNC tips. Those SE are attracted either towards the secondary electron detector or towards the positively charged GNC tip, thereby neutralizing the accumulated surface charge and suppressing major charging effects (Figure 4.3C). Considering the low primary He ion beam current of 0.1-0.5 pA, charges buried in the wall can readily dissipate and have a neglectable effect on the transmission of impinging He ions. Assuming full neutralization of the surface charge on the GNC, the total amount of detected SE is equal to the SE emitted from the Aluminum background, whereas $\delta_{Glass} << \delta_{Aluminum}$. The Aluminum background therefore acts as an energy loss detector of transmitted He ions and hence gives a direct measure of the transited GNC wall thickness. The application of a simple geometrical model (*vide infra*) enables the direct correlation between the cross sectional SE intensity profile and the transited glass thickness. This then allows for a straight forward three-dimensional reconstruction of the suspended GNC.

Our geometrical considerations start from the assumption of radial symmetry around the entire GNC axis from the base to the tip. This allows one to describe the position of the beam on the GNC circumference in polar coordinates relative to the capillary axis as origin (Figure 4.4A). The acquired cross sectional intensity profile at a given point along the GNC axis describes a “w” shaped form with a reflection plane along the axis of the GNC (Figure 4.4B and C). The intensity level was normalized to the areal average of the left and right quarters of each image away from the tip, where the He ions are supposed to arrive on the Aluminum background unperturbed (Figure 4.4B).

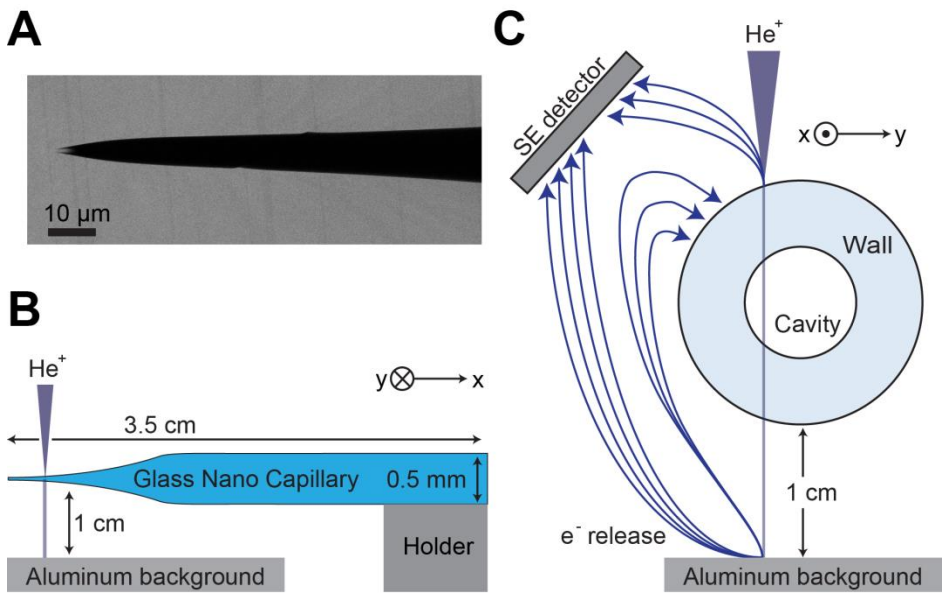

Figure 4.4: Principle of Helium Scanning Transmission Ion Microscopy. **A,** Top overview HeSTIM image of a GNC. He ions are able to transmit at the very tip. **B**, Schematics of the HeSTIM imaging assay with the glass nanocapillary arranged perpendicularly to the incoming Helium beam. Images with field of views of 2 µm and 100 µm were obtained at the very tip end. **C** Schematic of the contrast generating mechanism based on SE detection viewed along the nanocapillary axis from the base to the tip. The component of Helium beam reaching the Aluminum background depends on the encountered mass density in the beam path.

Departure from the baseline is therefore determined by the increase in encountered wall thickness D_I, simply following a sinusoidal

$$D_I = D\ sin(\alpha) \quad (4.5)$$

until the first minimum, with D the outer GNC diameter and α the angle between D and the horizontal mid plane. Accordingly, the position of the first local minimum corresponds to the start of the GNC cavity, where the He ions encounter the longest path through the wall and $\alpha = \beta$ (see Figure 4.4A for details). From this point, the intensity recovers proportional to the perpendicular chord of the cavity until it reaches a local maximum. Therefore, this section of the intensity profile corresponds to wall thickness progression D_{II} described by

$$D_{II} = D \sin\beta - d\sqrt{1 - \frac{D\cos\alpha}{d}} \quad (4.6)$$

with d the diameter of the GNC cavity. The local maximum defines the position of the reflection plane where the He ions pass a wall thickness of exactly $D - d$. Simulations based on these simple geometric arguments show excellent agreement with the acquired profiles (Figure 4.4C).

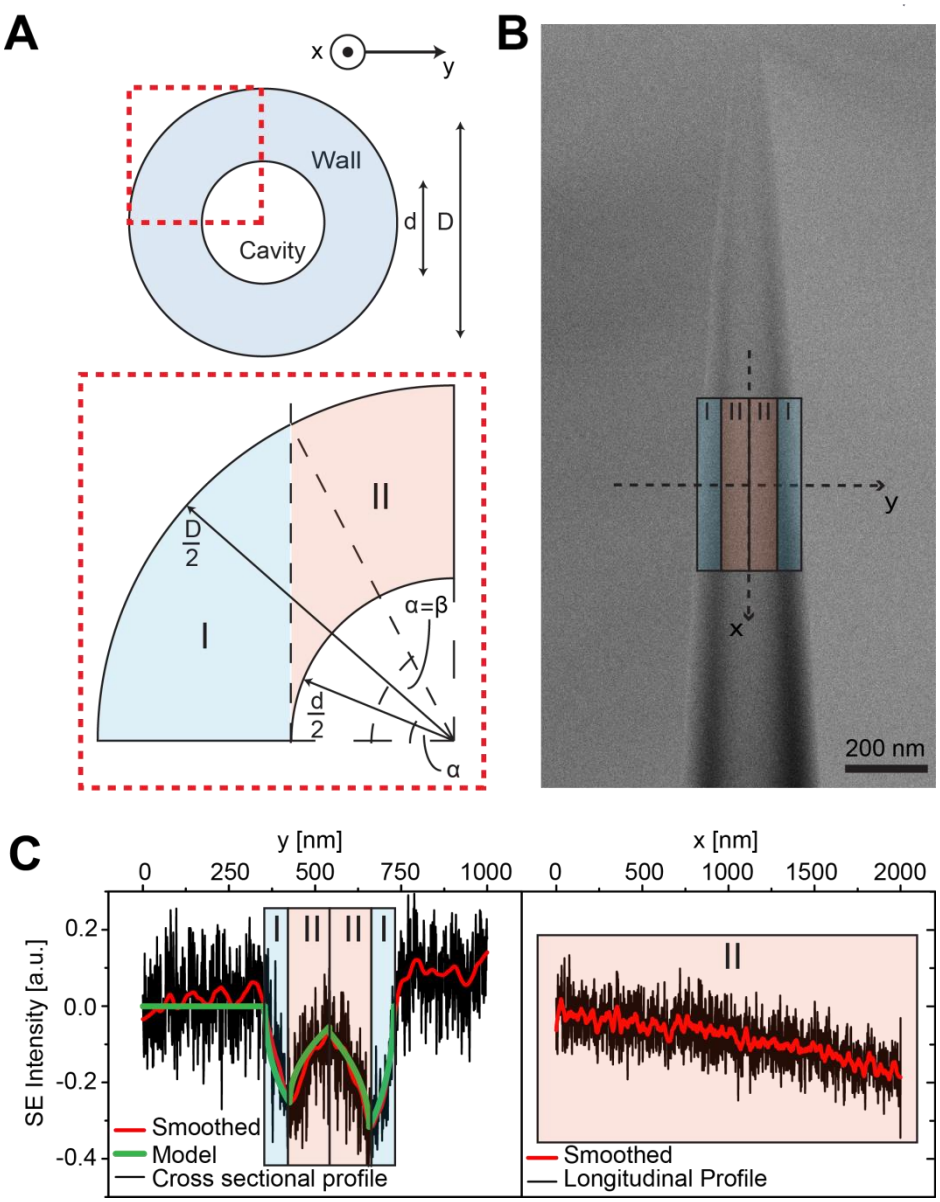

Figure 4.5: Analysis of Helium Scanning Transmission Ion Microscopy Images. **A**, Zoom in on the quarter of a circular nanocapillary cross section. Two distinct regimes can be identified: I where the helium beam travels entirely through glass and never crosses the inner cavity of the nanocapillary and II where the beam crosses the inner cavity. Axis orientation corresponds to **B** and **C**. **B**, Image of a representative GNC tip, with the sequence of regimes I and II from **A** indicated. **C**, Cross sectional and longitudinal profile along the x- and y-axis in **B** respectively. Smoothing was performed with a 50 point moving average filter. The green line is a simulation of the model described in the main text.

We further confirmed the linear relation between the cross sectional intensity profile and mass density (*i.e.*, wall thickness) with the dependence of the He ion absorption on different altitude angles (see Appendix Chapter 4).

4.3 Characterization of Differently Shaped GNCs by Helium Scanning Transmission Ion Microscopy

Having an imaging technique for uncoated GNCs on hand allowed for the fine-tuning of instrument specific pulling parameters leading to distinct tip shapes (see Appendix Chapter 4). We were able to fabricate GNCs with blunt, bullet and hourglass geometries with different opening diameters and opening angles (Figure 4.5). Blunt-ended tips distinguished from bullet-like ones by their streamlined inner and outer conical shape to the very tip end, while bullet-like develop a stronger taper of the outer tip walls. Hourglass shaped GNCs display a trumpet-like opening region which merges into a smaller pore from where the cavity radius starts to increase in a conical manner again.

In general, hourglass GNCs exhibited larger opening diameters as compared to blunt and bullet like ones. Hereinafter we refer to the location of smallest diameter in the GNC tip cavity as “pore” and to the orifice at the very GNC tip end as “opening”. The HeSTIM images reveal, given the fact that GNCs were produced via a thermal process, a surprising reproducibility from tip to tip (see Appendix Chapter 4). The geometric properties of these GNCs are summarized in Table 4.1.

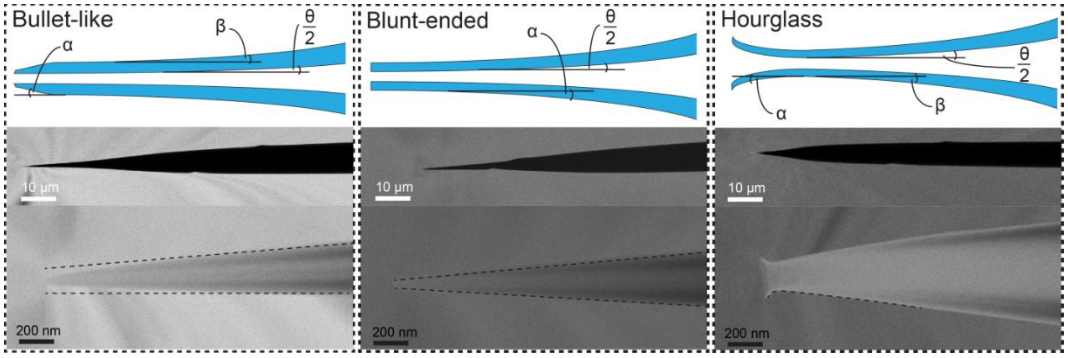

Figure 4.6: Schematics and Corresponding Images of Asymmetric Bullet-Like, Blunt-Ended, and Hourglass Tip Shapes. The indicated angles were used to characterize the different type of shapes and are summarized in Table 4.1. Dashed lines in the zoomed in images are guides to the eyes to emphasize the different tip shapes.

Table 4.1: Summary of Geometric Properties for Each Different GNC.

Bullet-like	1 (N=10)	2 (N=10)
1. Outer Angle [°] α	7.8 ± 1.6	8.7 ± 1.6
2. Outer Angle [°] β	4.1 ± 1.6	4.5 ± 0.5
Half Opening Angle [°] $\frac{\Theta}{2}$	2.5 ± 0.3	2.8 ± 0.4
Pore Diameter [nm]	29 ± 4	39 ± 8
Blunt-like	**3 (N=10)**	**4 (N=10)**
Outer Angle [°] α	3.9 ± 0.6	4.6 ± 0.8
Half Opening Angle [°] $\frac{\theta}{2}$	2 ± 0.4	2.5 ± 0.5
Pore Diameter [nm]	25 ± 4	30 ± 9

Hourglass-like	5 (N=7)	6 (N=8)	7 (N=10)
1. Outer Angle [°] α	17.1±9.1	22.7±3.5	21.9±3.2
2. Outer Angle [°] β	5±0.7	5.7±1.2	8.9±1.5
Half Opening Angle [°] $\frac{\theta}{2}$	2.2±0.4	3.5±1	6.7±1.8
Opening Diameter [nm]	68±17	127±37	426±85
Pore Diameter [nm]	43±6	71±32	327±86

Refer to Figure 4.5 for definition of α, β and θ/2.

4.4 Characterization of Differently Shaped GNCs by Ion Current Rectification

For molecular transport studies, it is essential to characterize the GNCs by their electrical properties. In order to do so, individual GNCs were mounted between two salt solution (Gibko PBS, 150 mM NaCl pH 7.2) reservoirs (Figure 4.1B). An ionic current *I* was then driven through the GNC by applying an electric potential Φ to the reservoir containing the base of the GNC (*trans*), while keeping the tip containing reservoir at ground (*cis*).

Although the *I-V* curves in Figure 4.6A for ensembles of hourglass (*N* = 8, pore type 5 from Table 4.1), bullet (*N* = 7, type 2) and blunt (*N* = 5, type 3) shaped tips show a moderate negative rectification $|I(+V)| < |I(-V)|$, notice that high voltage regimes (-500 to -250 and 250 to 500 mV respectively) behave nearly Ohmic. Using the properties outlined in Table 4.1, linear fits to these ranges give estimates of the local voltage-dependent conductivity in the vicinity of the GNC pores from pure geometrical deliberations by Equation (4.4), as summarized in Table 4.2.

Table 4.2: Conductance Values and Calculated Conductivity Differences for Each GNC Shown in Figure 4.6A.

GNC type	G_{500mV} [nS]	G_{-500mV} [nS]	$\Delta\sigma$ [mSm^{-1}]
Blunt	1.18	2.17	721
Bullet	2.24	3.75	503
Hourglass 1	3.81	4.42	235

SE of the linear fits are all below $\pm$ 40 pS and are not considered.

The rectification for GNCs shown in Figure 4.6A is generally moderate due to the large pore radii from ~10 nm to ~20 nm compared to λ_D at 150 mM NaCl (~ 1 nm). To quantify differences in rectification, we define a weighted rectification ratio given as

$$\xi = \frac{|<I(+V)>|}{|<I(-V)>|}\frac{|V|}{500\ mV} \qquad (4.7)$$

for all potentials *V* between -500 mV and 500 mV. This is shown in Figure 4.6B, where one finds significant differences which cannot simply be explained by the different pore diameter d_P and opening angles Θ. Deviation from the dashed line in Figure 4C corresponds to a non-Ohmic behavior for a given voltage. The highest negative rectification is observed for the blunt GNCs, anticipated from having the smallest d_P and comparable Θ. Interestingly, the bullet tips show comparable

rectification properties, $\xi_{blunt}(V) = \xi_{bullet}(V)$, in spite of having larger d_P and Θ values. This unexpected result might be attributed to their different tip shapes, such that the thinner wall of bullet tips might experience stronger field effects from the outer tip surface that alter the electrical field distribution and local ion concentration in their lumina[35]. The hourglass GNCs on the other hand show less ICR than bullet ones ($\xi_{bullet}(V) < \xi_{hourglass}(V)$), despite the fact that they have comparable d_P and comparable Θ. While field effects might exist, we postulate that hourglass GNCs show a higher axial symmetry as compared to blunt-ended and bullet-like tips. Indeed, an impressive reduction of the ICR has recently been shown by the transition from purely conical towards hourglass shaped nanochannels in PET membranes[36].

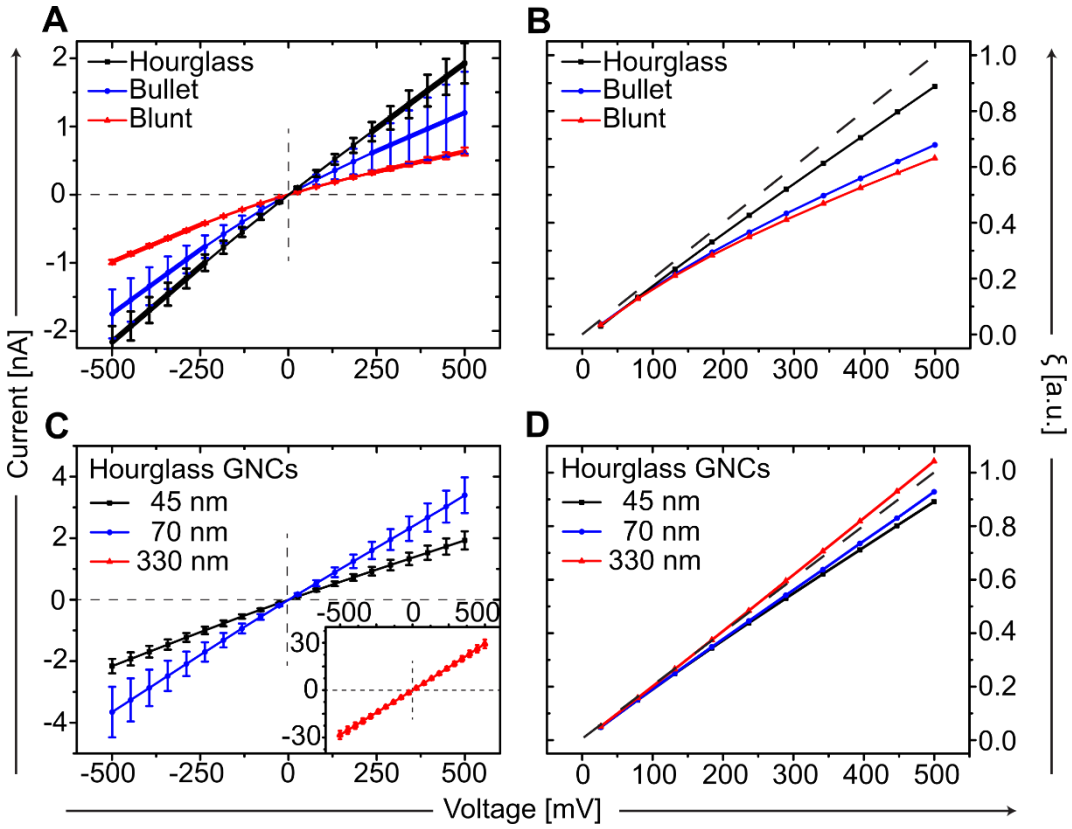

Figure 4.7: Characterization of Differently Shaped GNCs by Ion Current Rectification. **A**, Comparison of *I-V* responses for hourglass (N = 8, pore diameter d_P = 43±6 nm, full opening angle Θ = 4.4±0.8°), bullet (N = 7, d_P = 39±8 nm, Θ = 5.6±0.8°) and blunt (N = 5, d_P = 25±4 nm, Θ = 4±0.8°) shaped GNCs. In all cases, the high voltage regime at both polarities (-500 to -250 and 250 to 500 mV respectively) can be fitted linearly to obtain a lower and upper conductance limit (see Table 2). **B**, ICR ratios ξ for the GNCs from **A**. Deviations at a given voltage below the dashed line correspond to negative rectification (see main text). **C**, Comparison of *I-V* responses between ensembles of hourglass shaped (N = 8, d_P = 43±6 nm, Θ = 4.4±0.8°; N = 7, d_P = 71±32 nm, Θ = 7±2°) GNCs, Inset: N = 8, d_P = 327±86 nm, Θ = 13.4±3.8°. **C**, Increasing pore size reduces ICR for hourglass GNCs shown in **D**.

Observing that the emergence of Ohmic behavior correlates to the increase in d_P for hourglass GNCs (N = 8, type 5; N = 7, type 6; N = 8, type 7) presented in Figure 4.6C and D, we then apply the simplified expression[13]

$$d_P = \frac{4Gl}{\pi\sigma d_B} \quad (4.8)$$

with l the length of the taper and G the conductance, assuming a conical approximation from tip to base. This enables a comparison between the pore diameters deduced by HeSTIM imaging in Table 4.1 and the calculated diameters from the related conductance values, which are summarized in Table 4.3.

Table 4.3: Calculated GNC Pore Diameters d_p for the Different Hourglass GNCs Shown in Figure 4.6C.

GNC type	G [nS]	l [mm]	d_p [nm]
Hourglass 1*	4.09	2.6	42
Hourglass 2	7.02	2	56
Hourglass 3	57.62	1.5	344

Conductance value G of Hourglass 1* is the average of G_{500mV} and G_{-500mV} from Table 4.2. SE of the linear fits are all below $\pm$ 40 pS and are not considered.

Interestingly, the calculated values correspond approximately to the measured pore diameters (compare with Table 4.1). At this point, it should be emphasized that the narrow distribution of the *I-V* curves supports the reproducibility for the different GNC types as found by HeSTIM imaging.

4.5 Effect of Tip Shapes on Protein Translocation Signals

Next, we measured the translocation of bovine serum albumin (BSA) through GNCs of different geometries. The baseline in Figure 4.7 shows a representative current-time trace $I_B(t)$ for an hourglass GNC at 500 mV for 10 s, mainly fluctuating around its mean value due to intrinsic low-frequency ionic current noise. Upon application of 1 µM of BSA to the *cis* reservoir, current drops emerge from transient ion blockages $\Delta I(t)$ due to BSA translocation (translocation trace). The translocation of the negatively charged BSA molecules (hydrodynamic diameter d_{hyd} = 7 nm measured from dynamic light scattering, data not shown and theoretical isoelectric point *pI* = 5.6) towards the positive potential ($\Phi > 0$) indicates that electrophoretic transport dominates over electro-osmosis. As usual,[16] single translocation events are characterized by their duration and mean current drop amplitude (Figure 4.7B) and recognized as such when $|\Delta I(t)| > 5\, I_{B,rms}$, with $I_{B,rms}$ being the root mean square of the baseline current. The entire translocation process thereby consists of two asymmetric phases, the capture of the proteins on the *cis* side and the actual translocation through the GNC pore towards the *trans* side. The event duration is therefore a composition of the capture time (*cis*) and the residential time of the BSA molecules in the sensing volume (*trans*) while the maximal current drop depends on the ratio between d_P and d_{hyd}. Particle passage analysis of well-defined molecules (BSA) at a common set of parameters (*V* = 500 mV, 150 mM NaCl pH 7.2, *BW* = 10 kHz, sample rate = 100 kHz, 1 µM BSA) may thus open an additional way to investigate the GNC geometries. Similar studies to characterize nanopore geometries by their particle translocation properties have been performed recently for symmetric membrane embedded systems[37,38].

The current drops in Figure 4.7A and B can be directly converted into changes of conductance ΔG considering near-Ohmic behavior around 500 mV. To compare amongst different GNC pores with different $I_B(t)$, mean conductance changes of translocation events are normalized by the respective baseline conductance, $\langle \Delta G \rangle / \langle G_B \rangle = \langle \Delta I \rangle / \langle I_B \rangle$. The event times are defined as the duration of the first deviation from the baseline ($|\Delta I(t)| > 0$) until its recovery ($|\Delta I(t)| \rightarrow 0$) and are directly comparable between pores. Individual BSA translocation events from within a 1 min trace are then represented as single point in a scatter plot as presented in Figure 4.7C for bullet (blue: type 2, n = 43), blunt (red: type 3, n = 781; green: type 4, n = 68) and hourglass shaped (black: type 5, n = 2687) GNCs. The mean normalized current drops are 0.3 %, 3.9 %, 1.3 % and 1.2 % and the mean event durations 0.32 ms, 2.05 ms, 1.64 ms and 1.93 ms respectively. The

considerable differences in event frequency likely stem from different shape effects since all other parameters between the measurements remained unchanged. Regardless, we do observe large device to device variations in the event rates between GNCs fabricated from the same pulling parameters. The reason for this variation is not understood and awaits further study.

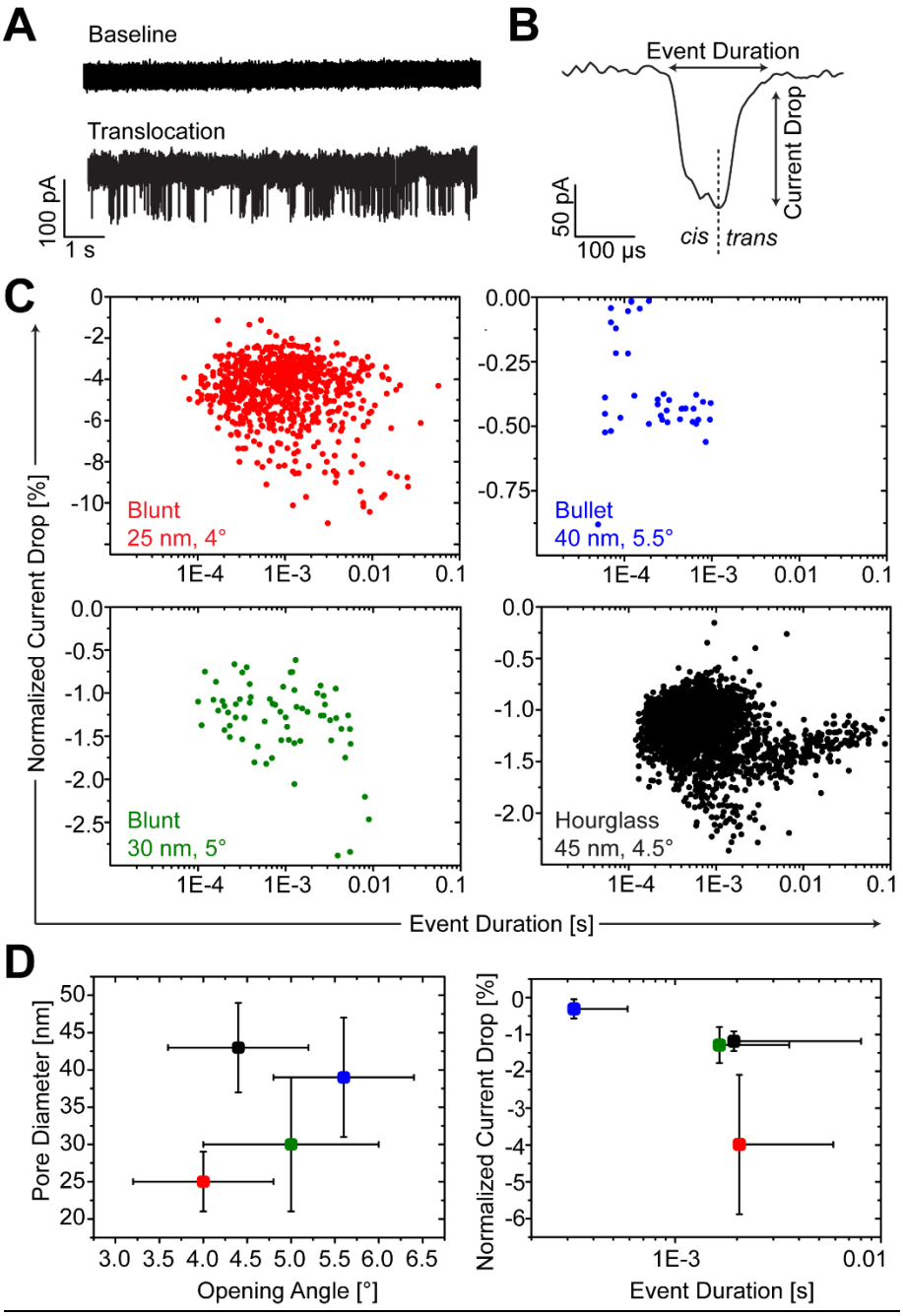

Figure 4.8: Effect of Tip Shapes on Protein Translocation Signals. **A**, Ion transport through an hourglass geometry at a certain voltage leads to a current-time trace only fluctuating due to ionic current noise (baseline), while translocation of BSA molecule manifests in temporal current drops (translocation). BSA molecules in translocation experiments are always applied to the cis reservoir (Figure 4A). **B**, Zoom into a single translocation event which is characterized by the event duration and the associated current drop. The event asymmetry around the maximal current drop is likely to occur due to the geometrical asymmetry of the tip. **C**, Red and green: blunt ended, blue: bullet-like and black hourglass GNC. Each point in the scatter plots corresponds to a single translocation event. All plots are obtained at 500 mV with 1 µM BSA applied to the cis chamber. **D**, Pore geometry versus event distribution corresponding to the colors in **C**. Smaller pore diameters (25 nm) lead to bigger current drops (4 %), smaller angles (4 °) to longer event durations (2 ms).

4.6 Discussion and Conclusion

Blunt-ended, bullet-like and hourglass shaped GNC tips have been reproducibly fabricated by laser-assisted pulling. The non-destructive characterization using HeSTIM is evident by the analysis of the electrical conductance and their corresponding ICR properties. Variations in electrical transport characteristics largely originate from the physical shape of the tip, since all GNCs were fabricated from the same material and by the same technique. Nevertheless, we observed the least influence of ICR and highest capture rates for hourglass tips, suggesting their utility in biomimetic and selective nanochannels[39].

4.7 Materials and Methods

4.7.1 Fabrication of GNCs

Asymmetrical GNCs were produced by laser-assisted capillary pulling (Sutter instruments P-2000 B) from the same type of quartz capillaries (Hilgenberg; O.D. 500 µm, I.D. 200 µm with inner filament), heated with the same laser spot size and pulled with a constant load. The puller exposes the capillaries to a tunable CO_2 (up to 10 W) IR laser (approx. λ = 10 µm) beam with a minimal spot size of 0.1 mm. Quartz glass absorbs firmly in the infrared and is heated up to the melting point (approx. 1700 °C) upon irradiation with the laser. Pulling and heating at the same time then leads to a shrinking of the exposed region of the capillary. A final pull separates the thinned middle region resulting in two GNCs. The pulling parameters are summarized in the Appendix of Chapter 4.

4.7.2 HeSTIM Imaging

Imaging was performed with a He ion microscope (OrionPlus, Carl Zeiss Microscopy GmbH). The GNCs were mounted more than 1 cm away from an Aluminum background on a custom-made sample holder allowing for scan angles from 0° (central capillary axis perpendicular to the beam) to 90° (central capillary axis parallel to the beam). Prior to the transfer of the GNCs to the main chamber a plasma cleaning procedure was performed (10W air plasma for 3 min at 0.8 mbar). The focused He ion beam was then rastered across the tip endings of the GNCs (Figure 4.3B), where the wall thickness is either <100 nm (field of view 2 µm) or >100nm (field of view 100 µm). Comparability between images was guaranteed with a constant image resolution of 0.94 nm^2 per pixel. Standard acquisition parameters were ~8 mm working distance, 0.1 - 0.5 pA beam current, 25 and 30 kV acceleration voltage, a dwell time of 0.5 or 1 µs and 16 or 32 line averaging. Image processing was performed with ImageJ (ImageJ 1.48v) and by a custom written MATLAB code (MATLAB r2012b, The MathWorks).

4.7.3 Measurement Procedure

Single GNCs were mounted as sole connection between two reservoirs filled with filtered (0.22 um, TRP) PBS (pH 7.2, 150 mM NaCl, Gibko) in homemade PDMS cells (Figure 4.1B). Wettability was increased by hydrophilizing the glass surface in an O_2–plasma (13.56 MHz, 12.5 W, 5 sccm, 5 min, Femto, DienerElectronics). The O_2 plasma conditions have a strong influence on the I–V characteristics; therefore, the geometrical integrity of each GNC structure was preserved by a choice of mild plasma conditions (see Appendix Chapter 4). A current amplifier (Axopatch 200B, Axon Instruments) was used to apply potentials (-500 mV to 500 mV) between the

reservoirs and to measure the ionic current through the GNC. Custom-made Ag/AgCl electrodes were placed with the ground electrode in the reservoir with the tip of the GNC (*cis*) and with the reference electrode setting the potential in the reservoir with the base of the GNC (*trans*). Currents were low pass filtered (internal 4-pole Bessel) at 10 kHz or 100 kHz and sampled at 100 kHz or 1 MHz with a NI-PCIe-6251 card (National Instruments), respectively. *I*−*V* responses of individual GNCs from program 1 to 7 are shown in Appendix of Chapter 4. A custom written LabView (LabView v13.0, National Instruments) program was used to record and analyze the *I*-*V* curves as well as the translocation events of BSA (>98 %, lyophilized, Sigma-Aldrich) shown in Figure 4.6 and 4.7. All graphs were produced by OriginPro (OriginPro v9.1.0, OriginLab Corp.) and all schemes designed in Adobe Illustrator (Adobe Illustrator CS5 v15.0.2, Adobe Systems Inc.)

4.8 References

1. Bayley, H. & Martin, C. R. Resistive-Pulse SensingFrom Microbes to Molecules. *Chem. Rev.* **100,** 2575–2594 (2000).
2. Venkatesan, B. M. & Bashir, R. Nanopore sensors for nucleic acid analysis. *Nat. Nanotechnol.* **6,** 615–624 (2001).
3. Fologea, D., Ledden, B., McNabb, D. S. & Li, J. Electrical characterization of protein molecules by a solid-state nanopore. *Appl. Phys. Lett.* **91,** 539011–539013 (2007).
4. Apel, P. Y., Korchev, Y. ., Siwy, Z., Spohr, R. & Yoshida, M. Diode-like single-ion track membrane prepared by electro-stopping. *Nucl. Instruments Methods Phys. Res. Sect. B Beam Interact. with Mater. Atoms* **184,** 337–346 (2001).
5. Yameen, B. *et al.* Synthetic proton-gated ion channels via single solid-state nanochannels modified with responsive polymer brushes. *Nano Lett.* **9,** 2788–2793 (2009).
6. Kalman, E. B., Vlassiouk, I. & Siwy, Z. S. Nanofluidic bipolar transistors. *Adv. Mater.* **20,** 293–297 (2008).
7. Ali, M. *et al.* Single cigar-shaped nanopores functionalized with amphoteric amino acid chains: Experimental and theoretical characterization. *ACS Nano* **6,** 3631–3640 (2012).
8. Apel, P. Y., Blonskaya, I. V, Orelovitch, O. L., Ramirez, P. & Sartowska, B. A. Effect of nanopore geometry on ion current rectification. *Nanotechnology* **22,** 175302-1–175302-13 (2011).
9. Li, J. *et al.* Ion-beam sculpting at nanometre length scales. *Nature* **412,** 166–169 (2001).
10. Lanyon, Y. H. *et al.* Fabrication of nanopore array electrodes by focused ion beam milling. *Anal. Chem.* **79,** 3048–3055 (2007).
11. Storm, A. J., Chen, J. H., Ling, X. S., Zandbergen, H. W. & Dekker, C. Fabrication of solid-state nanopores with single-nanometre precision. *Nat. Mater.* **2,** 537–540 (2003).
12. Haywood, D. G., Saha-Shah, A., Baker, L. A. & Jacobson, S. C. Fundamental studies of nanofluidics: Nanopores, nanochannels, and nanopipets. *Analytical Chemistry* **87,** 172–187 (2015).
13. Steinbock, L. J., Otto, O., Chimerel, C., Gornall, J. & Keyser, U. F. Detecting DNA folding with nanocapillaries. *Nano Lett.* **10,** 2493–2497 (2010).
14. Wei, C., Bard, A. J. & Feldberg, S. W. Current Rectification at Quartz Nanopipet Electrodes. *Anal. Chem.* **69,** 4627–4633 (1997).

15. Sa, N. & Baker, L. Experiment and Simulation of Ion Transport through Nanopipettes of Well-Defined Conical Geometry. *J. Electrochem. Soc.* **160,** 376–381 (2013).

16. Li, W. *et al.* Single Protein Molecule Detection by Glass Nanopores. *ACS Nano* **7,** 4129–4134 (2013).

17. Bell, N. a W. & Keyser, U. F. Specific protein detection using designed DNA carriers and nanopores. *J. Am. Chem. Soc.* **137,** 2035–2041 (2015).

18. Steinbock, L. J. *et al.* Probing the size of proteins with glass nanopores. *Nanoscale* **6,** 14380-1–14380-7 (2014).

19. Postek, M. T., Vladár, A. E. & Purushotham, K. P. Does your SEM really tell the truth? How would you know? Part 2. *Scanning* **36,** 347–355 (2014).

20. Steinbock, L. J., Steinbock, J. F. & Radenovic, a. Controllable shrinking and shaping of glass nanocapillaries under electron irradiation. *Nano Lett.* **13,** 1717–1723 (2013).

21. Hall, A. & Yang, J. *Scanning Transmission Ion Microscopy for Imaging and Nanofabrication in the Helium Ion Microscope*. *White Paper* (2012).

22. Schoch, R. B., Han, J. & Renaud, P. Transport phenomena in nanofluidics. *Rev. Mod. Phys.* **80,** 839–883 (2008).

23. Uram, J. D., Ke, K. & Mayer, M. Noise and bandwidth of current recordings from submicrometer pores and nanopores. *ACS Nano* **2,** 857–872 (2008).

24. Smeets, R. M. M., Keyser, U. F., Dekker, N. H. & Dekker, C. Noise in solid-state nanopores. *Proc. Natl. Acad. Sci. U. S. A.* **105,** 417–421 (2008).

25. Snell, F. M. in *Glass Microelectrodes* 111–123 (1969).

26. Ramírez, P., Apel, P. Y., Cervera, J. & Mafé, S. Pore structure and function of synthetic nanopores with fixed charges: tip shape and rectification properties. *Nanotechnology* **19,** 315707-1–315707-12 (2008).

27. Woermann, D. Electrochemical transport properties of a cone-shaped nanopore: high and low electrical conductivity states depending on the sign of an applied electrical potential difference. *Phys. Chem. Chem. Phys.* **5,** 1853–1858 (2003).

28. White, H. S. & Bund, A. Ion current rectification at nanopores in glass membranes. *Langmuir* **24,** 2212–2218 (2008).

29. Behrens, S. H. & Grier, D. G. The charge of glass and silica surfaces. *J. Chem. Phys.* **115,** 6716–6721 (2001).

30. Ali, M., Ramirez, P., Mafé, S., Neumann, R. & Ensinger, W. A pH-Tunable Nanofluidic Diode with a Broad Range of Rectifying Properties. *ACS Nano* **3,** 603–608 (2009).

31. Notte, J. *et al.* An introduction to the helium ion microscope. *AIP Conf. Proc.* **931,** 489–496 (2007).

32. Cohen-Tanugi, D. & Yao, N. Superior imaging resolution in scanning helium-ion microscopy: A look at beam-sample interactions. *J. Appl. Phys.* **104,** 063504-1–063504-7 (2008).

33. Ziegler, J. F., Ziegler, M. D. & Biersack, J. P. SRIM – The stopping and range of ions in matter (2010). *Nucl. Instruments Methods Phys. Res. Sect. B Beam Interact. with Mater. Atoms* **268,** 1818–1823 (2010).

34. Hlawacek, G., Veligura, V., van Gastel, R. & Poelsema, B. Helium Ion Microscopy. *J. Vac. Sci. Technol. B,* **32** 020801-1–020801-13 (2014).

35. Calander, N. Analyte Concentration at the Tip of a Nanopipette. *Anal. Chem.* **81,** 8347–8353 (2009).

36. Zhang, H. *et al.* Bio-inspired Smart Single Asymmetric Hourglass Nanochannels for Continuous Shape and Ion Transport Control. *Small* **11,** 786–791 (2015).

37. Liu, S., Yuzvinsky, T. D. & Schmidt, H. Effect of Fabrication-Dependent Shape and Composition of Solid-State Nanopores on Single Nanoparticle Detection. *ACS Nano,* **7,** 5621–5627 (2013).

38. Davenport, M. *et al.,* The Role of Pore Geometry in Single Nanoparticle Detection. *ACS Nano, **6,*** 8366–8380 (2012).

39. Kowalczyk, S. W. *et al.* Single-molecule transport across an individual biomimetic nuclear pore complex. *Nat. Nanotechnol.* **6,** 433–438 (2011).

Chapter 5

Conclusions and Outlook

Parts of this chapter have been published as
Luo, W., Ruba, A., Takao, D., Zweifel, L. P., Lim, R. Y., Verhey, K. J., & Yang, W. (2017). Axonemal lumen dominates cytosolic protein diffusion inside the primary cilium. *Scientific reports* **7,** 15793-1 – 15793-11 (2017).

5 Conclusions and Outlook

5.1 Conclusions

This thesis provides a stepwise approach to engineer biomimetic NPCs for the *ex vivo* investigation of the FG Nup permeability barrier. Previously employed silanization based surface chemistry to form FG domain brushes on planar glass surfaces[1] failed within the nanoconfined volume of GNCs that resemble native NPC scaffolds[2]. This demanded a new FG Nup immobilization strategy, which is equally applicable to GNCs and, for the sake of comparability, to planar surfaces. The procedure of choice was a NTA – Histidine affinity mediated immobilization on SLBs formed by spontaneous liposome spreading, since their capacity to form FG domain brushes[3,4] and their ability to coat the inner lumen of GNCs[5] have been previously shown. Minimal NPC models formed in this way experience a consistent biointerface independent of the underlying support. This allows them to be addressed in a comparative manner with different techniques. In addition, detrimental effects from different surface chemistries can be excluded when the transition from two- to three-dimensional biophysical assays is performed. In other words, this approach permits the correlation of eventual differences in the response of Kap-FG domain binding between two- and three-dimensional assays directly to the effect of spatial confinement.

Brush formation on SLBs influences the diffusional properties of the lipids underneath, as it immobilizes the NTA modified lipids linked to individual FG domains. The average grafting distance between the domains was derived by correlating the decay of diffusivity of lipid tracers with the immobilization of FG domains. A FRAP based approach was developed to assess the grafting distance of Nups from this decay. This revealed that SLB mediated brushes undergo spatiotemporal density fluctuations which depend on the grafting distance and attractive F-F interactions between individual FG domains, reminiscent of the situation recently observed in native NPCs[6].

Comparative SPR measurements of Kapβ1-FG domain binding showed that the previously described conformational changes, binding affinities and multivalent binding kinetics described on covalently end-grafted FG domains remain preserved, regardless of the fluidity of the underlying lipid substrate. Consequently, close-packed brushes from His-tagged FG domains linked *via* NTA display the similar emergence of a two phase affinity behavior ($K_D \approx 10^{-7}$ M and $K_D \approx 10^{-5}$ M) upon Kapβ1 titration towards physiological conditions (~10 µM)[7] which

are dominated by the same kinetic states found for gold grafted FG domains[8]: At a low Kapβ1 concentration, a fast association rate k_{on} into the largely unsaturated, collapsed FG domain brush pairs with a slow dissociation rate k_{off} due to high binding avidity. At a physiological Kapβ1 concentration, the layers extend upon saturation and two states evolve. A fast k_{on} and k_{off} pair representing the limited multivalent interaction at the brush periphery and a slow k_{on} and k_{off} due to slow penetration and release from the occupied FG domain brush. Furthermore, this SPR assay was used to show that an F -> S Nsp1 mutant is incompetent in Kapβ1 binding.
Strikingly, dual-color FLCCS investigations at low Kapβ1 concentrations indicate a surprisingly high in-layer mobility, although the multivalency of the FG domain - Kapβ1 interaction invokes a slow k_{off} from the collapsed layer. This is understood as the consequence of the binding avidity *per se* since the interactions between the individual FG motives and Kapβ1, which lead to a high specificity towards the layer, are extremely weak and short-lived[9,10]. At physiological Kapβ1 concentrations, the displacement of layer-bound Kapβ1 at timescales of cargo translocation through the NPC (∼5 ms)[11] appears to be further boosted towards the free two-dimensional diffusion limit. However, this effect is also apparent for highly occupied layers without Kapβ1 in the soluble phase. Incorporation of Kapβ1 into the FG domain layer at physiological concentrations is therefore not only accompanied by the emergence of a small, transiently bound Kapβ1 fraction at the periphery of the brush (fast k_{on} and k_{off}) but also by an accelerated displacement of the strongly bound fraction within the brush (slow k_{on} and k_{off}) - regardless of the enhanced molecular crowding. This additional contribution may therefore account for the highly parallelized translocation through the crowded aqueous channel of the NPC as observed *in vivo*[12,13].

GNCs are envisioned to bridge the gap from these two-dimensional platforms to a three-dimensional assay resembling the structure of a NPC (see Section 5.2). Here, various GNC tip geometries have been reproducibly fabricated by laser-assisted pulling and were non-destructively characterized using HeSTIM. The influence of the tip geometries on the electrical transport characteristics, electrical conductance and their ICR properties was further assessed by ion current measurements. This allowed the determination of fabrication parameters, which lead to hourglass shaped tips with a diameter in the range of the aqueous channel of the NPC.

5.2 Outlook

Towards the Determination of Karyopherinβ1 Pathways in Artificial NPCs made from GNCs

Results from preliminary studies using SPEED microscopy[11] (a single molecule fluorescence technique which was previously employed to determine the pathways of Kapβ1 i*n vivo*[11]) show that it should be feasible to investigate the Kapβ1 mobility inside functionalized GNCs. Both, confocal and SPEED, confirm the evolution of a lipid layer covering the inner walls of a GNC. Confocal images capture the boundary region of the propagating SLB within the GNC lumen (Figure 5.1A). The travelling distance from the tip depends on the time the GNC is exposed to the liposome solution and the size of the opening.

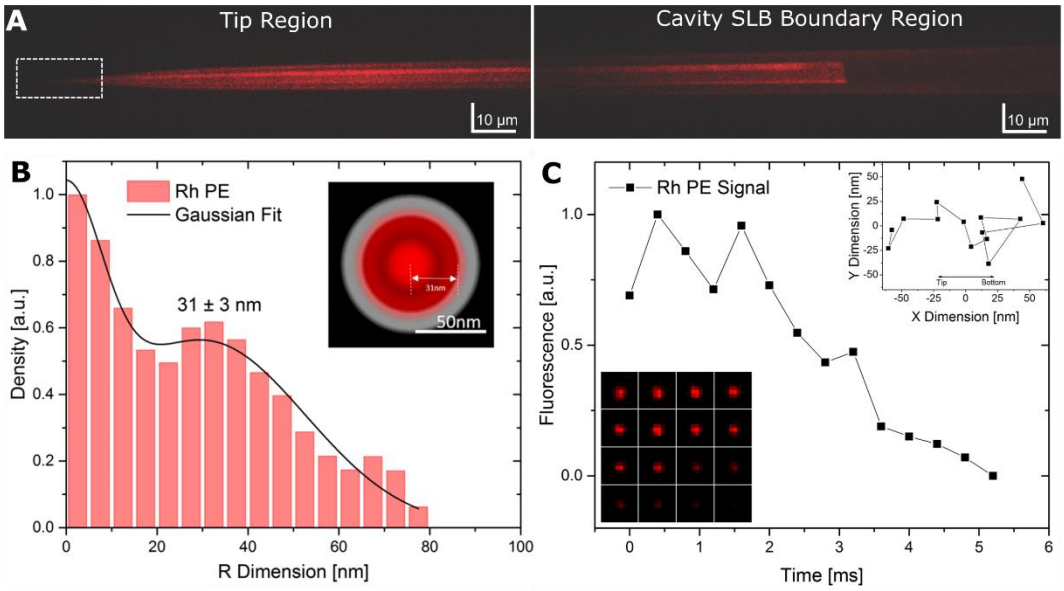

Figure 5.1**:** SLB formation on the inner GNC walls. **A**, Confocal image of the tip region and the boundary region of the propagating lipid bilayer along the inner wall of the same GNC. For representation purposes, images are shown at a ratio of 1:1.5 and were captured after an incubation time of ~1 h. **B**, Spatial density of Rh PE along the radial dimension. Gaussian fitting discloses a bimodal distribution with peaks at the GNC axis and at 31 ± 3 nm. Approximately 70% of the Rhodamine molecules are located within the SLB at the GNC wall. Inset: Cross-section view of the spatial density distribution (red cloud) of liposome (or micelle) diffusion along the central axis and of the SLB at the GNC wall (grey). **C**, Fluorescent signal decay of single liposomes (or micelle) crossing the illumination volume. The majority of Rhodamine modified lipids are quenched after ~5 ms. Lower left inset: Frame by frame montage (400µs) of the fluorescent decay. Upper right inset: Tracking results of the quenched single liposomes diffusing along the x-axis of the GNC lumen.

Thorough rinsing after SLB formation prior to the SPEED experiments was not applicable, due to the fact that the coated GNC are not fixed and must not cross the solution-air interface. Therefore, non-incorporated liposomes or micelles remained in the lumen of the GNC and the Rhodamine fluorescent signal acquired by SPEED microscopy follows a bimodal distribution (Figure 5.1B). One maximum

stems from intact liposomes or micelles and another maximum found 31 ± 3 nm away from the central axis refers to the Rh PE within the formed SLB. The high quantum yield of Rhodamine and the large number of fluorophores per liposome enabled the tracking of single liposomes along the cavity of the GNC at a frame rate of 400µs (Figure 5.1C). The non-incorporated fraction of liposomes was depleted by addition of buffer through the GNC base by means of a microneedle, prior to the immobilization of Alexa Fluor488 labelled Nsp1FF12 (Figure 5.2A). Confocal microscopy indicates the specific attachment of the Nsp1FF12 by the co-localized fluorescent signals of Alexa Fluor488 and Rhodamine (inset image in Figure 5.2B). FRAP experiments on the functionalized GNCs thereby corroborate the fluidity of the SLB underneath the Nsp1FF12 layer as for planar surfaces (Figure 5.2B).

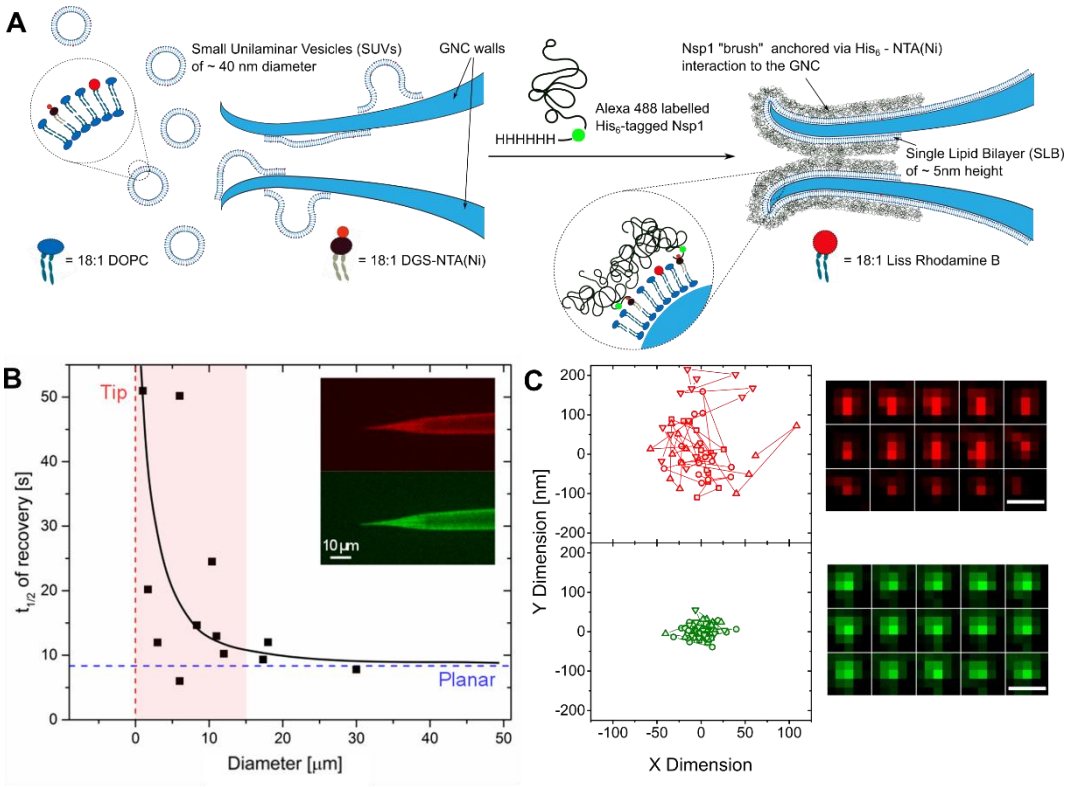

Figure 5.2: Functionalization of SLB coated GNCs with Nsp1FF12. **A**, Schematics of the SLB formation by spontaneous liposome spreading and subsequent Nsp1FF12 functionalization of GNCs with an hourglass tip shape (Schematics are not drawn to scale). **B**, FRAP experiments on functionalized GNCs confirm the fluid behavior of the SLB observed on planar glass surfaces. The half time of recovery seems to be dependent on the diameter of the examined region on GNC (black line is a guide to the eyes). The reason of this increase is not well understood, but might originate from the curvature itself or from the less accessible reservoir to replenish the fluorescent species. **C**, Single-molecule tracking of Rh PE (red) and DGS – Nsp1FF12 (green) supports the notion of brush-like behavior gained by FRAP experiments in Chapter 2.

In the end, lipid bilayer coated, hourglass shaped GNCs with an inner remaining channel of ~50 nm were employed to investigate the interaction of immobilized Nsp1FF12 with Kapβ1. Strikingly, two different pathways emerge from the analysis of the spatial density distribution (Figure 5.3). About 10 % of the Kapβ1 gather at the very center of the GNC and the remaining ~90 % are localized 24 ± 3 nm away from the axis. Compared to the center peak of the bimodal distribution of Rh PE (see Figure 5.1B), Kapβ1 is narrowly distributed around the central axis. This is an indication that a small fraction of Kapβ1 lives in a confined lumen restricted by a saturated Nsp1FF12 layer. However, the major fraction of Kapβ1 seems to be embedded in the FG rich Nsp1FF12 layer. Their location is in agreement with the reported distribution of Kapβ1 within the central channel of native NPCs (23 ± 1 nm)[11].

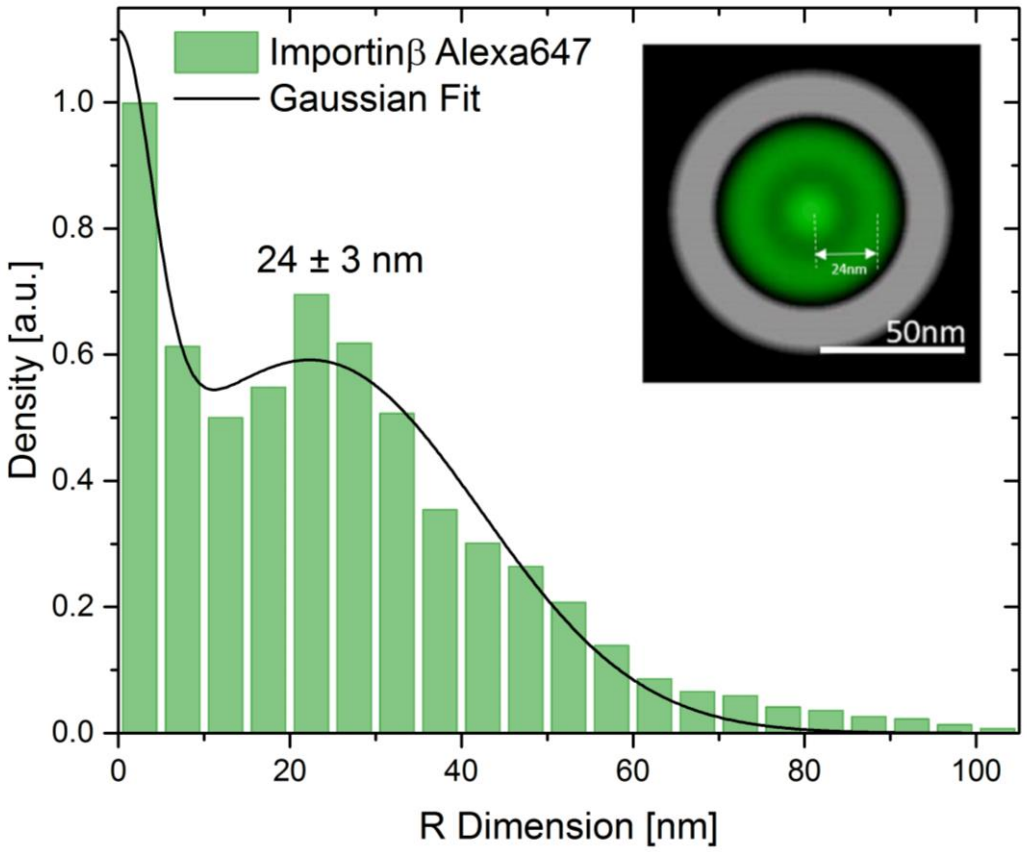

Figure 5.3: Kapβ1 interacting with Nsp1FF12 anchored to the inner GNC wall. Based on Gaussian fitting the spatial density distribution, ~90% of Kapβ1 molecules are found to be located at ~24 ± 3 nm. The rest likely stays at the very central lumen restricted by the surrounding saturated Nsp1FF12 layer. Inset: Cross-section view of the spatial density distribution (green cloud) of Kapβ1 locations along the central axis constrained by the GNC wall (grey).

Future experiments to address and characterize the spatio-temporal pathways of NTRs within artificial NPCs may also include lifetime-corrected FCS experiments. Parking of the GNC tip in a confocal volume may enable a statistical separation of three-dimensional (within the GNC lumen) and two-dimensional (along the functionalize GNC wall) diffusion. Possibly, a lifetime FRET assay would allow for the investigation of the exchange between layer bound NTRs and free NTRs in the lumen at the single-molecule level. A fluorescence-independent, label-free source of information of the collective conformational state of Nup layers as response to NTRs within the GNC may also be their electrophysiological noise characteristics. However, artificial NPCs based on GNCs open the way to investigate the interplay between various NTRs and various Nups in a well-defined environment, regardless of the employed techniques. This may reveal intrinsic differences between both Nups and NTRs that can determine the selectivity barrier.

5.3 References

1. Schleicher, K. D. *et al.* Selective transport control on molecular velcro made from intrinsically disordered proteins. *Nat. Nanotechnol.* **9,** 525–530 (2014).

2. Zweifel, L. P., Shorubalko, I. & Lim, R. Y. H. Helium Scanning Transmission Ion Microscopy and Electrical Characterization of Glass Nanocapillaries with Reproducible Tip Geometries. *ACS Nano* **10,** 1918–1925 (2016).

3. Eisele, N. B., Frey, S., Piehler, J., Görlich, D. & Richter, R. P. Ultrathin nucleoporin phenylalanine–glycine repeat films and their interaction with nuclear transport receptors. *EMBO Rep.* **11,** 366–372 (2010).

4. Eisele, N. B., Labokha, A. a., Frey, S., Görlich, D. & Richter, R. P. Cohesiveness tunes assembly and morphology of FG nucleoporin domain meshworks - Implications for nuclear pore permeability. *Biophys. J.* **105,** 1860–1870 (2013).

5. Hernández-Ainsa, S. *et al.* Lipid-coated nanocapillaries for DNA sensing. *Analyst* **138,** 104–106 (2013).

6. Sakiyama, Y., Mazur, A., Kapinos, L. E. & Lim, R. Y. H. Spatiotemporal dynamics of the nuclear pore complex transport barrier resolved by high-speed atomic force microscopy. *Nat. Nanotechnol.* **11,** 719–723 (2016).

7. Paradise, A., Levin, M. K., Korza, G. & Carson, J. H. Significant Proportions of Nuclear Transport Proteins with Reduced Intracellular Mobilities Resolved by Fluorescence Correlation Spectroscopy. *J. Mol. Biol.* **365,** 50–65 (2007).

8. Kapinos, L. E., Schoch, R. L., Wagner, R. S., Schleicher, K. D. & Lim, R. Y. H. Karyopherin-centric control of nuclear pores based on molecular occupancy and kinetic analysis of multivalent binding with FG nucleoporins. *Biophys. J.* **106,** 1751–1762 (2014).

9. Valle Aramburu, I. *et al.* Plasticity of Nucleoporin Nuclear Transport Receptor Interactions - Molecular Description of a Highly Dynamic, Ultrafast Interaction Mechanism. *Biophys. J.* **110,** 734–745 (2016).

10. Raveh, B. *et al.* Slide-and-exchange mechanism for rapid and selective transport through the nuclear pore complex. *Proc. Natl. Acad. Sci. U. S. A.* **113,** 2489-2497 (2016).

11. Ma, J. & Yang, W. Three-dimensional distribution of transient interactions in the nuclear pore complex obtained from single-molecule snapshots. *Proc. Natl. Acad. Sci. U. S. A.* **107,** 7305–7310 (2010).

12. Yang, W. & Musser, S. M. Nuclear import time and transport effi ciency depend on importin beta concentration. *J. Cell Biol* **174,** 951–961 (2006).

13. Ribbeck, K. & Gorlich, D. Kinetic analysis of translocation through nuclear pore complexes. *EMBO J.* **20,** 1320–1330 (2001).

14. Steinbock, L. J., Steinbock, J. F. & Radenovic, a. Controllable shrinking and shaping of glass nanocapillaries under electron irradiation. *Nano Lett.* **13,** 1717–1723 (2013).

Appendix

Appendix

Appendix Chapter 2

Modified Free Area Model for Obstructed Lipid Diffusion

Free area models for lipid diffusion in two-dimensions are based on the free-volume theory for diffusion in liquids[1,2]. The diffusion coefficient is defined as the integral over the distribution of free area

$$D = \int_{a^*}^{\infty} D(a)p(a)\,da$$

In a first approximation $D(a)$ is thought to be a constant diffusion within the free area. $p(a)$ is the probability of finding a free area of size a which is only useful for diffusion, above a critical value a^* equal to the closed packed disc area of a lipid given by

$$p(a) \sim e^{(-\frac{\vartheta a^*}{a_f})}$$

where ϑ is a correction factor for overlapping free areas and a_f is the mean free area per lipid determined by the total area a_t minus a^*. In a second approximation[3] D is also dependent on an activation energy to enter an adjacent void leading to

$$D = D_0\, e^{-(\frac{\vartheta a^*}{a_f} + \frac{E_a}{kT})}$$

Introducing obstacles leads to scattering of lipids and consequently to a reduction of their diffusivity. A modified free area model captures this effect. In addition to the repulsion of a hard sphere, this model also includes a possible soft-core repulsion due to partial ordering of lipids in the vicinity of an obstacle, *i.e.* the formation of an annulus of ordered lipids around the obstacle with coherence length ξ.

A numerical solution is given by Almeida *et al.* (1992)[4], which relates the relative (or normalized) diffusion D^*_{tracer}, with the area fraction of the obstacle c, the radius of the obstacles R and the coherence length

$$D^*_{tracer}(c) = 1 + ac + bc^2$$

where

$$a = -1.208 - 24.3\, e^{\left(\frac{-1.763R}{\xi}\right)} - 2.408\, e^{\left(\frac{-0.3138R}{\xi}\right)}$$

and

$$b = 185e^{\left(\frac{-2.587R}{\xi}\right)}$$

whereas no physical significance is attached to the numerical parameters *a* and *b*. If $R/\xi < 1.17$ the curve reaches a minimum with no physical meaning before going through zero, simply indicating that the approximations of the model break down for $c > c_{min}$: $\partial D^*_{tracer}(c_{min}) / \partial c = 0$.

The Alexander – de Gennes brush model

The Flory theory (1953) leads to a universal power law dependence of the polymer size *R* on the number Kuhn monomers *N:*

$$R \sim N^{\nu}$$

where the exponent depends on the solvent ($\nu_{good} = 3/5$, $\nu_\theta = 1/2$ and $\nu_{poor} = 1/3$). Applying the scaling approach, each FG domain is considered to be constraint within a tube of diameter *g* formed by surrounding FG domain chains. The chain is thought to be made of correlation blobs containing *n* Kuhn monomers of length *b* (total number of Kuhn monomers of the entire FG domain chain is *N*). The *n* segments within a blob are assumed to behave like random coils and therefore

$$g = bn^{\nu}$$

The total thickness of a grafted FG domain with *N* Kuhn monomers is hence

$$h = \frac{Ng}{n} = N\frac{b^{\nu^{-1}}}{g^{(\nu^{-1})-1}}$$

Under the assumption that a constant number of monomers distributes uniformly within the FG layer the volume fraction writes

$$\varphi = \frac{N\sigma}{hV_0}$$

where σ is the grafting density ($\sigma = g^{-2}$) and V_0 is the volume of a monomer. Considering the expression for h:

$$\varphi = \frac{N\sigma}{hl^3} = \frac{Ng^{-2}}{hV_0} = \frac{g^{((\nu^{-1})-3)}}{V_0 b^{\nu^{-1}}}$$

According to Vovk *et al.*[5], the height of FG Nup domain brushes follow all a power law dependence for any given interaction parameter χ (see main text):

$$h \sim g^{-p}$$

Applied to FG domain brushes grafted to an Au surface[6–8], they find that $p \in [0.9, 2]$ and all $\chi \in [-2.5,-0.8]$. The entire relation p - χ for a the cohesion strength from 0 to -2.5 is shown in the figure below.

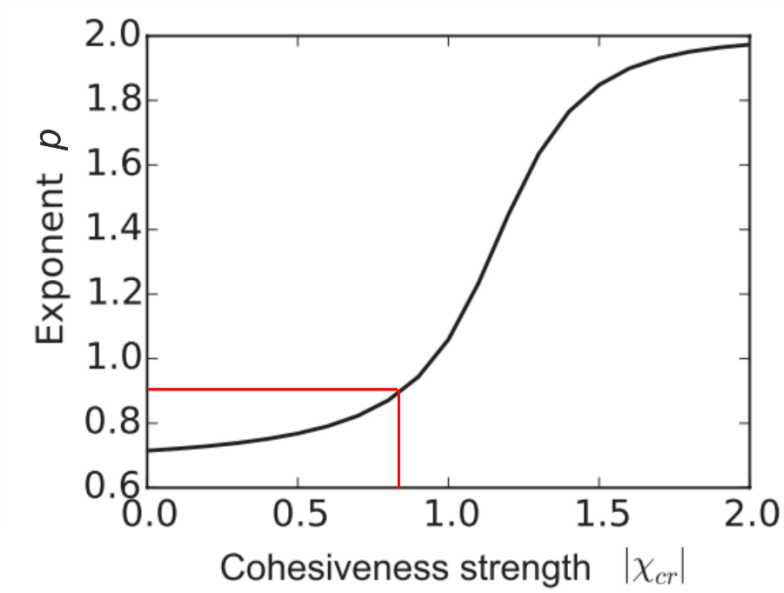

The exponent p increases from 2/3 to 2 as the absolute value of the cohesion strength χ increases from 0 to -2.5. The red lines indicate the lower boundaries for FG Nup brushes grafted to gold. Figure adapted from Vovk *et al.*[5]

The boundary value χ = -0.8 corresponds to an exponent p = 0.9 and a Flory parameter $\nu \approx 0.525$ and the boundary value χ = -2.5 to p = 2 and ν = 0.333. Note: For the lower case, ν = 0.333 is the Flory solution for a poor solvent, where all brushes collapse and the FG Nup layer behaves effectively like a material of constant density.

Matlab Code to Reduce Overweighting of the Slow Phase

ROI1 is the bleached area, ROI2 is the surrounding area including ROI2 and ROI3 is the background intensity.

```
handles.leg = 'Data';
   handles.resleg = '';
   R1=handles.ROI1-handles.ROI3;
   R1pre=mean(R1(1:handles.prebleach,:));
   R2=handles.ROI2-handles.ROI3;
   R2pre=mean(R2(1:handles.prebleach,:));
   n11=R1./R2;
   n12=R2pre./R1pre;
   k=size(handles.ROI1,2);
   for i=1:k
      g(:,i)=n11(:,i)*n12(i);
   end
   g1=g(handles.prebleach+1,:);
   for j=1:k
      n1(:,j)=(g(:,j) - g1(j))./(1-g1(j));
   end

%Average normalized curves
   n2=n1;
   handles.norm1=n1;
   handles.norm1(handles.prebleach+1:handles.prebleach,:)=[];
   handles.t1=handles.t;
   handles.t1(handles.prebleach+1:handles.prebleach,:)=[];
   handles.mn=mean(handles.norm1,2);
   handles.stdev=std(handles.norm1,0,2);

   handles.norm2=n2;
   handles.norm2(1:handles.prebleach,:)=[];
   handles.t2=handles.t(:,1);
   handles.t2(1:handles.prebleach)=[];
   handles.t2=handles.t2-handles.t2(1);
   handles.mn2=mean(handles.norm2,2);

%Fit asymptotes to average curve
   x=handles.t2;
   p = polyfit(x(1:10),handles.mn2(1:10),1);
   pfit= (p(1))*(x-handles.t(handles.prebleach+1,1))+p(2);

   x=handles.t1;
   p2 = polyfit(x(end-30:end,1),handles.mn2(end-30:end),1);
   pfit2= p2(1)*(x)+p2(2);

   handles.fit1=pfit;
   handles.fit2=pfit2;
```

```
%approximate cross over value
fun=@(x)abs(((p(1)/2)*(x-handles.t(handles.prebleach+1,1))+p(2))-(p2(1)*x+p2(2)));
options = optimset('Display','final','Maxiter',10000,'maxfuneval',50000);
x_min = fminsearch(fun,5,options);
dist=abs(handles.t1(:,1)-x_min);
%index of closest value
[c, idx] = min(dist)
%closest value
closest = handles.t1(idx,1)

%number of data points in fast regime
num_df=idx-handles.prebleach;
%number of data points in slow regime
num_ds=size(handles.t1(:,1),1)-idx;

ratio=num_ds/num_df;

%equalize the number of data points depending of the ratio (threshold set to 2) of points
%before and after the asymptotic cross over. To do so, points in the
%slow regime (after the cross over point) are averaged accordingly

ds_single_new_conc=[];

if ratio > 2

s=round(ratio);
t_ds=handles.t1(idx:end,1);
ds=handles.mn(idx:end);
ds_single=handles.norm1(idx:end,:)
ds_err=handles.stdev(idx:end);
rest=mod(num_ds,s);
ds_new=[];
ds_single_new=[];
ds_err_new=[];
t_ds_new=[];
m=((num_ds-rest)/s);

if mod(s,2) == 0

    for n=0:s:(num_ds-s-rest)
    ds_new=[ds_new mean(ds(n+1:n+s))];
    ds_err_new=[ds_err_new mean(ds_err(n+1:n+s))];
    t_ds_new=[t_ds_new mean(t_ds(n+1:n+s))];
    ds_single_new=[ds_single_new; mean(ds_single(n+1:n+s,:))];

    end
    ds_single_new=[handles.norm1(1:idx,:); ds_single_new; handles.norm1(end-rest:end,:)];
    ds_new=[(handles.mn(1:idx))' ds_new (handles.mn(end-rest:end))'];
    ds_err_new=[(handles.stdev(1:idx))' ds_err_new (handles.stdev(end-rest:end))'];
    t_ds_new=[(handles.t1(1:idx,1))' t_ds_new (handles.t1(end-rest:end,1))'];
```

```
  else

     for n=0:s:(num_ds-s-rest)
     ds_new=[ds_new mean(ds(n+1:n+s))];
     ds_err_new=[ds_err_new mean(ds_err(n+1:n+s))];
     t_ds_new=[t_ds_new t_ds(n+round(s/2)-1)];
     ds_single_new=[ds_single_new; mean(ds_single(n+1:n+s,:))];


     end
     ds_single_new=[handles.norm1(1:idx,:); ds_single_new; handles.norm1(end-rest:end,:)];
     ds_new=[(handles.mn(1:idx))' ds_new (handles.mn(end-rest:end))'];
     ds_err_new=[(handles.stdev(1:idx))' ds_err_new (handles.stdev(end-rest:end))'];
     t_ds_new=[(handles.t1(1:idx,1))' t_ds_new (handles.t1(end-rest:end,1))'];

  end

  handles.singlemanip=ds_single_new;
  handles.tmanip=t_ds_new';
  handles.datamanip=ds_new';
  handles.dataerror=ds_err_new';

else
handles.singlemanip=handles.norm2;
handles.tmanip=handles.t2;
handles.datamanip=handles.mn2;
handles.dataerror=handles.stdev;

end

   else
   return
end
```

Details of the Used FG Nup Constructs

Nsp1FF12

MCCWHHHHHHSSGLVPRGSGMKETAAAKFERQHMDSPDLGTGSENLYFQGAMAKPAL
SFGTATSDNKTTNTTPSFSFGAKSDENKAGATSKPAFSFGAKPEEKKDDNSSKPAFSFGAKS
NEDKQDGTAKPAFSFGAKPAEKNNNETSKPAFSFGAKSDEKKDGDASKPAFSFGAKPDEN
KASATSKPAFSFGAKPEEKKDDNSSKPAFSFGAKSNEDKQDGTAKPAFSFGAKPAEKNNNE
TSKPAFSFGAKSDEKKDGDASKPAFSFGAKSDEKKDSDSSKPA

Nsp1SS12

MCCWHHHHHHSSGLVPRGSGMKETAAAKSERQHMDSPDLGTGSENLYSQGAMAKPAL
SSGTATSDNKTTNTTPSSSSGAKSDENKAGATSKPASSSGAKPEEKKDDNSSKPASSSGAKS
NEDKQDGTAKPASSSGAKPAEKNNNETSKPASSSGAKSDEKKDGDASKPASSSGAKPDEN
KASATSKPASSSGAKPEEKKDDNSSKPASSSGAKSNEDKQDGTAKPASSSGAKPAEKNNNE
TSKPASSSGAKSDEKKDGDASKPASSSGAKSDEKKDSDSSKPA

Nup153 after His Tag cleavage

GSRGCCCESAKPGTKSGFKGFDTSSSSSNSAASSSFKFGVSSSSSGPSQTLTSTGNFKFGDQ
GFKIGVSSDSGSINPSEGFKFSKPIGDFKFGVSSESKPEEVKKDSKNDNFKFGLSSGLSNPVSL
TPFQFGVSNLGQEEKKEELPKSSSAGFSFGTGVINSTPAPANTIVTSENKSSFNLGTIETKSAS
VAPFTCKTSEAKKEEPATKGGFSFGNVEPASLPSASVFVLGRTEEKQQEPVTSTSLVFGKKAD
NEEPKCQPVFSFGNSEQTKDENSSKSTFSFSTKPSEKESEQPAKATFAFGAQTSTTADQGAA
KPVFSFLNNSSSSSSTPATSAGGGIFGSSTSSSNPPVATFVFGQSSNPVSSSAFGNTAESSTSS
LLFSQDSKLATTSSTGTAVTPFVFGPGASSNNTTTSGFGFGATTTSSSAGSSFVFGTGPSAPS
ASPAFGANQTPTFGQSQGASQPNPPGFGSISSSTALFPTGSQPAPPTFGTVSSSSQPPVFQ
PSQSAFGSGTTPNSSSAFQFGSSTTNFNFTNNSPSGVFTFGANSSTPAASAQPSGSGGFPQ
SPAAFTVGSNGKNVFSSSGTSFSGRKIKTAVRRRK

Nup98 after His Tag cleavage

GGSCCCFNKSFGTPFGGGTGGFGTTSTFGQNTGFGTTSGGAFGTSAFGSSNNTGGLFGNS
QTKPGGLFGTSSFSQPATSTSTGFGFGTSTGTANTLFGTASTGTSLFSSQNNAFAQNKPTGF
GNFGTSTSSGGLFGTTNTTSNPFGSTSGSLFGPSSFTAAPTGTTIKFNPPTGTDTMVKAGVS
TNISTKHQCITAMKEYESKSLEELRLEDYQANRKGPQNQVGAGTTTGLFGSSPATSSATGLF
SSXTTNSGFAYGQNKTAFGTSTTGFGTNPGGLFGQQNQQTTSLFSKPFGQATTTQNTGFS
FGNTSTIGQPSTNTMGLFGVTQASQPGGLFGTATNTSTGTAFGTGTGLFGQTNTGFGAVG
STLFGNNKLTTFGSSTTSAPSFGTTSGGLFGFGTNTSGNSIFGSKPAPGTLGTGLGAGFGTAL
GAGQASLFGNNQPKIGGPLGTGAFGAPGFNTTTATLGFGAPQAPVALTDPNASAAQQAV
LQQHINSLTYSPFGDS

SPR measurement procedure and analysis of the binding kinetics

Human Nup98 or Nup153 and yeast Nsp1FF12 or Nsp1SS12 FG domains (with cysteine at their N-terminus) were anchored to the Au surface *via* covalent sulfide bonds. To form comparable FG domain brushes on the supported lipid layer, HPA sensor chips were washed 5-min with 40 mM octyl-glucoside(n-octylβ-D glucopyranoside) (OG) in water to condition the surface and subsequently liposomes (30 nm) containing 20% NTA(Ni) modified DGS lipids were injected. Consequently, a single lipid monolayer was formed on the hydrophobic surface of the HPA chip exposing Ni^{2+}-NTA for His_6-Nup98, His_6-Nup153, His_6-Nsp1FF12 and His_6-Nsp1SS12 capture. The lipid layers are reusable after releasing the FG Domains by imidazol and stripping of Ni^{2+} with EDTA. The mean grafting distance was determined in both cases form the Nups binding response as it was shown previously[6,7]. The mean height of the layer was measured by using innate BSA molecules after layer formation[9]. Equilibrium binding constants were obtained by plotting the SPR response (R_{eq}) at steady state equilibrium as a function of Kapβ1 concentration and a Langmuir absorption isotherm fit of 2 components (see Figure 2.6).

The multivalent binding kinetic analysis was done using numerical fit to the sensograms. The basic idea of surface heterogeneity is applied to facilitate the interpretation of multivalent binding kinetics of Kapβ1 interacting with FG domains as explained in detail by Kapinos *et al*. (2014)[6].

Two-dimensional kinetic maps obtained after the numerical fit to the sensograms of Kapβ1 binding for Nsp1FF12, Nup98 and Nup153 layers immobilized on gold surfaces (blue) and on SLMs (brown) are shown in the following ((Figure below A, B and C, respectively). The fractional abundance of the kinetic states for FG domains grafted to Au or DGS NTA(Ni) containing lipid layers coincide remarkably. Three states dominate: At low Kapβ1 concentration, a fast k_{on} into the largely unsaturated FG domain brushes pairs with a slow k_{off} due to high binding avidity (★). At high (physiological) Kapβ1 concentration the layers are saturated and two states evolve. A fast k_{on} and k_{off} pair represents the limited multivalent interaction at the brush periphery (▲) and a slow k_{on} and k_{off} due to slow penetration and release from the occupied FG domain brush (○).

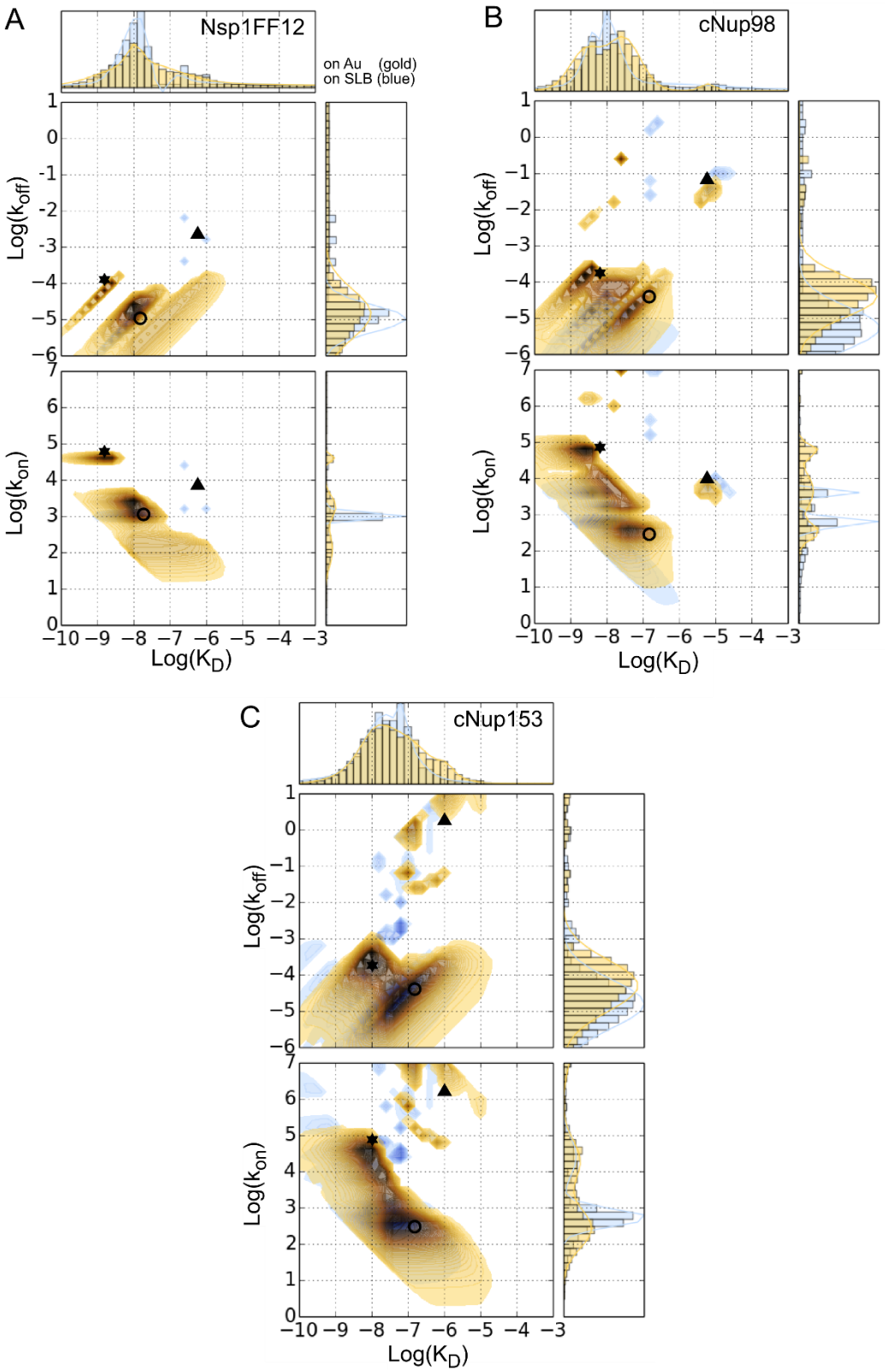
A
Nsp1FF12
on Au (gold)
on SLB (blue)
Log(k_off)
Log(k_on)
Log(K_D)
B
cNup98
Log(k_off)
Log(k_on)
Log(K_D)
C
cNup153
Log(k_off)
Log(k_on)
Log(K_D)

Appendix Chapter 4

Fabrication parameters

Heat and velocity values with related heat on times and shapes (filament 0, pull 255, delay 170). Heat on mean and standard deviation values have been obtained from $N_1 = 8$, $N_2 = 13$, $N_3 = 20$, $N_4 = 11$, $N_5 = 30$, $N_6 = 21$ and $N_7 = 14$ pulls.

Program	Heat	Velocity	Heat on [s]	Shape
1	460	25	0.92 ± 0.03	Bullet
2	460	18	0.94 ± 0.03	Bullet
3	600	15	0.59 ± 0.02	Blunt
4	400	30	1.32 ± 0.05	Blunt
5	400	25	1.30 ± 0.04	Hour-glass
6	400	20	1.27 ± 0.05	Hour-glass
7	300	40	4.31 ± 0.35	Hour-glass

On the HeSTIM resolution

All GNCs were imaged at a resolution of 0.95 nm^2 per pixel (FOV = 2 µm and 2048x2048 pixels). Representative GNCs for the three different types (bullet, blunt and hourglass) from programs (1, 3 and 5) leading to the smallest pore size are shown in the subsequent figures.

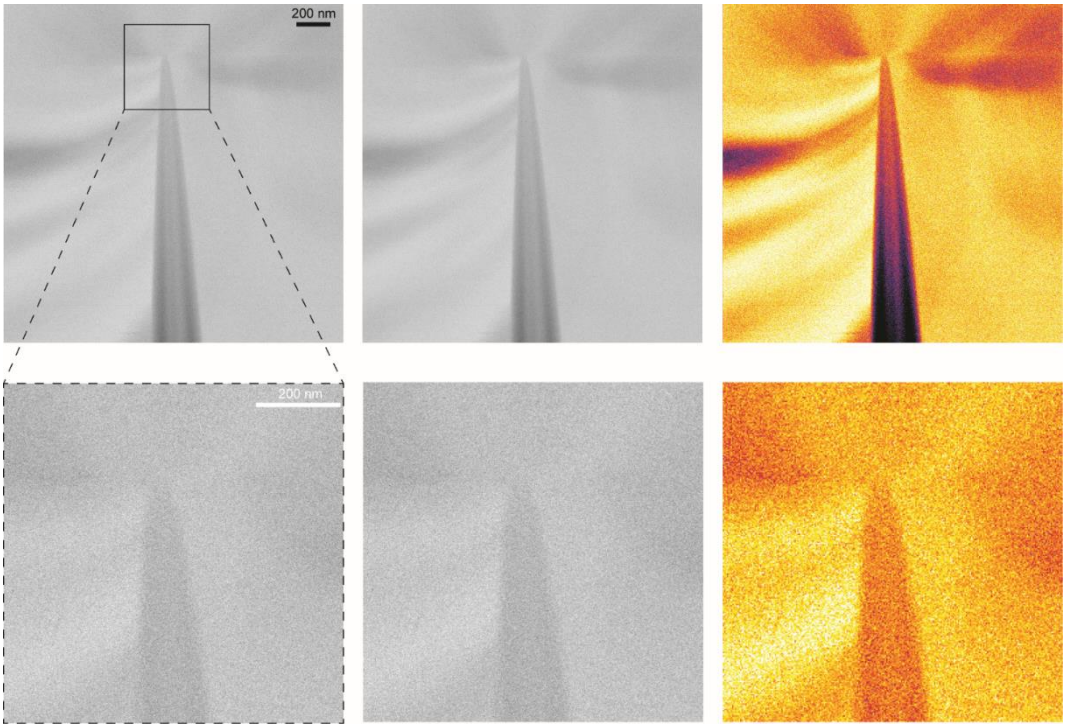

Representative bullet-like GNC from program 1**.** Images in the top row show a FOV = 2x2 µm resolved at 2048x2048 pixels. Top left is the unmodified original image. Top middle and right are contrast enhanced and 2x2 binned for a better visibility. The bottom row provides zoom ins of a FOV = 500x500 nm resolved at 512x512 pixels. Bottom middle and right are contrast enhanced and 2x2 binned for a better visibility.

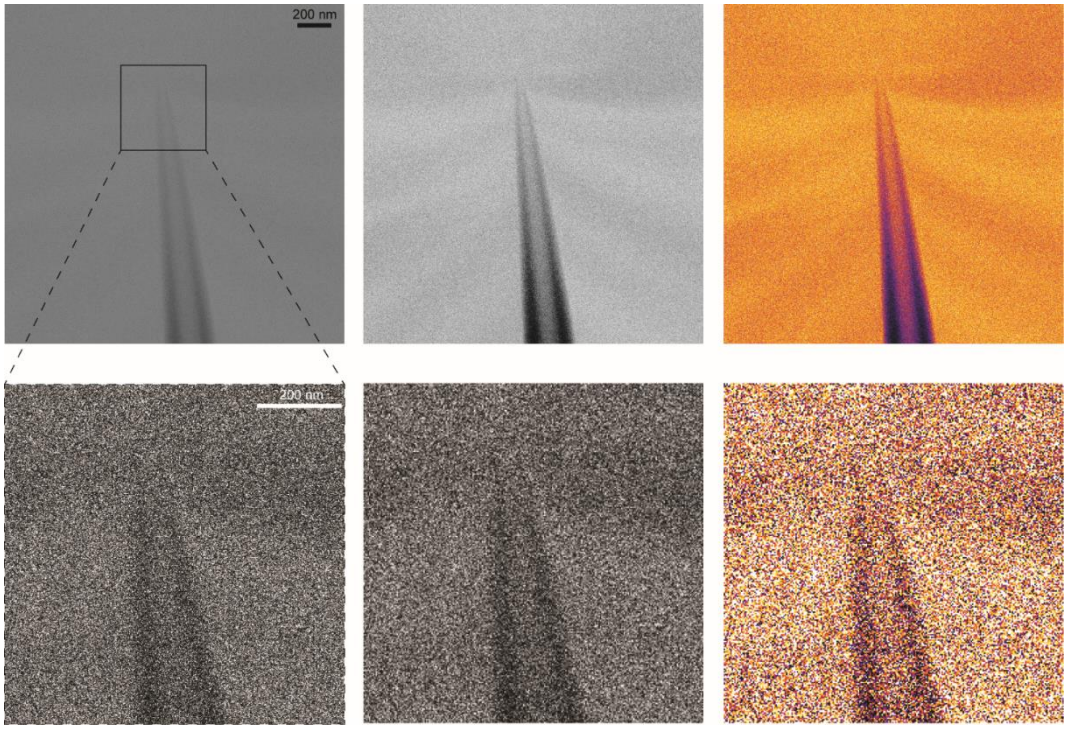

Representative blunt-ended GNC from program 3**.** Images in the top row show a FOV = 2x2 µm resolved at 2048x2048 pixels. Top left is the unmodified original image. Top middle and right are contrast enhanced and 2x2 binned for a better visibility. The bottom row provides zoom ins of a FOV = 500x500 nm resolved at 512x512 pixels. Bottom middle and right are contrast enhanced and 2x2 binned for a better visibility.

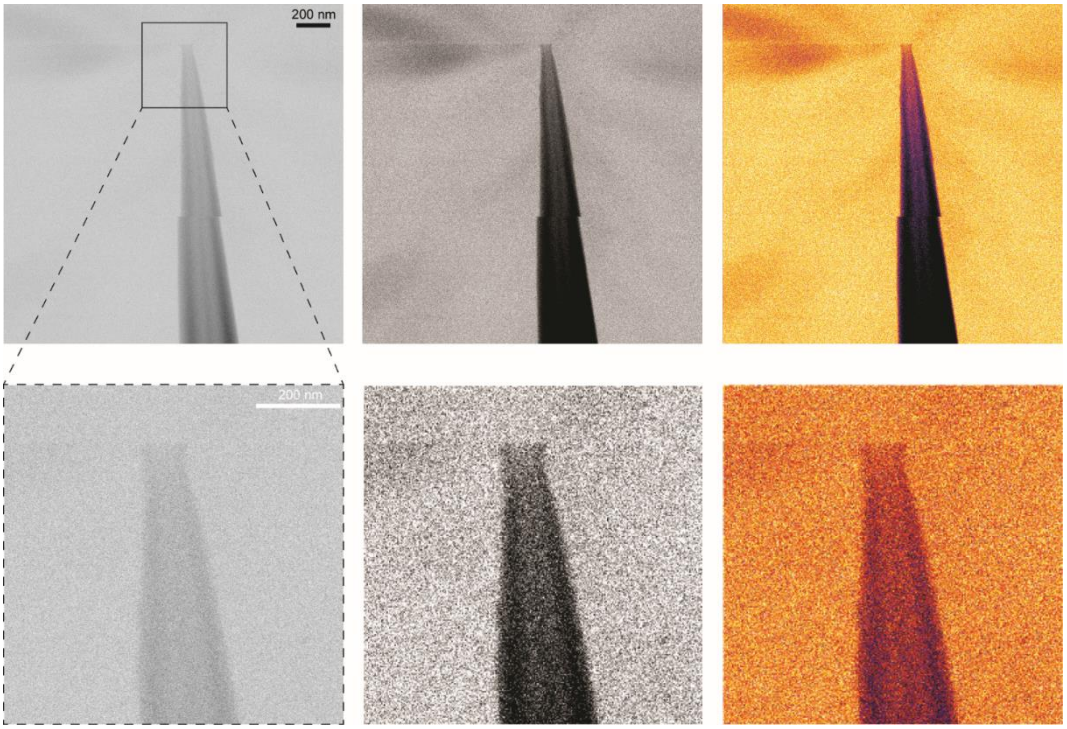

Representative hourglass-shaped GNC from program 5**.** Images in the top row show a FOV = 2x2 µm resolved at 2048x2048 pixels. Top left is the unmodified original image. Top middle and right are contrast enhanced and 2x2 binned for a better visibility. The bottom row provides zoom ins of a FOV = 500x500 nm resolved at 512x512 pixels. Bottom middle and right are contrast enhanced and 2x2 binned for a better visibility.

Altitude angle dependence of the longitudinal intensity profile

Images GNCs (FOV = 2x2 µm and 1024x1024 pixels, scale bar 200 nm) of the same GNC at different altitude angles (angle between the horizontal plane and the GNC axis) reveal the linear dependence of the intensity drop on the thickness of the material which He ions have to pass. Longitudinal profiles are plotted along the prolonged GNC axes indicted in the images. The linear parts of profiles correspond to the range between tip openings (depicted with a small perpendicular bar) to the bottom of the images. Most right image is an overview (FOV = 100x100 µm and 1024x1024 pixels of which an area of 206x911 pixels is shown, scale bar 10 µm).

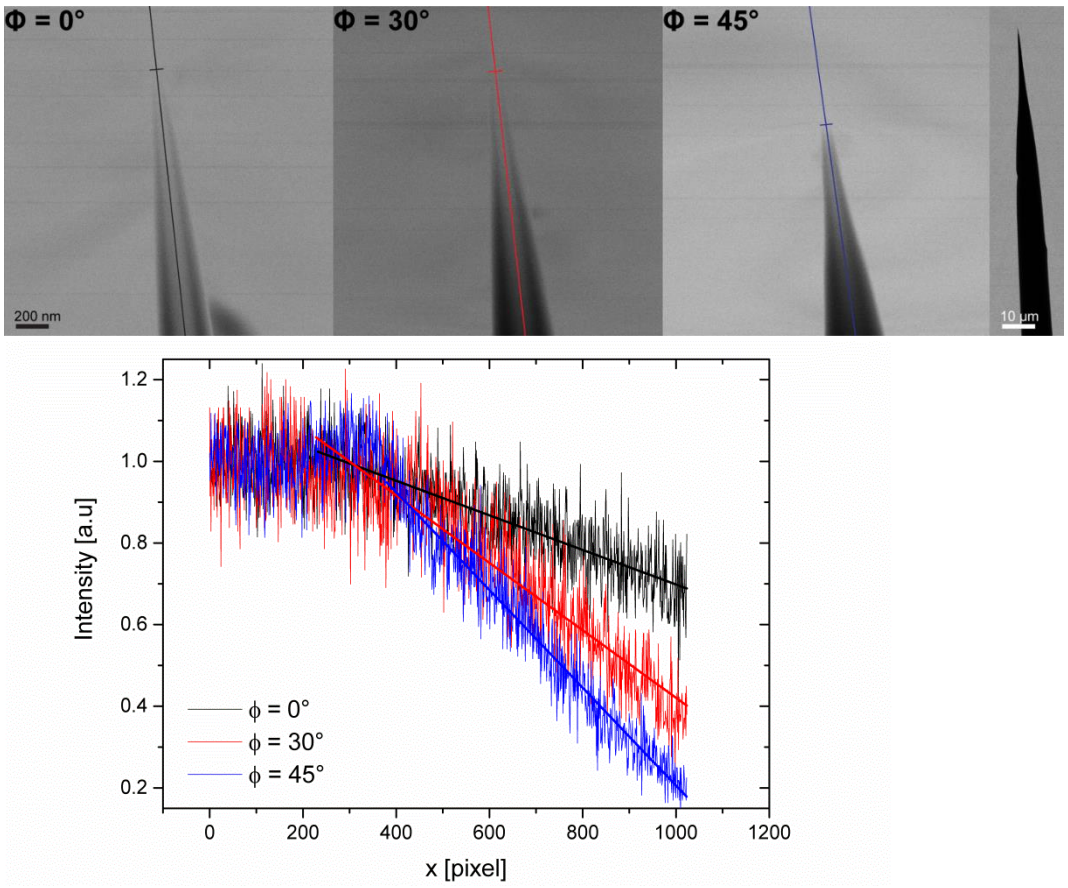

The same GNC imaged under different altitude angles and their corresponding longitudinal intensity profiles.

Images of GNCs

Images to support the reproducibility amongst GNCs from the same programs as stated in the main text. For each program 2x2 binned zoom ins of up to ten different GNCs (FOV = 2x2 µm and 1024x1024 pixels, scale bar 200 nm) and a representative overview (FOV = 100x100 µm and 1024x1024 pixels of which an area of 206x911 pixels is shown, scale bar 10 µm) are shown.

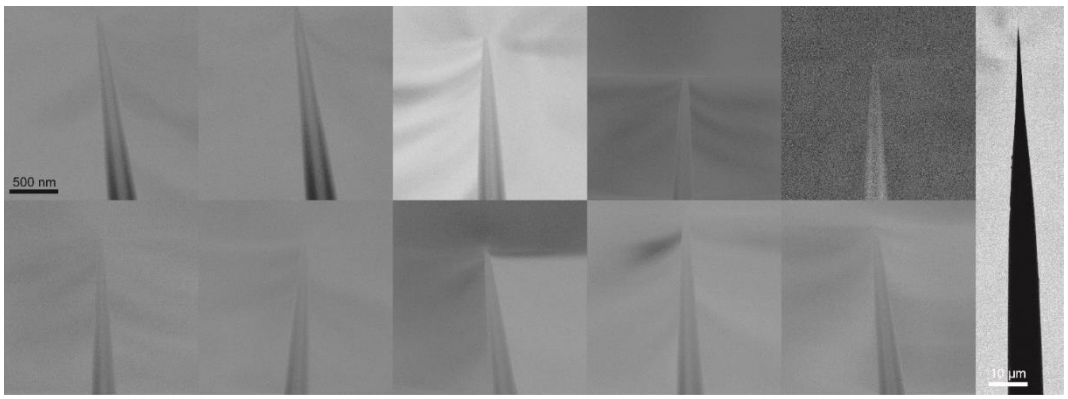

Bullet-like tips from program 1 in table 'fabrication parameters'

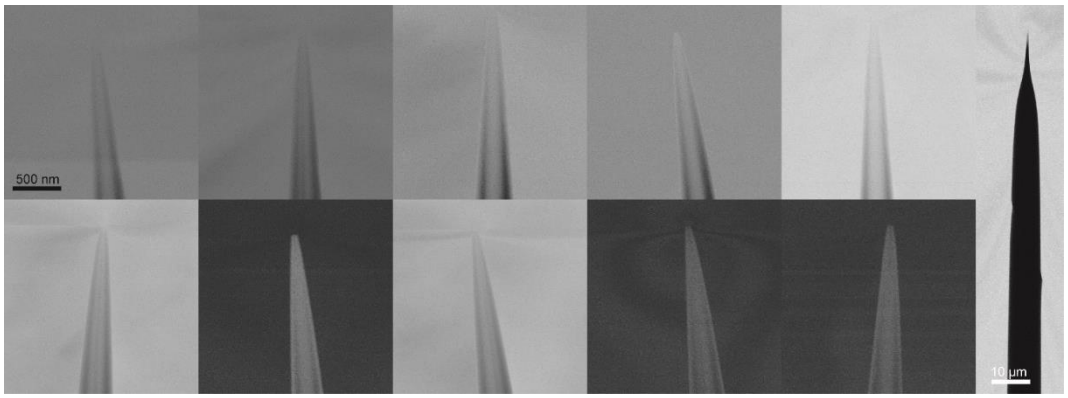

Bullet-like tips from program 2 in table 'fabrication parameters'

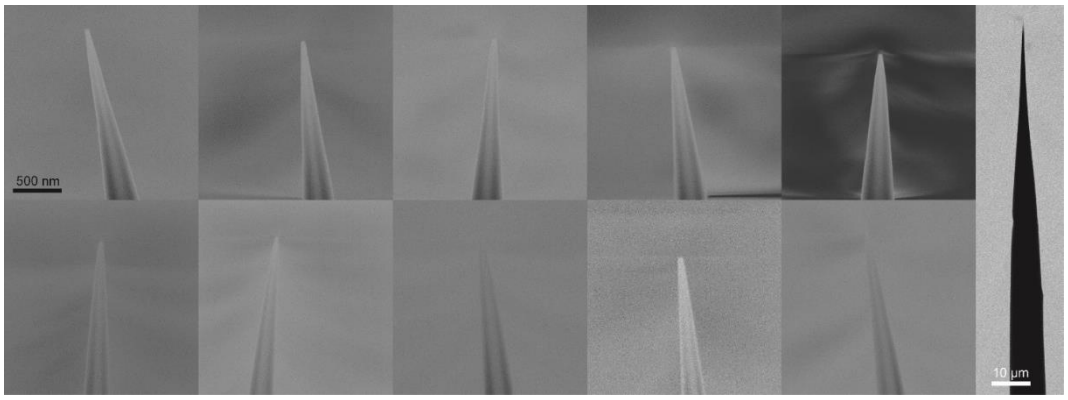

Blunt-ended tips from program 3 in table 'fabrication parameters'

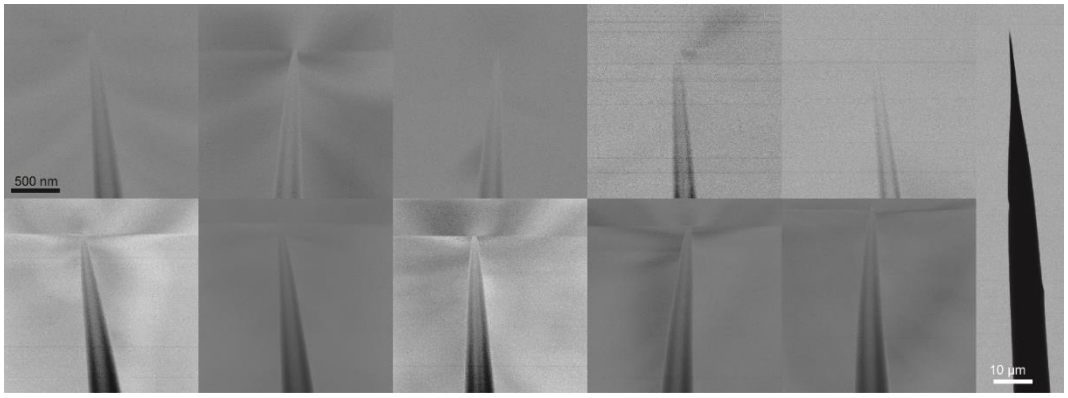

Blunt-ended tips from program 4 in ‘fabrication parameters’

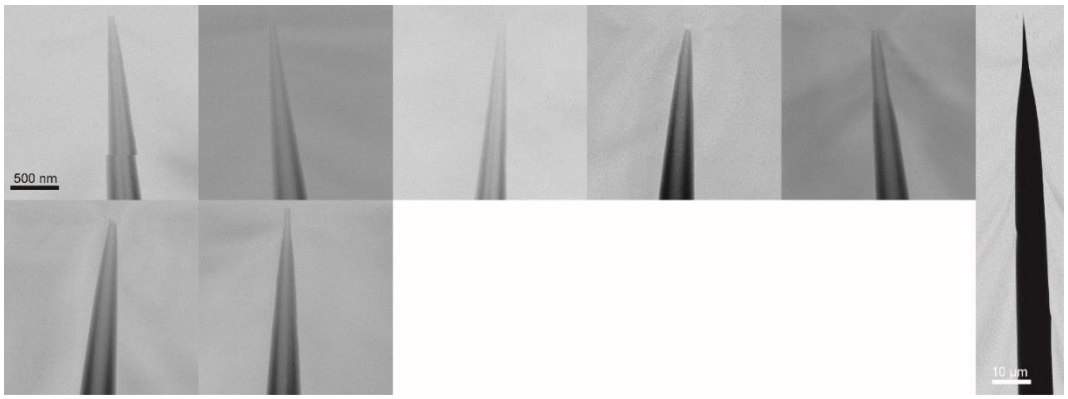

Hourglass shaped tips from program 5 in ‘fabrication parameters’

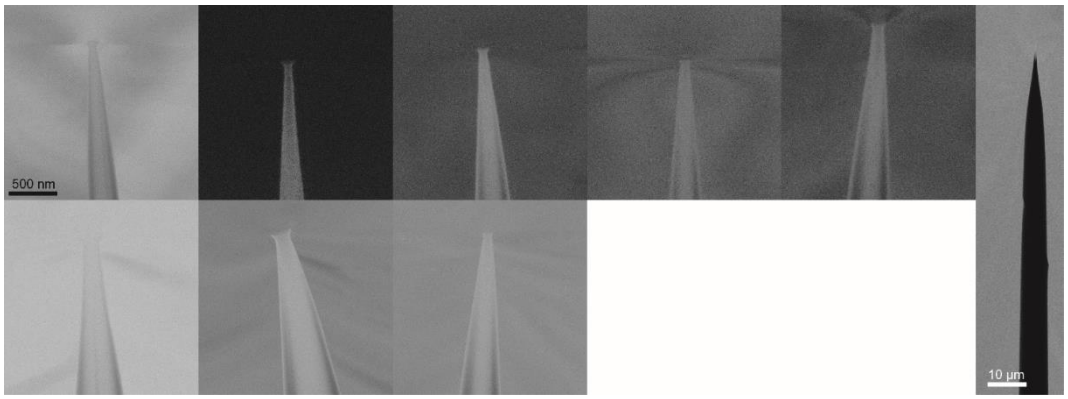

Hourglass tips from program 6 in table ‘fabrication parameters’

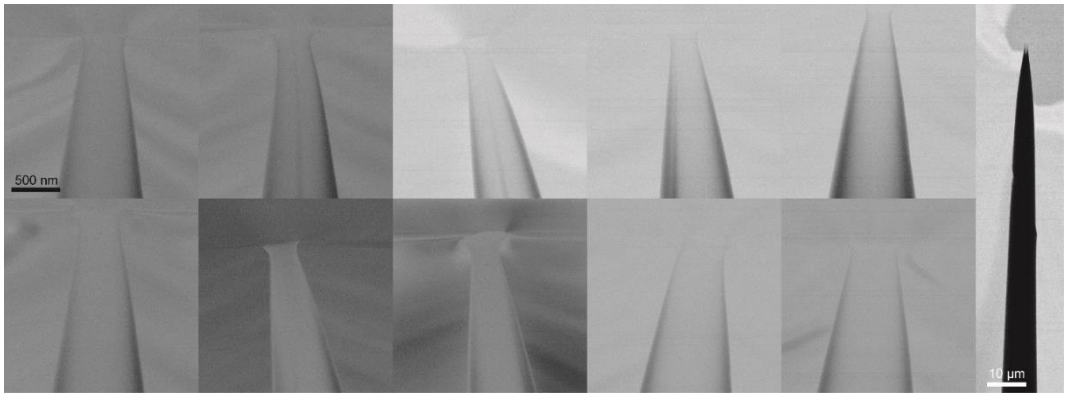

Bunt-ended tips from program 7 in table ‘fabrication parameters’

Influence of plasma cleaning

The insight that the O_2-plasma has an influence on the IV characteristics of GNCs triggered the attempts to produce GNCs reproducibly by laser assisted pulling. Finding a lower boundary where the influence of the plasma treatment is neglectable justifies not only hydrophilization before wetting, but also the moderate cleaning procedure (10W air plasma for 3 min at 0.8 mbar) prior to the imaging by He STIM.

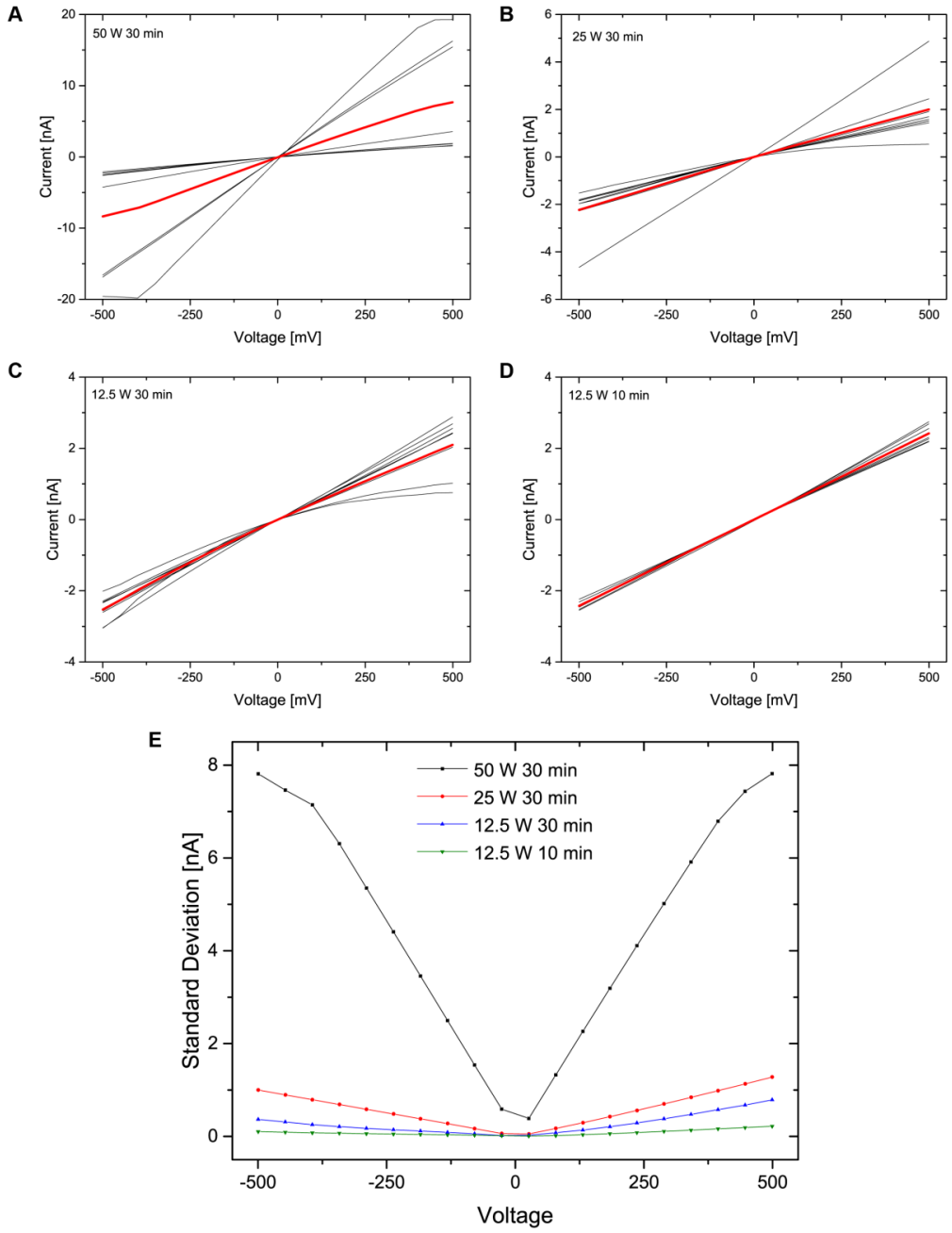

A-**D**, IV curves after treatment with different O_2 -plasma powers and exposure times (13.56 MHz, 5 sccm at

0.3 mbar). Each panel shows 8 GNCs pulled with the same program (black lines) and their average curve (red line). **E**, Standard deviation comparison from each average curve of panels **A**-**D** reveals a drastic influence of O_2 - plasma on the integrity of the GNCs in ion current measurements.

Single IV curves

Moderate plasma procedure (12.5 W for 10 min) for facilitated wetting has been applied to 10 GNCs of programs 1 to 7. Broken tips due to the handling during the wetting procedure (plasma, vakuum and reservoir transfer) and clear outliers are not considered. At least 50 % of the GNCs were successfully wetted and show reproducible IV response.

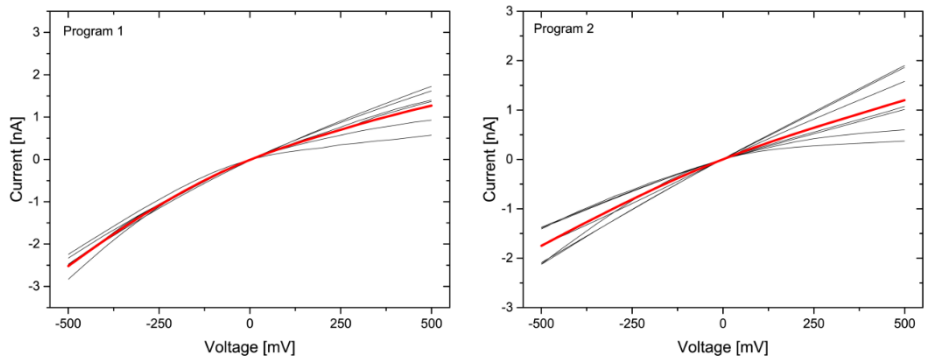

Single IV curves (black lines) and their average curve (red line) for bullet-like GNC tips from program 1 (N = 8) and program 2 (N = 7).

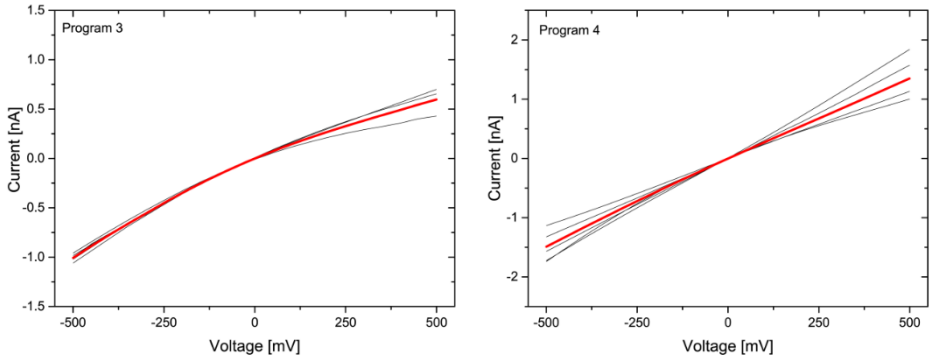

Single IV curves (black lines) and their average curve (red line) for blunt-ended GNC tips from program 3 (N = 6) and program 4 (N = 5).

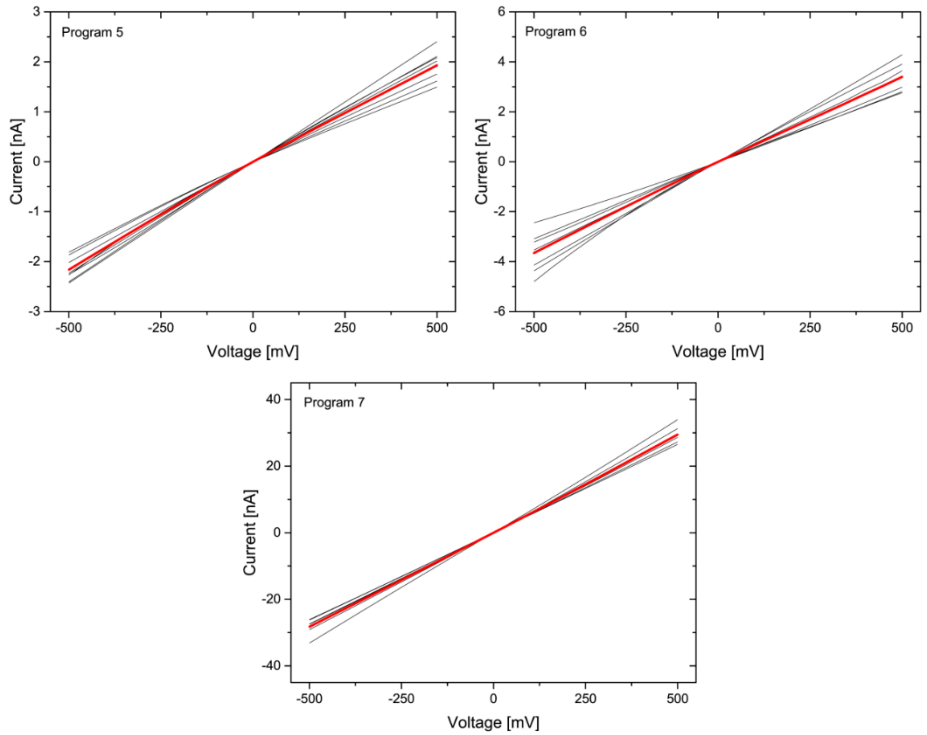

Single IV curves (black lines) and their average curve (red line) for hourglass shaped GNC tips from program 5 (N = 8), program 6 (N = 7) and program 7 (N = 8).

BSA adhesion effects on translocation signal

Proteins are known to adsorb on untreated glass surfaces. However, the effect of BSA adsorption on current recordings in single molecule translocation experiments through solid state nanopores is well understood[10], i.e. the nonspecific adsorption leads to long-lived current blockades as shown in the figure below. To avoid any influence from BSA adsorption we did not integrate current drops into our analysis, which emerged in regions of long-lived blockades.

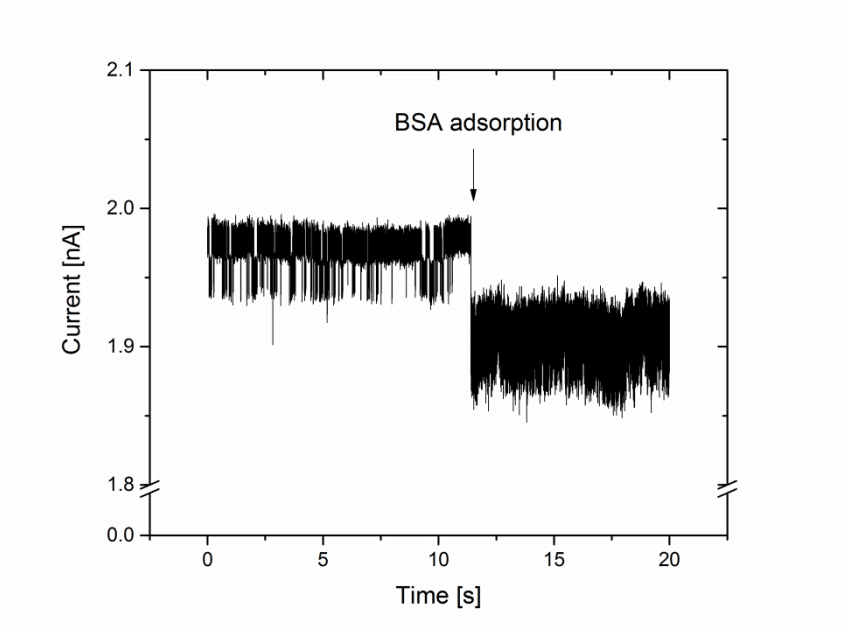

BSA adsorption on the GNC wall leads to a long-lived current blockage for a given voltage bias (500mV, hourglass GNC of type 5)

Normalized current drop and event duration distributions

Normalized current drop and event duration values in the main text are mean values over the entire distribution of events. To permit a comparison amongst reported values for similar experimental assays, i.e. BSA translocation through GNCs[11,12], log-normal fitting of the event duration distributions and normal fitting of the normalized current drop distributions has been performed.

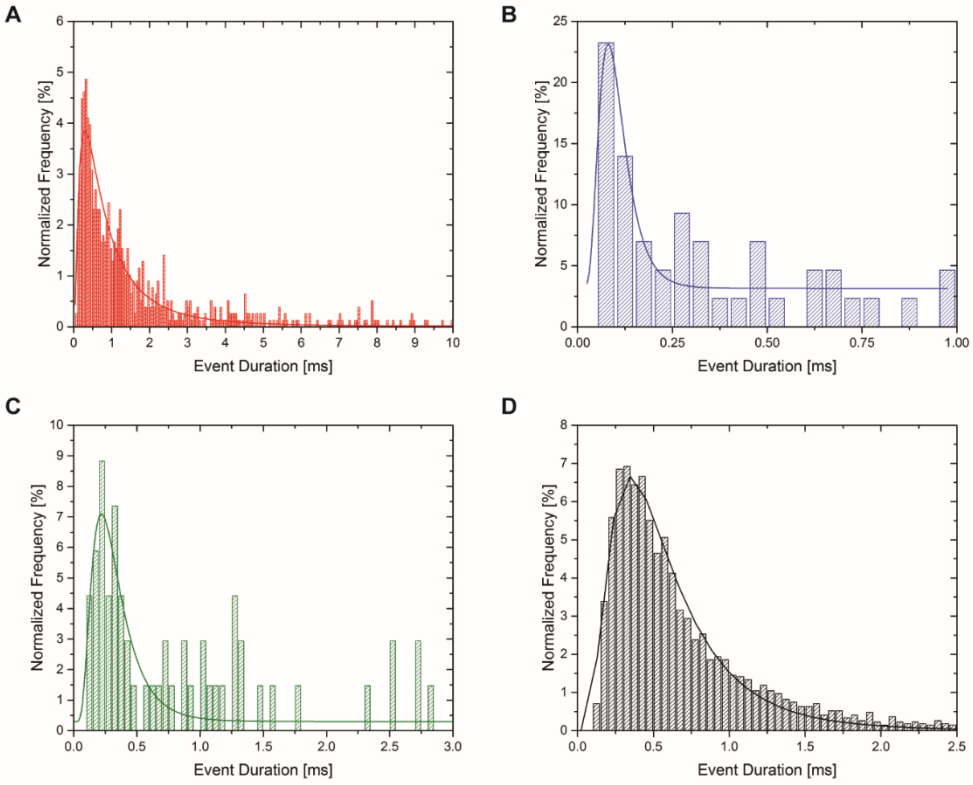

Event duration histograms (binning) and corresponding log-normal fits, with **A** blunt d_P = 25 nm and θ = 4° **B** bullet d_P = 39 nm and θ = 5.6° **C** blunt d_P = 30 nm and θ =5° and **D** hourglass d_P = 43 nm and θ = 4.4°. The obtained fit parameters are listed in the table below.

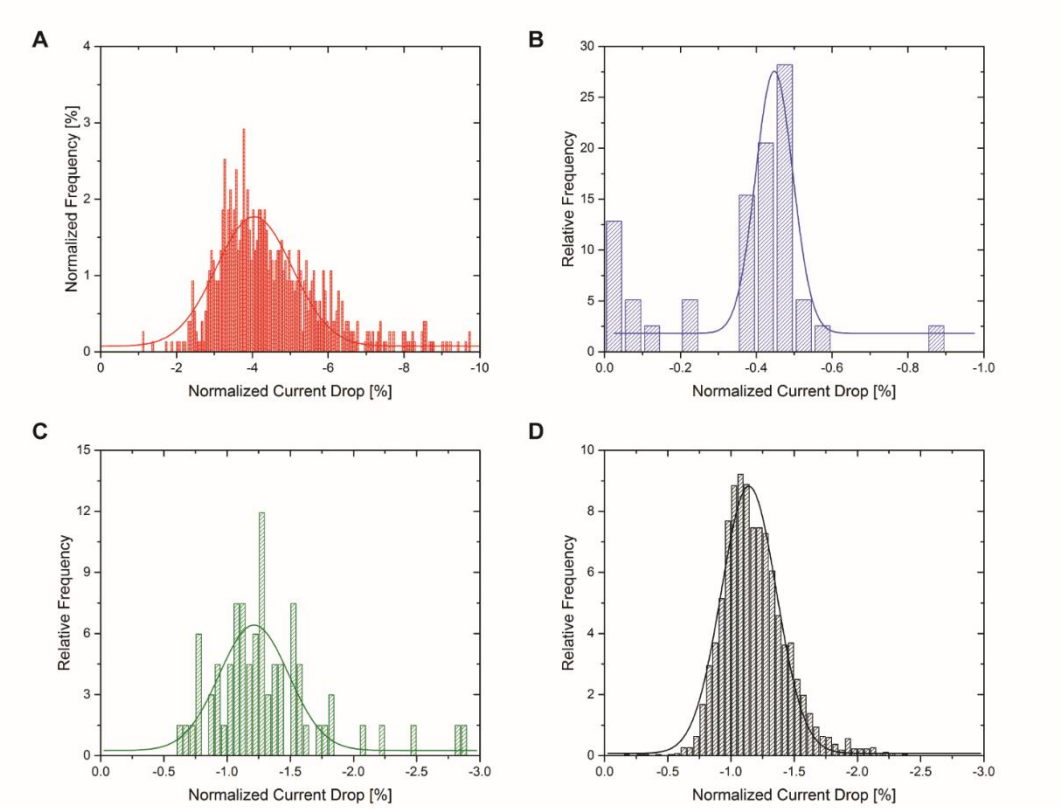

Normalized current drop histograms and corresponding normal fits of the scatter plots shown in the main text, with **A** blunt d_P = 25 nm and θ = 4° **B** bullet d_P = 39 nm and θ = 5.6° **C** blunt d_P = 30 nm and θ =5° and **D** hourglass d_P = 43 nm and θ = 4.4°. The obtained fit parameters are calculated back to mean current drops and listed in the table below.

Pulling parameter	Log-normal fit	Normal fit
f = 0, p = 255, d = 170, h= 600 v = 15 (Fig. S14A and S15A)	755 ± 12 µs	24.7 ± 4.7 pA
f = 0, p = 255, d = 170, h= 460 v = 18 (Fig. S14B and S15B)	96 ± 8 µs	10.2 ± 1.1 pA
f = 0, p = 255, d = 170, h= 400 v = 30 (Fig. S14C and S15C)	290 ± 14 µs	18.5 ± 9.3 pA
f = 0, p = 255, d = 170, h= 400 v = 25 (Fig. S14D and S15C)	506 ± 13 µs	23 ± 5.8 pA

Event duration and mean current drops from the histograms in the figures above obtained for BSA translocation in PBS 150 mM NaCl pH 7.2 (10kHz cut-off at 500mV)

Literature values for BSA translocation through GNCs. Ref. [2] refers to mean current drops and ref. [3] reports the mean of the blockage amplitude distribution. Both references used 1x TE, 1 M KCl pH 8 (10kHz cut-off at 500mV)

Pulling parameter	Event durations	Current drop
f = 0, p = 225, d = 170, h= 600 v = 25 [2]	~50 – ~200 µs	~10 – ~100 pA mean current drop
f = 0, p = 200, d = 140, h= 620 v = 30 [3]	~180 – ~600 µs	~215 pA mean peak to peak